Fall 2018

Damage detection using angular velocity

Samer Saadi Hussein Al Jailawi
University of Iowa

DAMAGE DETECTION USING ANGULAR VELOCITY

by

Samer Saadi Hussein Al Jailawi

A thesis submitted in partial fulfillment
of the requirements for the Doctor of Philosophy
degree in Civil and Environmental Engineering in the
Graduate College of
The University of Iowa

December 2018

Thesis Supervisor: Professor Salam Rahmatalla

ACKNOWLEDGMENTS

I would express my sincere gratitude to my advisor, Salam Rahmatalla, for providing me the opportunity to work with him, and the confidence he put in me during the whole process.

I sincerely thank the members of my committee, Jasbir Arora, Colby Swan, Asghar Bhatti, and Christopher Stoakes, who have aided in my advancement in knowledge.

I would like to express my deepest gratitude to my parents who provided me support during my journey.

ABSTRACT

The present work introduces novel methodologies for damage detection and health monitoring of structural and mechanical systems. The new approach uses the angular velocity inside different mathematical forms, via a gyroscope, to detect, locate, and relatively quantify damage. This new approach has been shown to outperform the current state-of-the-art acceleration-based approach in detecting damage on structures. Additionally, the current approach has been shown to be less sensitive to environmental acoustic noises, which present major challenges to the acceleration-based approaches. Furthermore, the current approach has been demonstrated to work effectively on arch structures, which acceleration-based approaches have struggled to deal with. The efficacy of the new approach has been investigated through multiple forms of structural damage indices.

The first methodology proposed a damage index that is based on the changes in the second spatial derivative (curvature) of the power spectral density (PSD) of the angular velocity during vibration. The proposed method is based on the output motion only and does not require information about the input forces/motions. The PSD of the angular velocity signal at different locations on structural beams was used to identify the frequencies where the beams show large magnitude of angular velocity. The curvature of the PSD of the angular velocity at these peak frequencies was then calculated. A damage index is presented that measures the differences between the PSD curvature of the angular velocity of a damaged structure and an artificial healthy baseline structure.

The second methodology proposed a damage index that is used to detect and locate damage on straight and curved beams. The approach introduces the transmissibility and coherence functions of the output angular velocity between two points on a structure where

damage may occur to calculate a damage index as a metric of the changes in the dynamic integrity of the structure. The damage index considers limited-frequency bands of the transmissibility function at frequencies where the coherence is high. The efficacy of the proposed angular-velocity damage-detection approach as compared to the traditional linear-acceleration damage-detection approach was tested on straight and curved beams with different chord heights. Numerical results showed the effectiveness of the angular-velocity approach in detecting damage of multiple levels. It was observed that the magnitude of the damage index increased with the magnitude of damage, indicating the sensitivity of the proposed method to damage intensity. The results on straight and curved beams showed that the proposed approach is superior to the linear-acceleration-based approach, especially when dealing with curved beams with increasing chord heights. The experimental results showed that the damage index of the angular-velocity approach outweighed that of the acceleration approach by multiple levels in terms of detecting damage.

A third methodology for health-monitoring and updating of structure supports, which resemble bridges' bearings, is introduced in this work. The proposed method models the resistance of the supports as rotational springs and uses the transmissibility and coherence functions of the output response of the angular velocity in the neighborhood of the bearings to detect changes in the support conditions. The proposed methodology generates a health-monitoring index that evaluates the level of deterioration in the support and a support-updating scheme to update the stiffness resistance of the supports. Numerical and experimental examples using beams with different support conditions are introduced to demonstrate the effectiveness of the proposed method. The results show that the proposed method detected changes in the state of the bearings and successfully updated the changes in the stiffness of the supports.

PUBLIC ABSTRACT

The present work introduces new methodologies for finding the damage of structural and mechanical systems. This approach uses the rate of change of the angular position (angular velocity) inside different mathematical forms, via a gyroscope, to detect, locate, and relatively quantify damage. This new approach has been shown to outperform the most up-to-date acceleration-based approach in finding damage on structures. Additionally, the proposed approach has been shown to be less sensitive to environmental acoustic noises, which present major challenges to the acceleration-based approaches. Furthermore, the current approach has been demonstrated to work effectively on arch structures, which acceleration-based approaches have struggled to deal with. The efficacy of the new approach has been investigated through multiple forms of structural damage indices numerically (using simulation computer work) and experimentally (using laboratory work).

TABLE OF CONTENTS

LIST OF TABLES

LIST OF FIGURES

CHAPTER ONE: INTRODUCTION AND BACKGROUND

Damage detection and health monitoring of mechanical and structural systems have become vital during recent years in many fields, including aerospace and civil engineering. They are important because early damage detection can prevent catastrophic failure in structures during their service lifespan. Also, the goal of structural health monitoring is economical; it can change the maintenance service routine by replacing periodic maintenance inspection with condition-based maintenance. For instance, by using smart monitoring systems, inspection time can be reduced by 40 percent or more for a modern fighter aircraft featuring both metal and composite structures [1]. Furthermore, autonomous health monitoring can improve safety and reliability by reducing human involvement, downtime, and human error.

Autonomous health monitoring and early detection of damage in structural systems have become popular due to the complexity of structures and the expectation for longer service life [2, 3]. Research in this area has shown that damage can be associated with changes in the physical and mechanical properties of the structures, such as the stiffness, damping, modal parameters [4], and mass [5]. Many methods have been suggested and tested toward achieving the goal of assessing the integrity of structures. Vibration-based damage methods have been considered among the most popular.

Vibration-based damage-detection methodologies [6, 7] have been used for many decades for identifying, quantifying, and locating damage in structures [8]. Some of these techniques [9-11] used the modal parameters of healthy structures as a baseline for comparison with damaged structures [12-14]. Others [4, 15-17] used the curvature of the mode shapes in identifying and localizing the damage in structures. Most existing methods have not been very

effective in detecting small damage on real-life structures but have produced reasonable results when tested on structures with relatively large damage [18, 19]. Different types of transfer functions and damage indices have been used to characterize the changes in the dynamics response of structures. One of these transfer functions, the transmissibility, showed very encouraging results [20-22]. In a recent article, Schallhorn and Rahmatalla [23] used the changes in the transmissibility to monitor the health condition of a highway bridge (Highway 30) in Iowa.

Vibration-based damage-detection methods can be classified as baseline or non-baseline methods. The latter do not require an undamaged healthy structure for comparison. Ratcliffe [16] presented a frequency response function and curvature for locating damage in structures. The curvature of the displacement, extracted from the measured frequency response function of the damaged structures, was used as a damage indicator. The healthy structure was modeled with a local or global curve fitting of the damage data. Rucevskis et al. [24] proposed a method based on mode shape curvature for identification and localization of damage in a plate-like structure. The damage index (DI) of the method is identified as the absolute difference between the measured curvature of the damaged structure and a smooth polynomial representing the curvature of the healthy structure.

The transmissibility is an output-only function and can be measured as the response ratio between two locations on the structure. The transmissibility is expected to measure the local changes in the structure since it contains valuable information about the dynamic characteristics of the structure represented by the anti-resonance frequencies [25]. Some researchers [23, 26, 27] have noted that the transmissibility has some uncertainties in detecting real changes in the dynamic properties of the structure in real-life field applications. These uncertainties can be related to the distance between the collected responses, the changes in the environmental

parameters, the intensity of damage, and the location and magnitude of the applied forces. It has been suggested that at a certain frequency band or at peaks of the transmissibility function that have less sensitivity to noise and environmental effects, the transmissibility function can be more effective in detecting structural integrity [22, 28, 29]. Schallhorn and Rahmatalla [23] used the coherence as a guide to select the frequency bands in the transmissibility function to monitor the health condition of a highway bridge (Highway 30) in Iowa.

For a reliable structural health-monitoring process, the sensor system used to acquire and collect the data is a significant component. Accelerometers constitute the majority of sensors traditionally used in most vibration-based damage-detection methods. When accelerometers are attached to the structural components, the expectation, based on the linear theory, is that they measure the acceleration of a point on the structure in the correct direction—the gravity direction, for example, for vertical measurements. Under operational loading, structural components, such as long beam-like components, would mostly undergo bending types of deflection. This deflection can be relatively geometrically large under heavy loading, and therefore the direction of the acceleration measurement may encounter some errors. With different operational loadings, it is expected that the degree of deflection will be different. The differences in the measured direction could generate uncertainties in the decision making of the health-monitoring algorithm. Also, accelerometers are shown to be very sensitive to acoustic noises in the surrounding environments, and their accuracy may be at risk under these conditions [30-34]. On the other hand, rotational measurements, using gyroscopes, for example, present a more consistent and direct way to measure the changes in the rotational motion and deflection of the structural components under different loading conditions.

Vibration-based damage-detection methodologies based on angular velocity are presented in the current work. These methodologies have been tested through numerical and experimental analyses. The contribution of the proposed work is to obtain a damage index to monitor the healthy condition of a structure or mechanical systems in a more effective manner than the current state-of-the-art approaches. The thesis is organized as follows: Chapter Two presents damage detection using the angular velocity to detect, localize, and relatively quantify damage in structures based on the changes in the second spatial derivative (curvature) of the power spectral density (PSD) of the angular velocity during vibration. Chapter Three presents an approach to detect damage on structural systems with a straight beam shape; the approach uses the transmissibility and coherence functions of the output angular velocity between two points on a structure where damage may occur to calculate a damage index as a metric of the changes in the dynamic integrity of the structure. Chapter Four includes an experimental study of the effect of acoustic noise on transmissibility-based damage detection using angular velocity versus acceleration. Chapter Five presents a numerical investigation of the performance of the presented approach of measurement on the damage indices and compares it with one that uses accelerations for the curved beam structures. A health monitoring of structural bearing and model updating is presented in Chapter Six to study the feasibility of the proposed methodology for the assessment of the boundary condition of a beam structure with the presence of noise. Both numerical and experimental work have been implemented to fulfill this purpose.

CHAPTER TWO: DAMAGE DETECTION USING POWER SPECTRAL DENSITY CURVATURE

2.1. Introduction

This chapter presents a non-destructive damage-detection technique that uses the changes in the power spectral density (PSD) of the angular velocity of beam-like structures as an indicator of damage. The proposed method uses the changes in the curvature of the PSD of the angular velocity at different selected locations on the beam. The proposed method can be considered a non-model-based approach, as it does not need a model of the structure to work with. Also, the method is a non-baseline method, as it does not need the undamaged healthy structure for comparison.

2.2. Theoretical Background

Structures normally comprise many beam-like elements where damage may take place. When accelerometers are attached to a structure to measure the changes in motion in some direction, mostly in the vertical gravity direction, there is a possibility that the acceleration measurements will not be in the intended direction, especially when large geometrical displacements exist. On the other hand, gyroscopes can measure the angular velocity $\dot{\theta}$ of the structure at a different location, and that measurement is immune when large geometrical changes take place.

When the health condition of the structure is changing due to changes in stiffness, similar to acceleration, the angular velocity is also expected to sense these changes. While the changes in the angular velocity can be small and hard to detect, especially when environmental noises exist, the second spatial derivatives ($\dot{\theta}_i''$) of the angular velocity will be used. $\dot{\theta}_i''$ can be determined numerically using the central differences method as shown in Equation 2-1.

$$\dot{\theta}_i'' = \frac{\dot{\theta}_{i+1} - 2\dot{\theta}_{i+1} + \dot{\theta}_{i-1}}{h^2} \tag{2-1}$$

where h is the distance between locations i+1 and i-1, where the angular velocity measurement is conducted.

The damage index (DI) in this work will be represented by the absolute difference between the curvature of the angular velocity of the damaged structure and that of the healthy structure, as shown in Equation 2-2:

$$DI = \left| \dot{\theta}''_{damage} - \dot{\theta}''_{healthy} \right| \tag{2-2}$$

While experimental and environmental noises are always expected to affect the magnitude of the real measured angular velocity signals, it becomes more convenient to look at locations in the angular velocity signal where the signal-to-noise ratio is as large as possible. One way to do that is to look at the PSD of the angular velocity signal and determine the peaks where the PSD is at its maximum. The peaks in the PSD graph normally represent the resonance frequencies where a large amount of energy is trapped in the system and where the deformation is expected to be large. Accordingly, the damage index will be calculated at these subsequent peak frequencies in the PSD graph.

The first step in the proposed damage-detection method is to determine the magnitude of the angular velocity at the peaks in the PSD curve at different locations on the structure. The second step is to calculate the curvature of the angular velocity at these peak frequencies using the central differences method of Equation 2-1. The final step is to calculate the difference between the curvature of the angular velocity at these peaks with those of the undamaged (healthy or baseline) structure as shown in Equation 2-3.

$$DI = \frac{1}{n}\sum_{i=1}^{n}\left|PSD_i''(\dot{\theta})_{damage} - PSD_i''(\dot{\theta})_{healthy}\right| \tag{2-3}$$

where n is the number of peak frequencies in the PSD signal, and $PSD_i''(\dot{\theta})$ is the normalized PSD curvature magnitude at the peak frequency (i). If the healthy data is available, then the damage index can be calculated using Equation 2-3. Otherwise, an artificial smooth, healthy PSD curvature curve can be generated from the PSD curvature of the damage data using a curve-fitting technique [16].

2.3. Experimentation and Results

2.3.1. Numerical Example (Simply Supported Beam)

To establish the feasibility of the method, a pin-ended beam was created inside the commercial finite element software ABAQUS/CAE 6.12 using 200 beam elements (2D planar with wire base feature and linear line element type B21). The beam was one meter in length and had a rectangular cross-section of 0.0762 m * 0.00635 m. It was made from steel with a density of 7860 (kg/m3) and a Young's Modulus of 200 GPa and was considered healthy or undamaged. The beam was loaded with an impulse point loading of 10 N/s at 0.2m from its left support as shown in Figure 2-1.

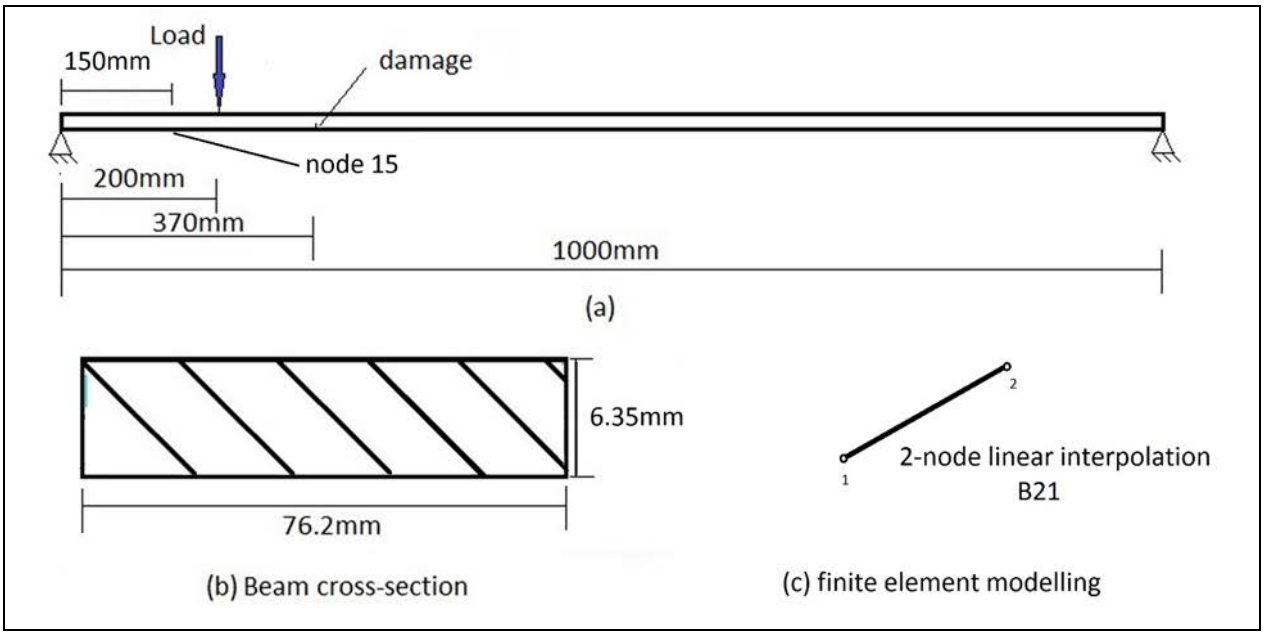

Figure 2-1 (a) Schematic representation of the pin-ended beam used in the numerical experiments and the locations of the applied load, node 15, and damage area, (b) dimension of the cross-sectional area of the beam, and (c) finite element beam model used in the analysis.

A damage 10 mm in length was then created on the beam 0.371 m from the left support of the beam by reducing the stiffness of the element from 200 GPa to 194 GPa as shown in Figure 2-1. This reduction in the stiffness represents 3% of the original element stiffness. The damaged beam was subjected to an impact loading similar to that used with the healthy beam. In both the healthy and damaged cases, the angular velocity of the beam was measured at different nodes across the beam length. The distance between each measurement node is 0.01 m. The PSD of the angular velocity of the healthy and damaged structures were calculated to identify the natural frequencies of the beams. For illustration purposes, node 15, which is located 0.15 m from the left support, was selected as an example of the time domain signal of the angular velocity on the beam (Figure 2-2a and Figure 2-2b).

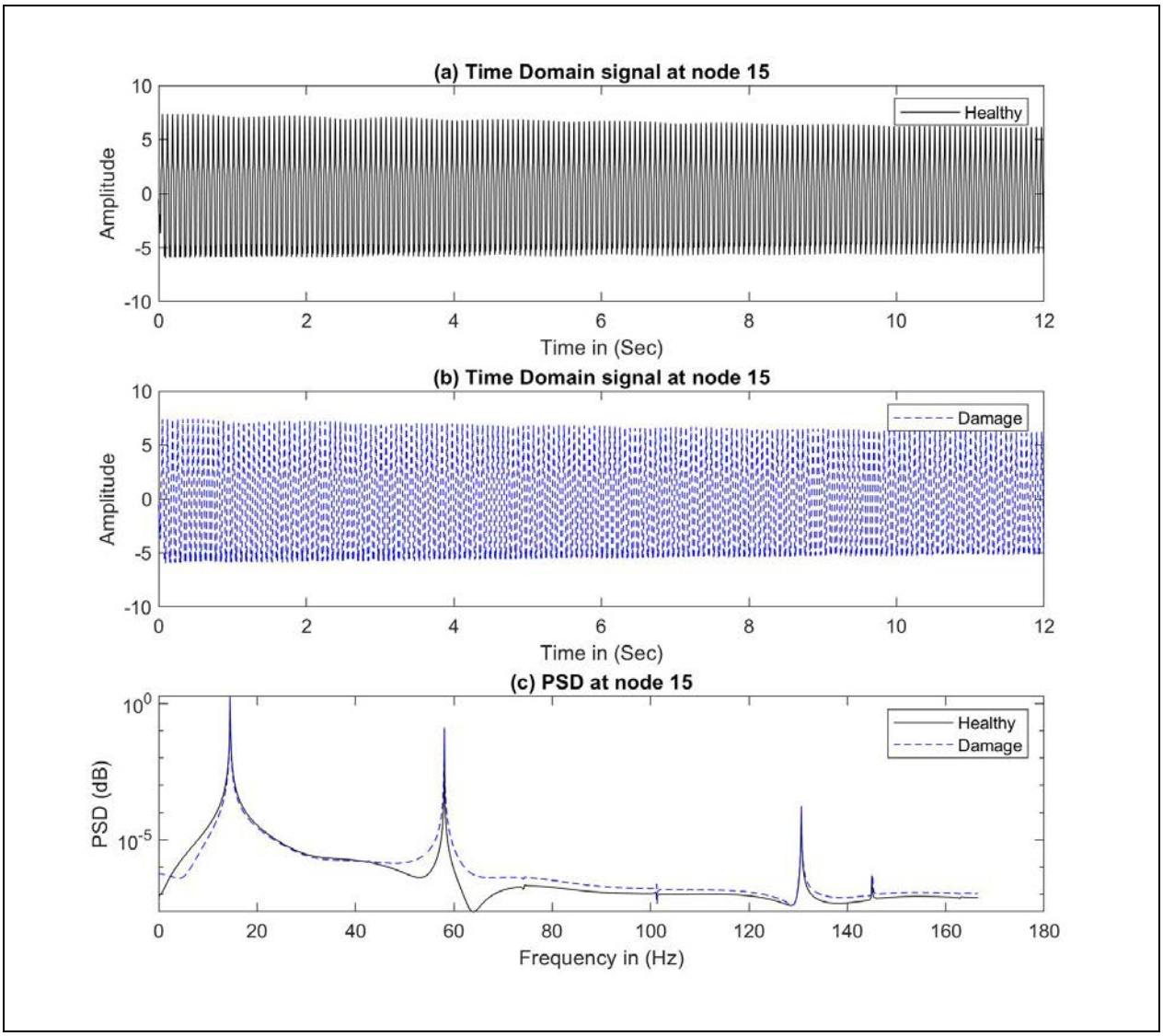

Figure 2-2 (a) Time history of the amplitude of the angular velocity signal at node (15) for the healthy beam, (b) time history of the amplitude of the angular velocity signal at node (15) for the damaged beam, (c) power spectral density plot of the angular velocity at node (15) for the healthy and damaged beams.

Figure 2-3 shows the PSD magnitude of the healthy and damaged beams at the different nodes at the first, second, and third natural frequencies. As is evident in Figure 2-3, it is not easy to differentiate between the PSD graphs of the healthy and damaged beams at the three natural frequencies.

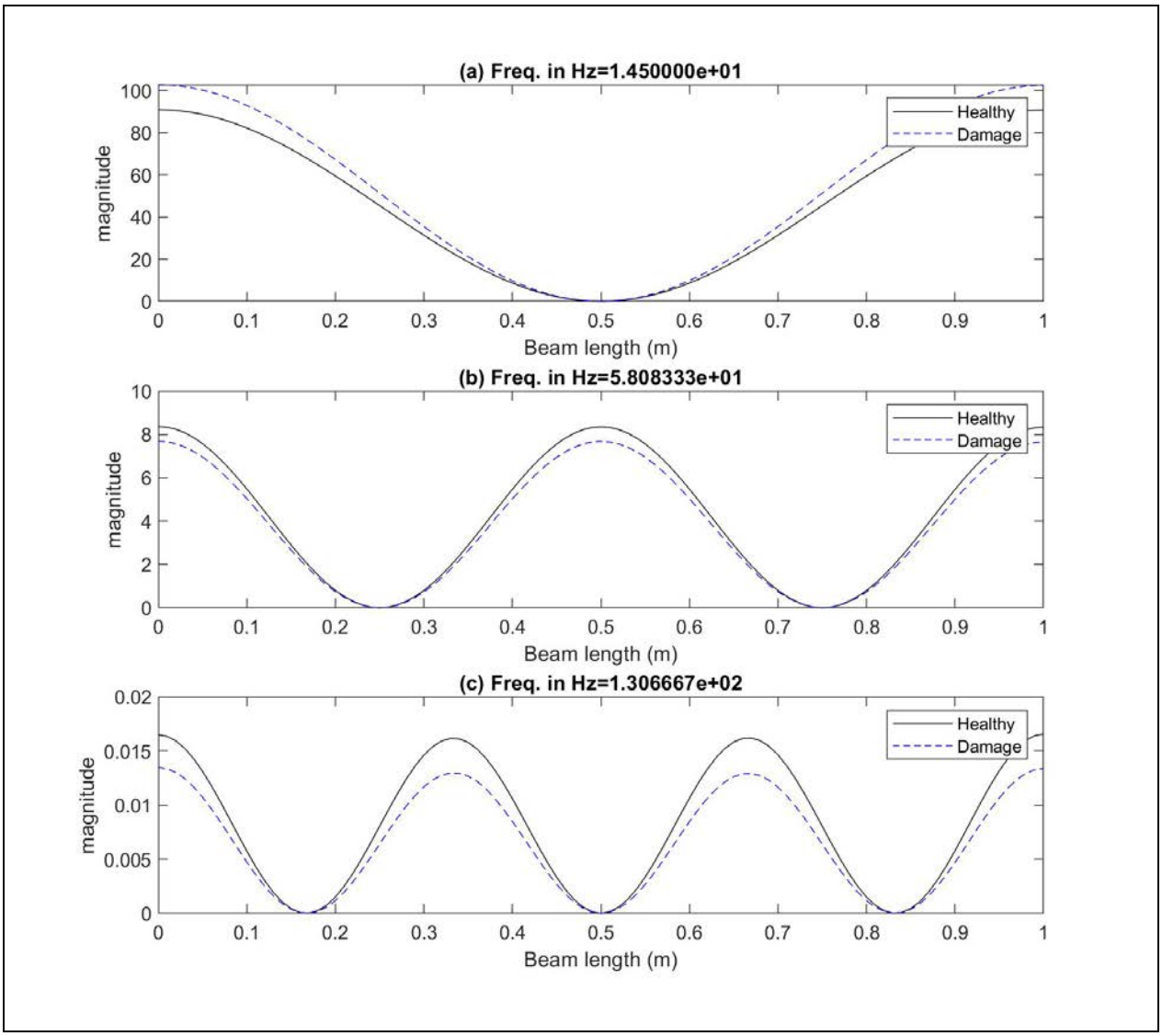

Figure 2-3 Power spectral density magnitude of the angular velocity of the healthy and damaged beams at different nodes across the beam at (a) the first peak frequency, (b) the second peak frequency, and (c) the third peak frequency.

The difference between the PSD graphs of the healthy and damaged beams becomes clearer with the PSD curvature graphs shown in Figure 2-4. The jumps in the PSD curvature graphs of the damaged beam took place at the locations where the damage existed, indicating that the PSD curvature graphs are more sensitive to local damage than the PSD graphs. In addition, the jump in the PSD curvature graph was obvious at the selected three natural

frequencies. The size of the jump was prominent at the first natural frequency and became smaller at higher frequencies.

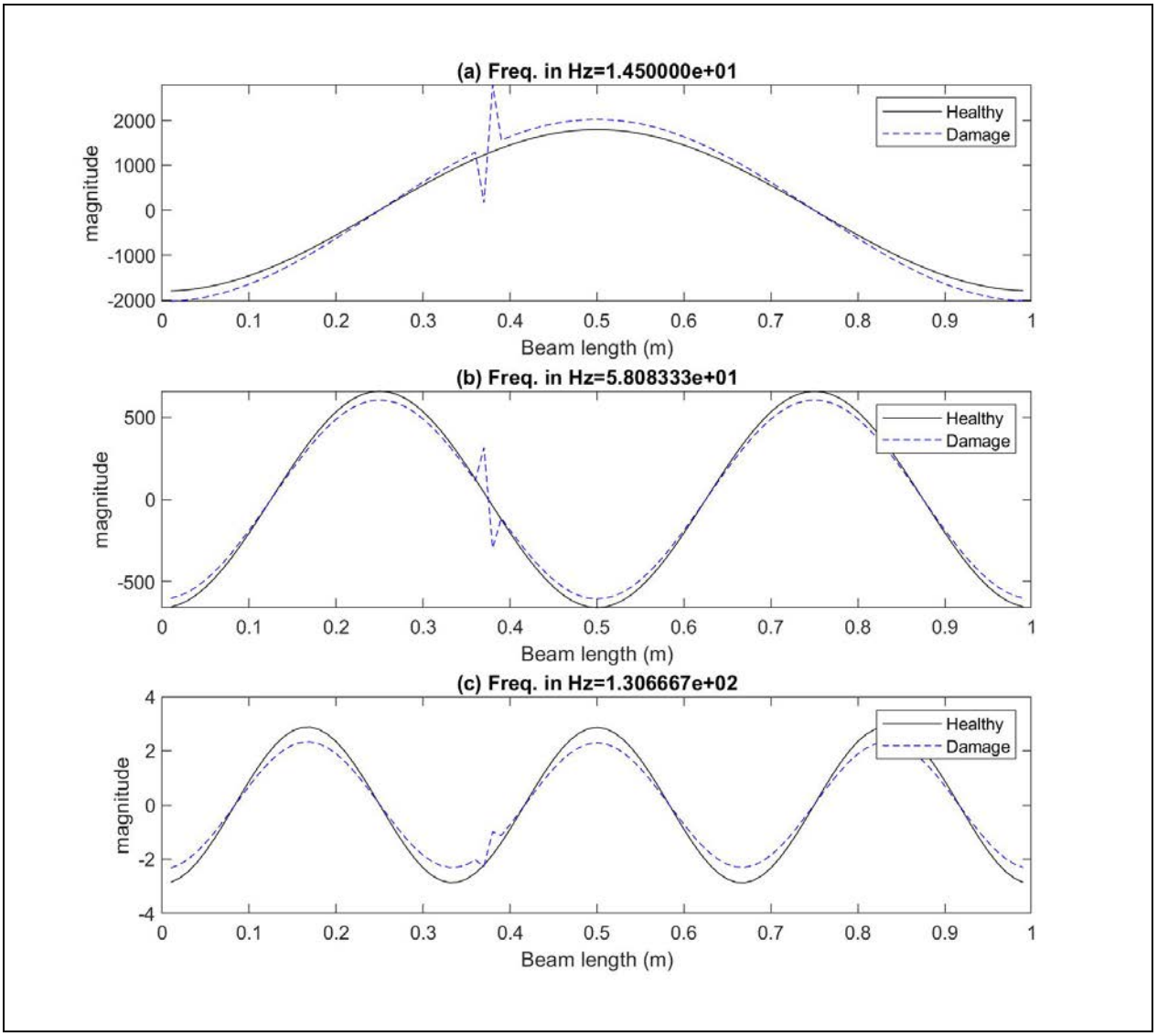

Figure 2-4 Power spectral density curvature of the angular velocity of the healthy and damaged beams across the beam length at (a) the first peak frequency, (b) the second peak frequency, and (c) the third peak frequency.

Figure 2-5 clearly shows a high magnitude of the damage index at the location of the damage at the different natural frequencies. This shows the capability of the proposed damage-detection method in identifying and localizing damage. The damage index can be based on the

magnitude of the first natural frequency only (Figure 2-5a), or it can be added from the different natural frequencies and produce a total number that represents the damage index (Figure 2-5d).

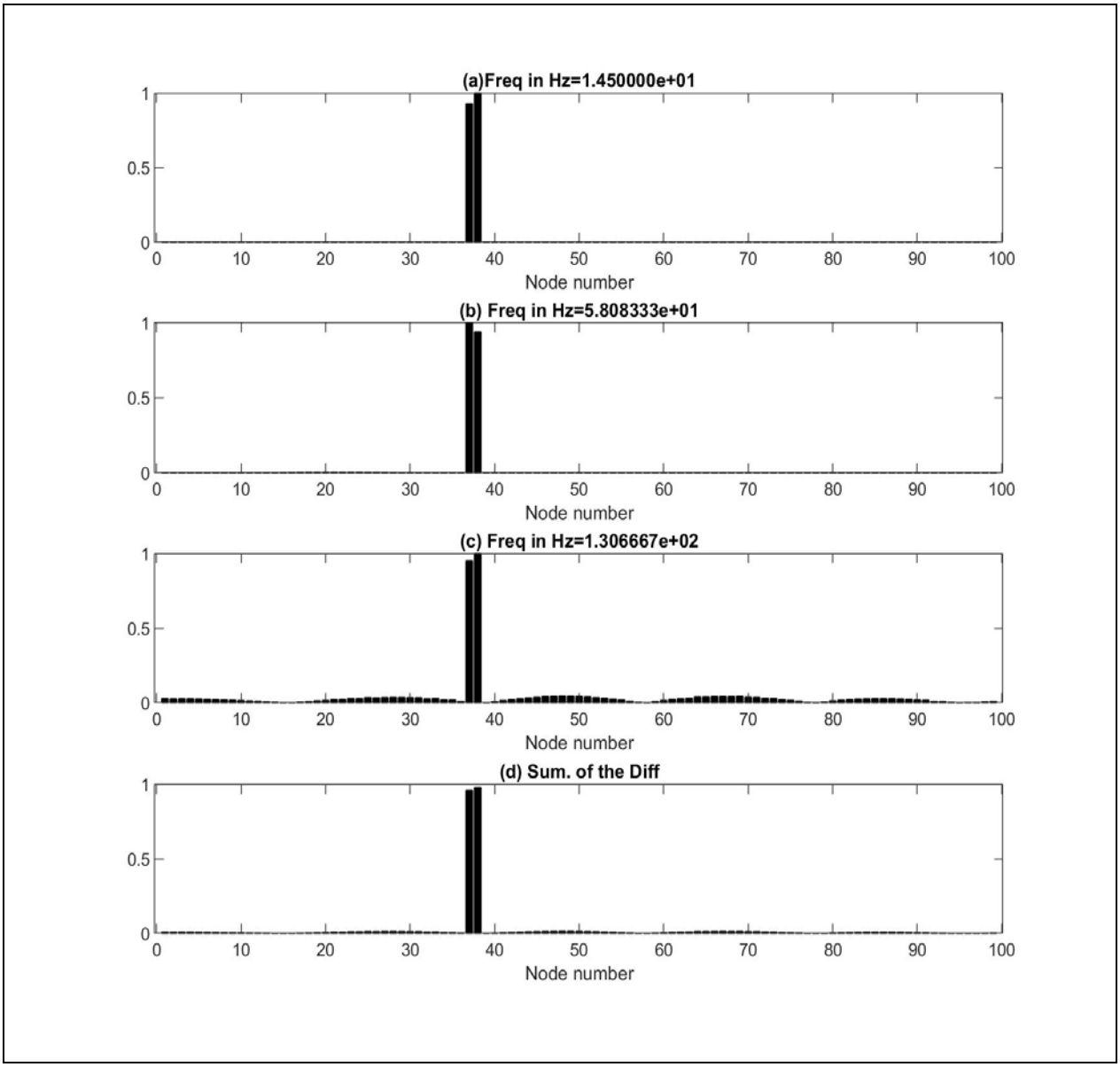

Figure 2-5 Magnitude of the damage index across the beam at (a) the first peak frequency, (b) the second peak frequency, and (c) the third peak frequency; (d) the sum across the three peak frequencies.

2.3.2. Effect of Added Noise

The example presented earlier will be revisited in this section, but with added noise. Two levels of noise will be considered. In the first level, a 5% white noise will be added to the measured angular velocity signal in the time domain. To increase the signal-to-noise ratio, the impact point load was increased to 100 N/s. Figure 2-6 shows the PSD curvature graphs at the peak frequencies. With this level of noise, one can clearly see the jumps in the PSD curvature graphs at the damage location at the different frequencies; however, additional artificial peaks are also seen at different locations at the three natural frequencies.

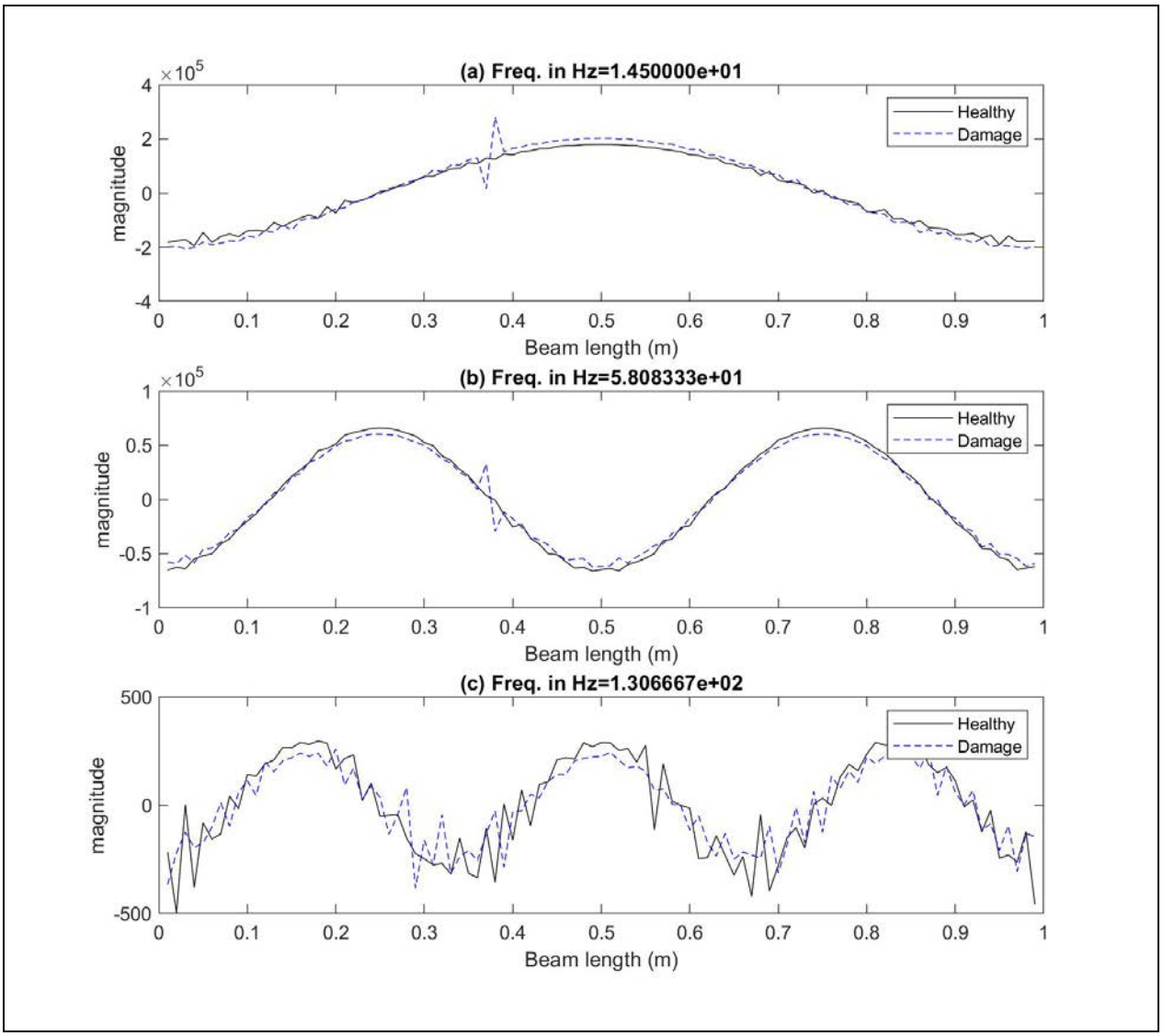

Figure 2-6 Power spectral density curvature of the angular velocity at the three peak frequencies of the healthy and damaged beams when 5% noise is added to the signal.

The damage index of the graphs in Figure 2-6 is demonstrated in Figure 2-7. As shown in Figure 2-7, the damage index at the three natural frequencies showed a high peak at the location of the damage but also showed smaller peaks at different locations. However, due to the relatively small signal-to-noise ratio, the magnitude of the damage index at the third peak frequency was relatively less dominant than that at the first and second peak frequencies.

Nevertheless, the damage index sum from the three natural frequencies produced a maximum peak at the location of the damage (Figure 2-7d).

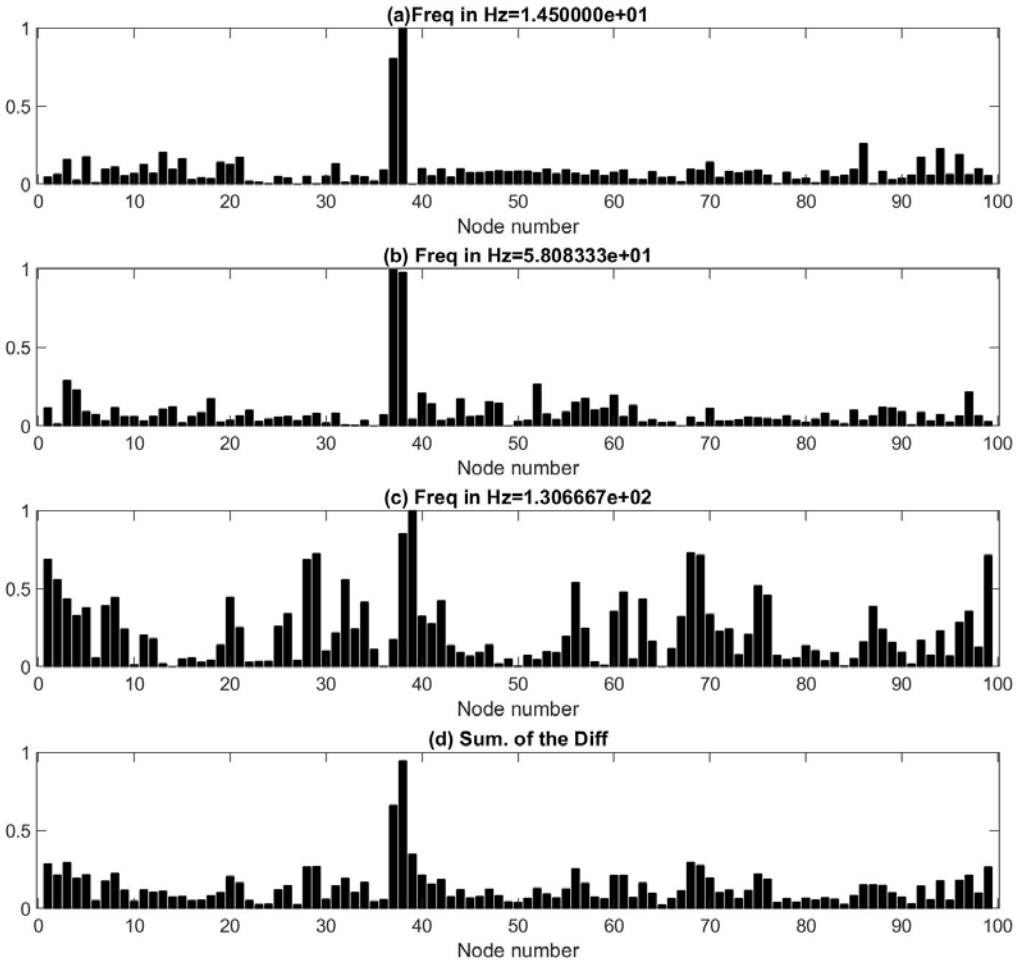

Figure 2-7 Magnitude of the damage index across the beam when adding 5% noise to the signal at (a) the first peak frequency, (b) the second peak frequency, and (c) the third peak frequency; (d) the sum across the three peak frequencies.

In the second level of noise, the same pin-ended beam was used but with an increased noise level of 10%. Figure 2-8 shows the PSD curvature at the three natural frequencies. Again, the PSD curvature graphs of the damaged beam showed prominent jumps at the location of the damage at the three natural frequencies, but also showed more jumps with high magnitude at

other locations on the beam. In spite of these anomalies, the PSD curvature graphs were able to show the largest jumps at the first and second natural frequencies (Figures 2-8a and 2-8b). With this level of noise, the jump at the third natural frequency was lower than the artificial jumps due to the noise in the signal.

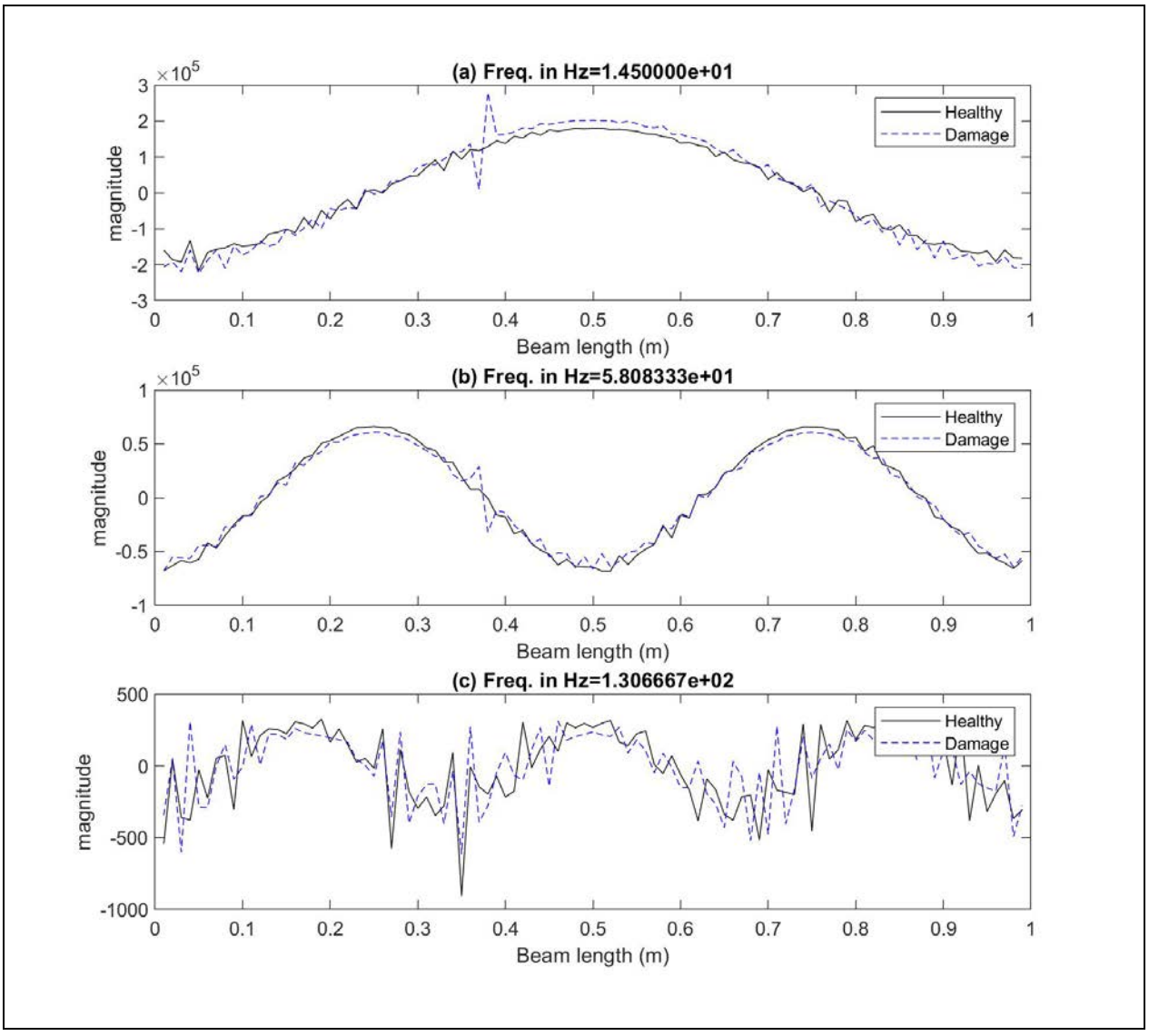

Figure 2-8 Power spectral density curvature of the angular velocity at the three peak frequencies of the healthy and damaged beams when 10% is noise added to the signal.

The damage index of the graphs in Figure 2-9 shows the damage index at the first and second natural frequencies with the highest peak at the location of the damage, but it also shows smaller peaks at different locations. In this case, the damage index magnitude at the third natural frequency was outweighed by the artificial peaks at different locations on the beam. Still, the damage index sum from the three natural frequencies produced a maximum peak at the location of the damage (Figure 2-9d) that outweighed the rest of the peaks across the beam.

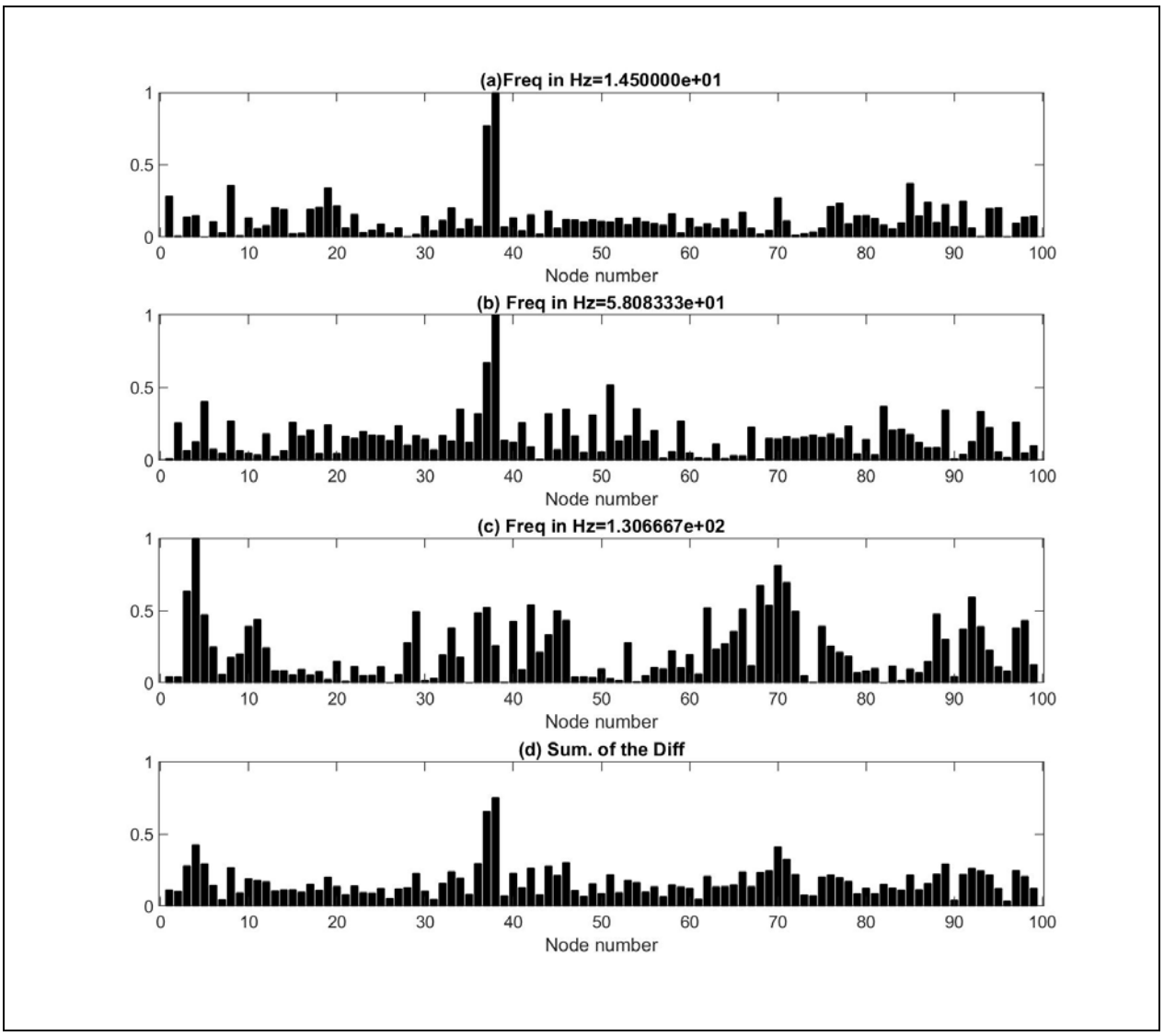

Figure 2-9 Magnitude of the damage index across the beam when adding 10% noise to the signal at (a) the first peak frequency, (b) the second peak frequency, and (c) the third peak frequency; (d) the sum across the three peak frequencies.

2.3.3. Multiple Damages

The method's capability to detect multiple damages is investigated in this section. A beam similar to the one presented earlier is used, but with damage at an element 0.01 m long at two locations. As shown in Figure 2-10, the first damage is simulated by reducing the stiffness of the element of the beam 0.37 m from the left support from 200 GPa to 194 GPa, which represents a 3% reduction of the original stiffness of the beam element. The second damage, located 0.18 m from the right support, is simulated by reducing the stiffness of the element of the beam from 200 GPa to 188 GPa, which represents a 6% reduction of the original stiffness of the beam element. The beam was loaded with an impulse loading of 10 N/s at 0.2 m from the left support, as shown in Figure 2-10.

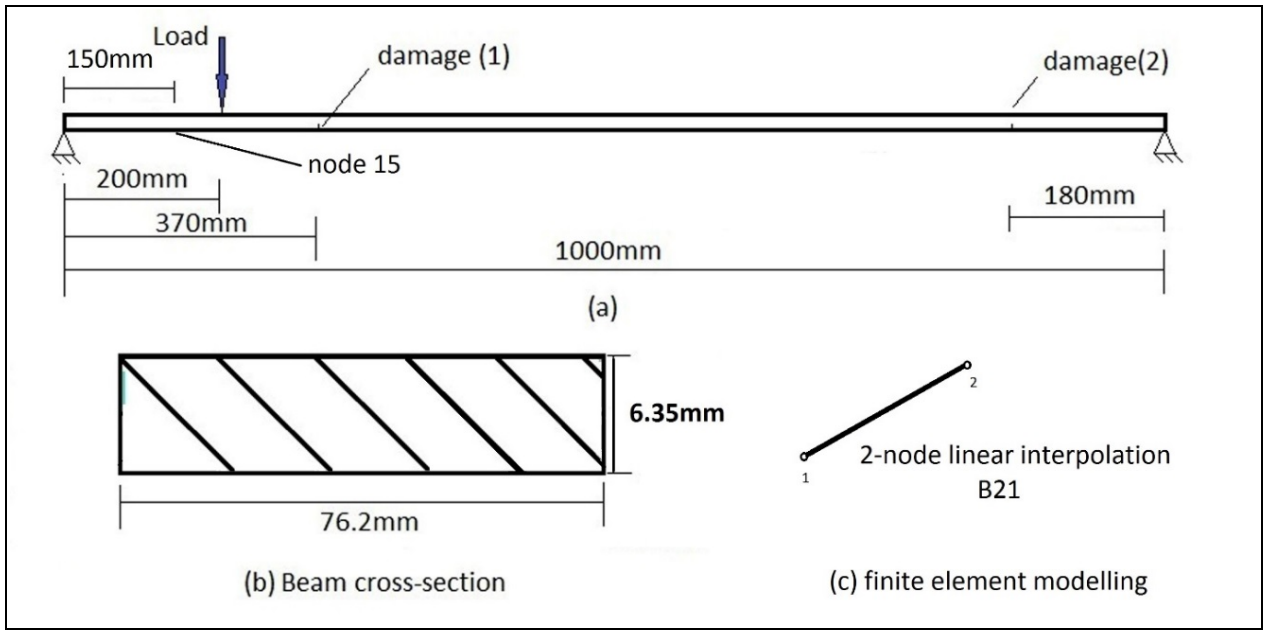

Figure 2-10 (a) Schematic representation of the pin-ended beam, used in the numerical experiments, showing the locations of the applied load, node 15, and damage area, (b) dimension of the cross-sectional area, (c) finite element beam model used in the analysis.

The PSD plots of the damaged and healthy beams at node 15 are shown in Figure 2-11. Figure 2-12 shows the damage index for this multiple-damage condition. The damage index showed two prominent bars at the locations of the damage at the three peak frequencies. This indicates that the proposed method is capable of detecting and locating multiple damages on the beam. The method was also capable of quantifying damage, as can be seen in Figures 2-12a, 2-12b, and 2-12c. The damage index sum (Figure 2-12d) was able to identify, locate, and relatively quantify the level of damage on the different locations on the beam.

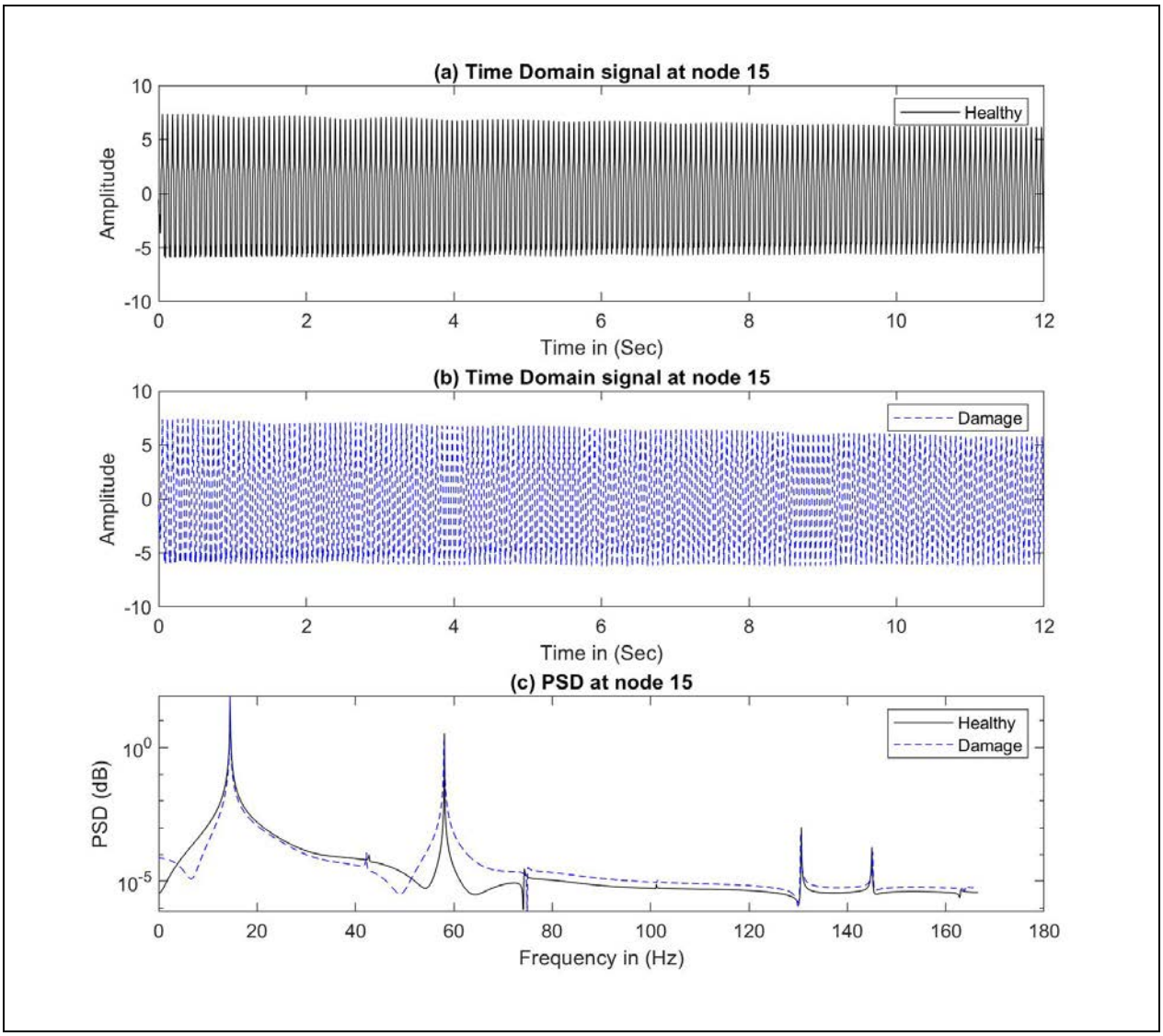

Figure 2-11 Power spectral density plot of the healthy and damaged (at two locations) beams at node (15).

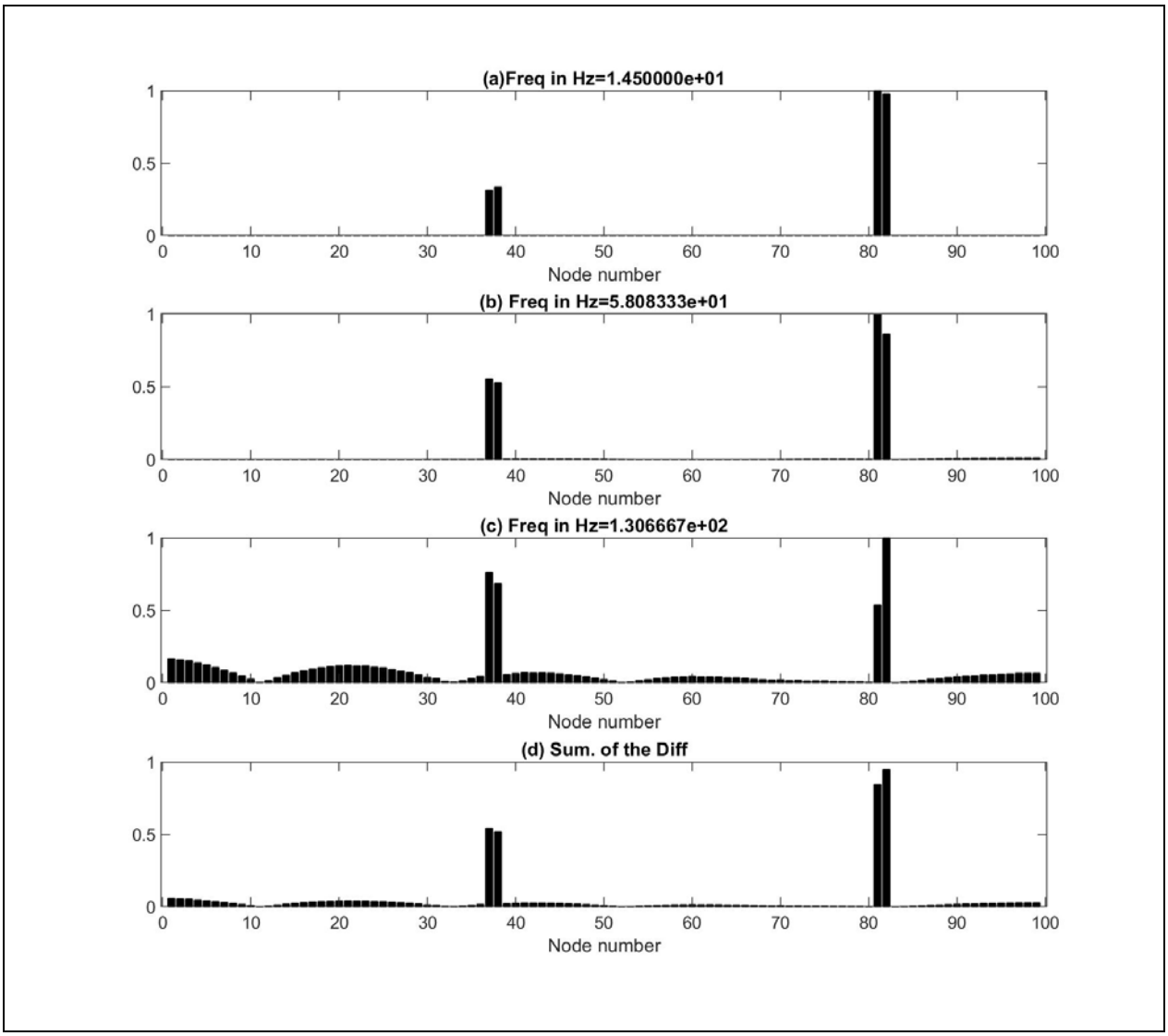

Figure 2-12 Magnitude of the damage index across the beam with two damage areas at (a) the first peak frequency, (b) the second peak frequency, and (c) the third peak frequency; (d) the sum across the three peak frequencies.

2.3.4. Numerical Example (Cantilever Beam)

A rectangular cantilever beam is presented in this section with the purpose of comparison with the experimental cantilever presented in the next section. The cantilever beam was created with 316 beam elements (2D planar with wire base feature and linear line element type B21) using the finite element software ABAQUS/CAE 6.12. The length of the beam is 0.790 m with a rectangular cross-section of 0.075 m * 0.006 m. The material of the beam is steel with a density of 7860 (kg/m3) and a Young's Modulus of 200 GPa. The beam was loaded with an impulse point loading of 100 N/s 0.025 m from its free end as shown in Figure 2-13. Damage was created at 0.355 m from the left support of the beam by reducing the depth of a 5 mm long slot from 0.006 m to 0.004 m as shown in Figure 2-13.

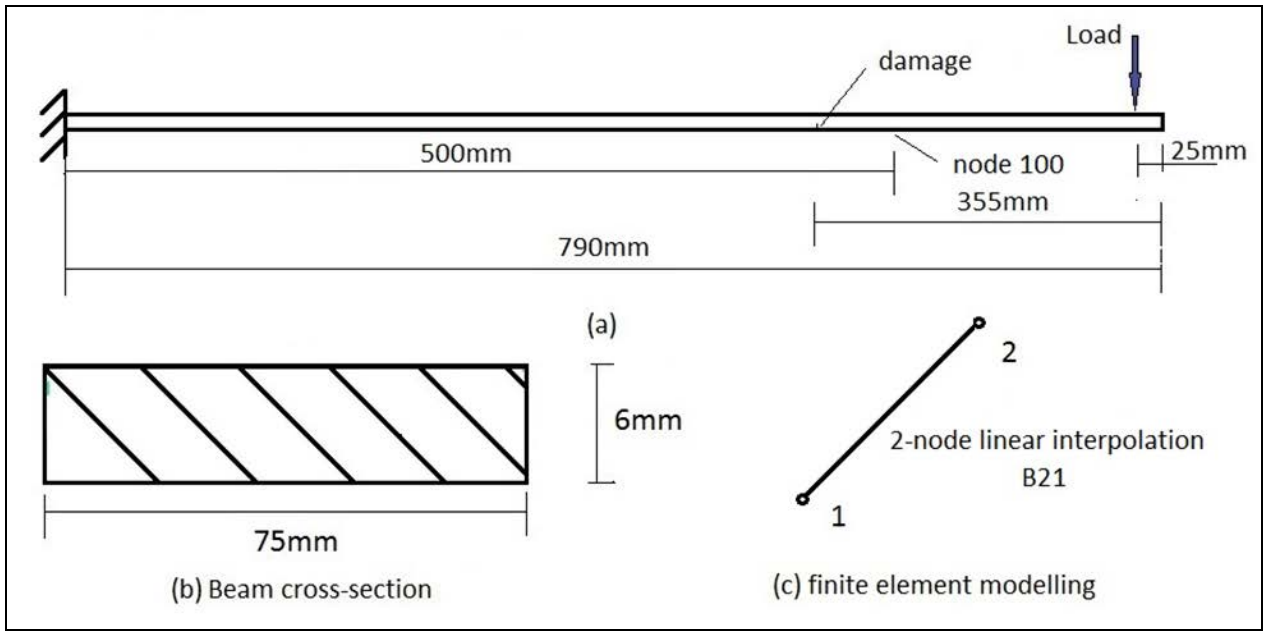

Figure 2-13 Schematic representation of the cantilever beam used in the numerical experiments with the load and damage locations, (b) dimension of the cross-sectional area, and (c) finite element beam model used in the analysis.

For illustration, node 100 (which is located 500 mm from the left support) has been selected to show an example of the time domain signal of the angular velocity of the healthy and damaged beams (Figures 2-14a and 2-14b) as well as their PSD graphs (Figure 2-14c). Figure 2-15 shows the PSD magnitude of the healthy and damaged beams at the different nodes across the beam at the first, second, and third natural frequencies.

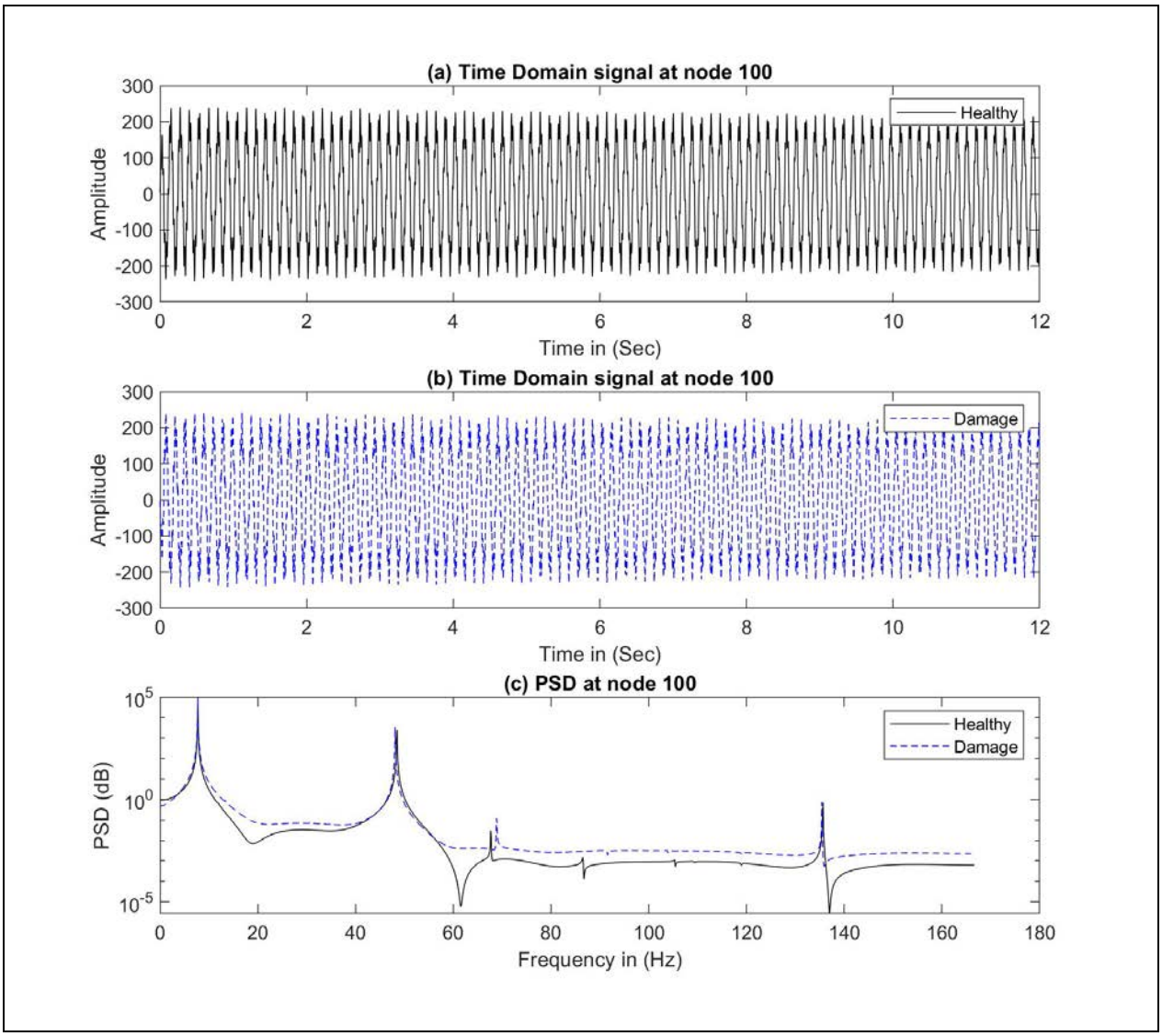

Figure 2-14 (a) Time history of the amplitude of the angular velocity signal at node (100) for the healthy beam, (b) time history of the amplitude of the signal at node (100) for the damaged beam (slot damage), (c) power spectral density plot at node (100) for the healthy and damaged beams.

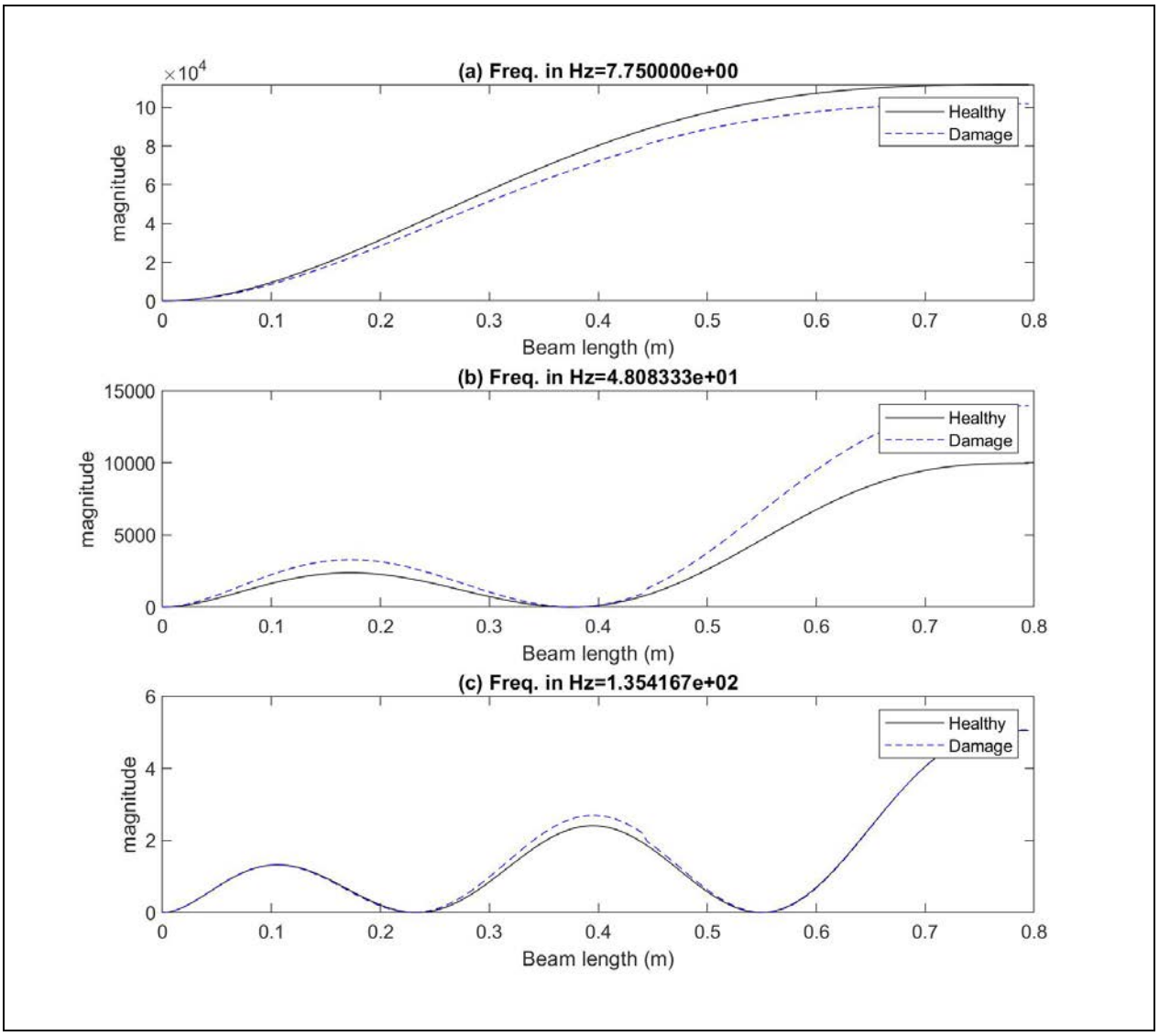

Figure 2-15 Power spectral density magnitude of the angular velocities of the healthy and damaged beams at the different nodes across the beam at (a) the first peak frequency, (b) the second peak frequency, and (c) the third peak frequency.

The difference between the PSD graphs of the healthy and damaged beams becomes clearer with the PSD curvature graphs shown in Figure 2-16. The jumps in the PSD curvature graphs of the damaged beam took place at the locations where the damage existed, indicating that the PSD curvature graphs are more sensitive to local damage than the PSD graphs.

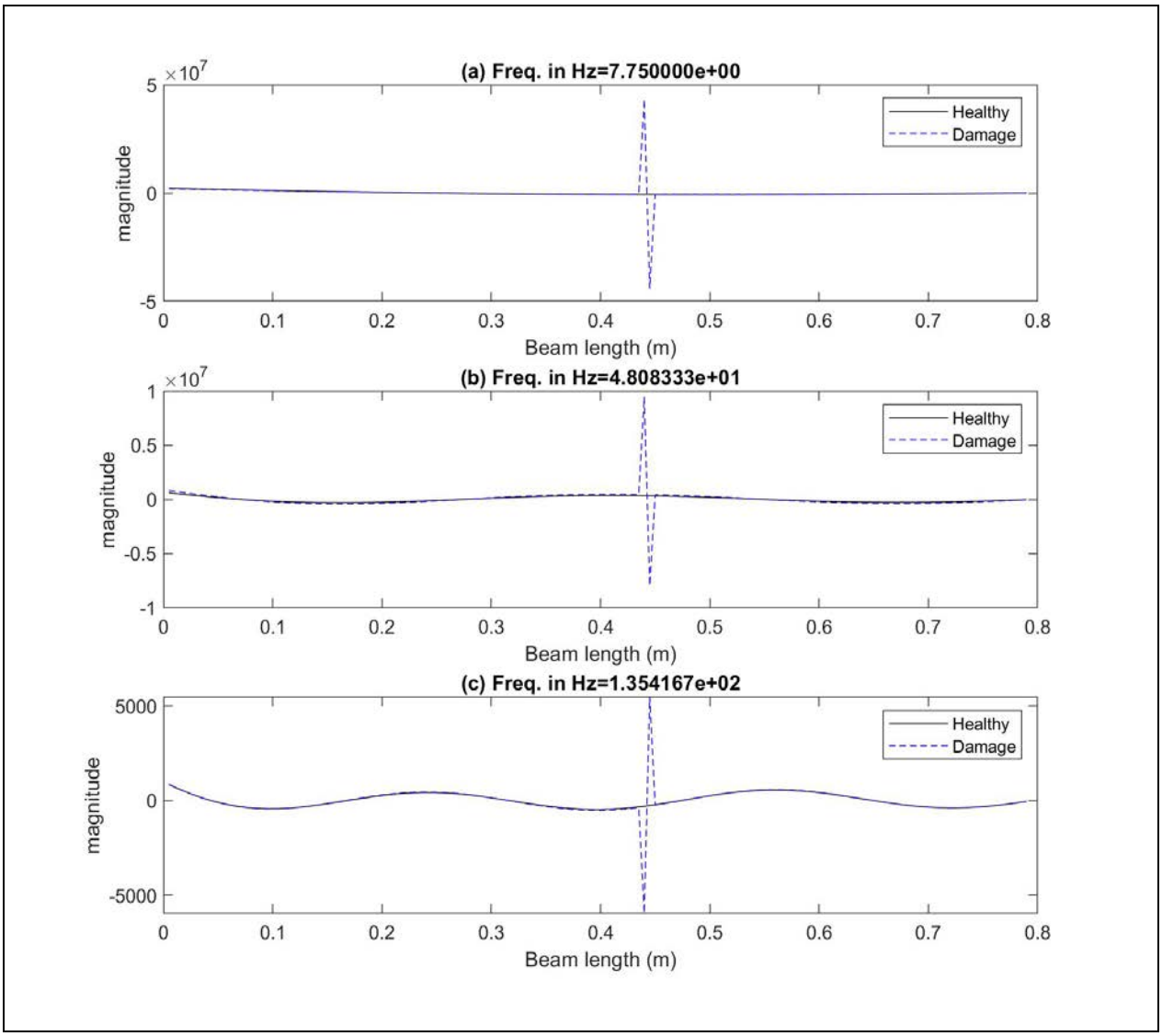

Figure 2-16 Power spectral density curvature of the angular velocity of the healthy and damaged beams across the beam length at (a) the first peak frequency, (b) the second peak frequency, and (c) the third peak frequency.

Figure 2-17 shows the magnitude of the damage index at the different natural frequencies (7.75, 48.33, and 135.58 Hz) across the beam length. This demonstrates the capability of the proposed damage-detection method in identifying and localizing the damage.

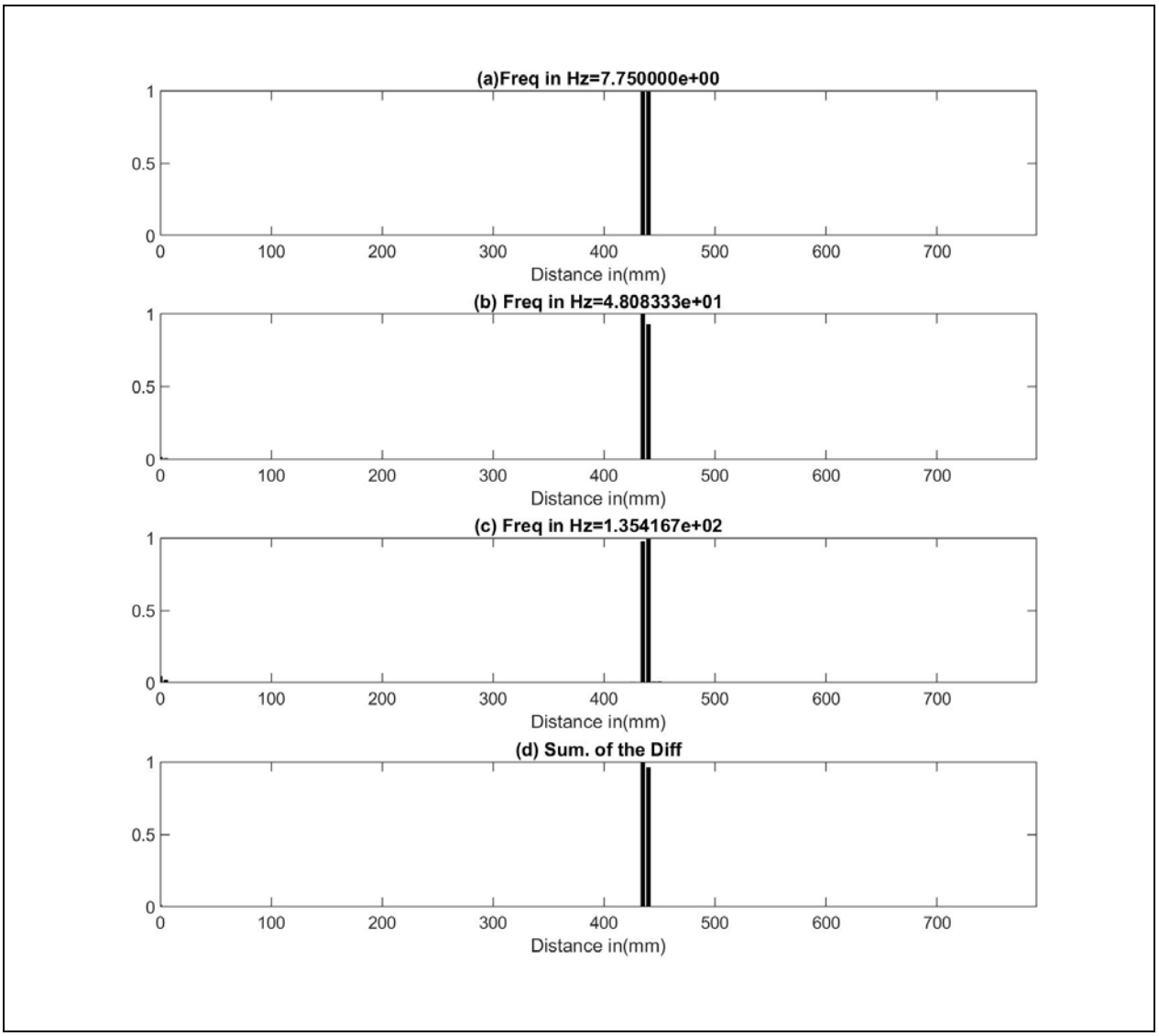

Figure 2-17 Magnitude of the damage index across the beam at (a) the first peak frequency, (b) the second peak frequency, (c) the third peak frequency, and (d) the sum across the three peak frequencies.

2.3.5. Experimental Example

In the laboratory experiments, it is easier to measure the angular velocity in comparison with the angular displacement. The results in this section will be based on the measurement of the angular velocity at different locations on the beam structure. A rectangular cantilever steel beam with dimensions of 790 x 75 x 6 mm was selected, as shown in Figure 2-18. Fourteen gyroscopes inside inertial sensors with a sampling rate of 60 frames per second were used to measure the angular velocity at a distance of 50 mm between each sensor across the length of the beam. The weight of each inertial sensor is 24 g. An impact load was applied at a distance of 25 mm from the far free end of the cantilever. Ten measurements were conducted for each experiment, and three scenarios were selected to establish the feasibility of the method in detecting damage. In the first scenario, a healthy cantilever beam was used, and the angular velocities were collected at each sensor under each of the ten impacts. In the second scenario, the cantilever beam was damaged at a distance of 355 mm from the free end by introducing a slot across the width of the beam. The slot had a width of 2 mm and a depth of 2 mm. The angular velocities were then measured under ten impact-loading conditions. In the third scenario, the depth of the slot was increased from 2 mm to 4 mm. Again, the angular velocities were collected at each sensor for ten impacts.

Figure 2-18 Experimental setup of the cantilever beam in the laboratory showing the locations of the fourteen sensors across the cantilever beam.

The PSD values of the angular velocities for the three scenarios were then calculated to identify the locations of the natural frequencies. The mean values of the PSD associated with the 10 impact loadings of the three scenarios are shown in Figure 2-19. Because of the boundary and environmental noises and the relatively low sampling rate of the sensors used in the experiments, uncertainties will be raised regarding the accuracy of the data at higher frequencies that may include the second natural frequency. The damage index magnitude of the second natural frequency of the experimental data was outweighed by that of the noise. For this reason, the damage index in this example will be presented in terms of the PSD curvature of the first natural frequency only.

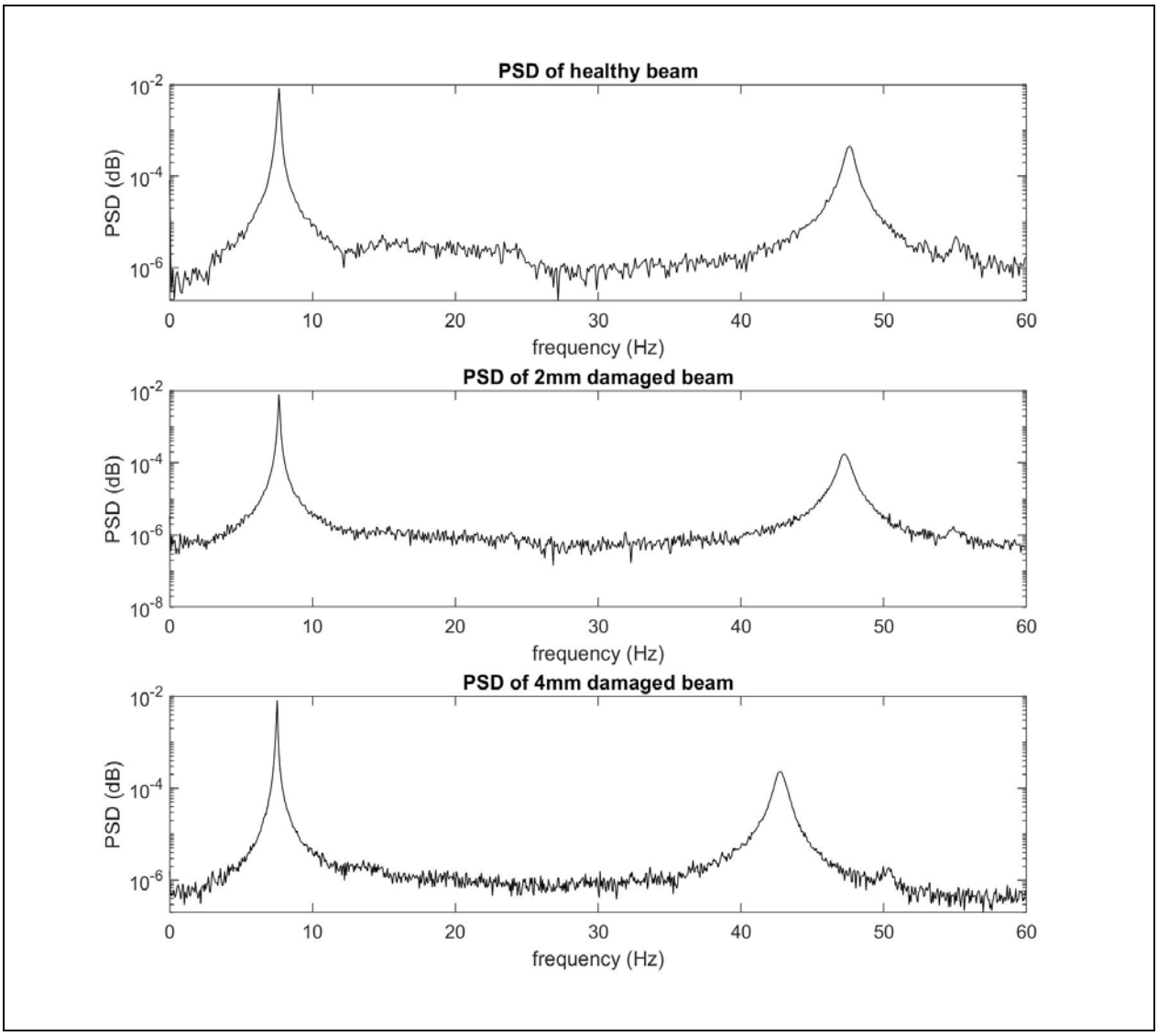

Figure 2-19 Power spectral density of the cantilever beam: (a) healthy beam, (b) damaged beam with a slot 2 mm wide and 2 mm deep, and (c) damaged beam with a slot 2 mm wide and 4 mm deep.

Figure 2-20a shows the PSD magnitude at the first peak of the PSD of the angular velocity for the healthy beam, a damaged beam with a 2 mm slot, and a damaged beam with a 4 mm slot. The PSD curvatures of these scenarios are shown in Figure 2-20b. Figure 2-20c shows the damage index at the first natural frequency for the three scenarios. It is evident that the resulting damage index with the largest magnitude occurred at the location of the crack, indicating that the method is able to detect and locate the damage. Small bars are also seen at

different locations on the beam but with smaller magnitudes. Also, the damage index magnitude for the 2 mm cracks was smaller than that of the 4 mm cracks, indicating that the method can differentiate between the severities of damage but not necessarily quantify the damage.

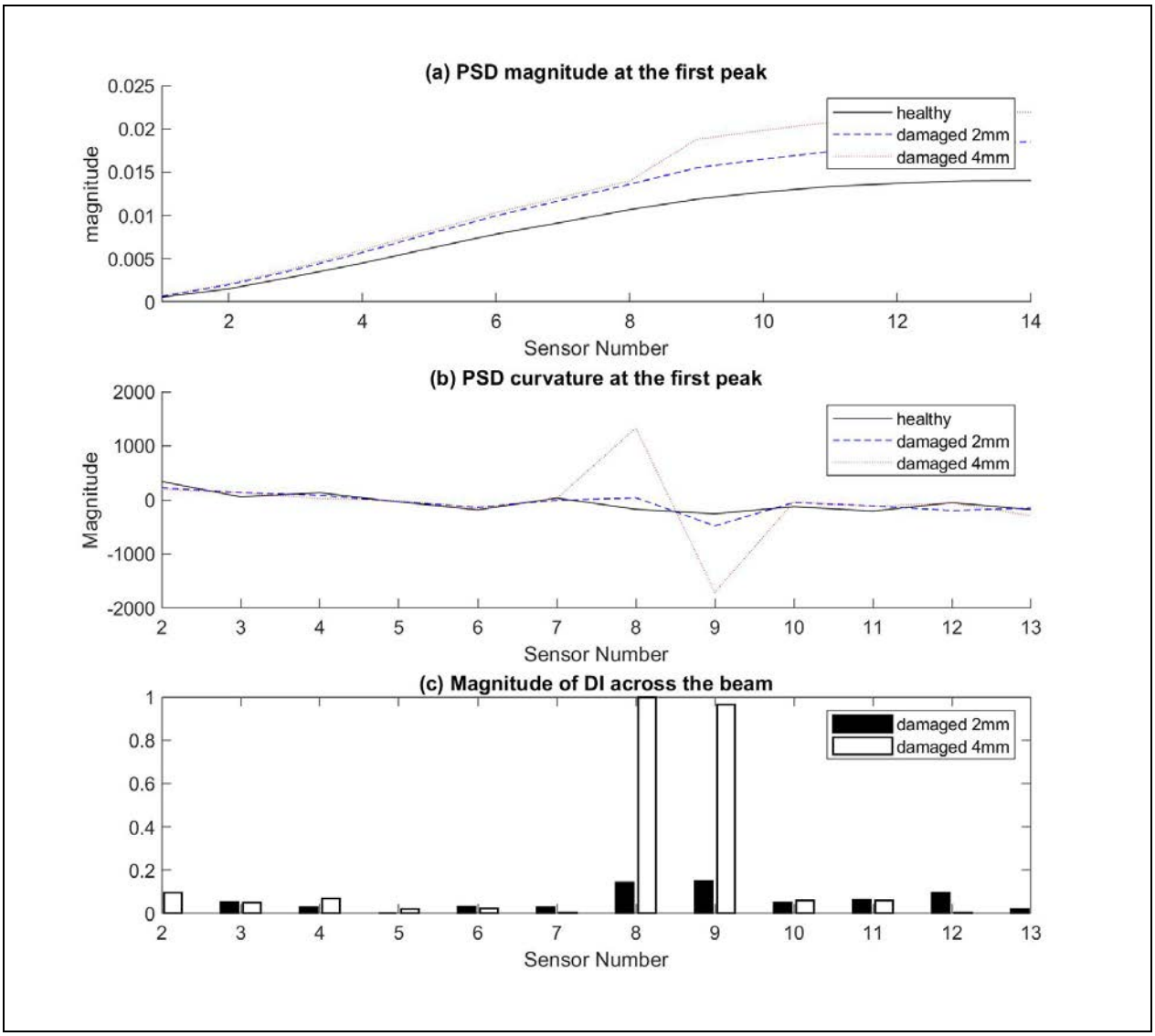

Figure 2-20 (a) Power spectral density magnitude of the angular velocities of the healthy and damaged beams across the beam at the first peak frequency, (b) power spectral density curvature of the angular velocity at the first peak frequency of the healthy and damaged beams, (c) magnitude of the damage index across the beam. The dark bar represents the damaged beam with a slot 2 mm wide and 2 mm deep, and the white bar represents the damaged beam with a slot 2 mm wide and 4 mm deep.

2.4. Discussion and Conclusion

This chapter introduced a new approach to capture the changes in the properties of beam structures in a more direct way using the angular velocity. This avoids the uncertainty encountered in the traditional acceleration-based measurements where the direction of measurements is continuously changing with the operational applied loading. This type of measurement will be essential when dealing with the health monitoring of the light and long structures that are expected to be more common in future systems, especially in aerospace applications.

The proposed method is a non-model and can be a non-baseline scheme, which can be very useful when dealing with old structures where the healthy structure and a representative model are unknown. The curve-fitting approach used in this work, which is based on passing a polynomial curve through the damaged structure's PSD curvature to construct the response of the healthy structure, can suffer some difficulties when high noise presents in the measurements. This can be mitigated by selecting the deflection data only when high signal-to-noise ratio occurs, which is expected to take place under relatively large loading. For example, Lu [35] proposed a strain-based damage-detection methodology in the health monitoring of highway bridges. However, this method faced difficulties when presented with low operational loadings coming from small vehicles crossing the highway bridge that produced a low strain-signal-to-noise ratio. To circumvent this problem, Lu used the strain data that comes only from the operational loading from heavy trucks. To investigate the effect of the load's magnitude on the resulting signal-to-noise ratio, in this present work, additional numerical testing was conducted, using various impact loadings with different magnitudes. The investigation showed that, with

higher impact loads, much improvement was observed in increasing the magnitude of the damage index at the damage locations relative to the other locations on the structure.

The application of the PSD on the angular velocity data has done well in identifying the frequencies where the deflection is at its maximum. This process provided an excellent guide for focusing on these peak frequencies instead of using the whole frequency range. The second spatial derivative of the PSD at selected locations of the beam clearly showed jumps where discontinuity resulted from damage. While the method identifies the peaks' frequencies and uses them for the subsequent steps in identifying a damage index, there is a tendency, with added noise as in real-life conditions, to make the identification of the natural frequencies more challenging and to encounter some errors. Therefore, further investigations were conducted in this work by adding percentage error in the magnitude of the resulting natural frequencies and using these erroneous magnitudes in the subsequent damage-detection steps. This was done by adding ± 1 Hz to the magnitude of the first natural frequency of the simply supported beam (14.5 Hz) when 5% noise was added to angular velocity signal of the beam with 3% damage. Even with this amount of shift in the magnitude of the natural frequency, the proposed method successfully detected and located the damage. The effect of noise on the PSD curvature at higher frequencies is clearly seen when 10% noise was added to the simply supported beam in Figure 2-9, where the magnitude of the damage index produced by noise outweighed that of the third natural frequency, and therefore reduced the total magnitude of the damage index below 1. Therefore, it is suggested to use only the first natural frequency in detecting the damage when high noise is present in the system.

The results of the numerical and experimental cantilever beams showed comparable results in terms of the magnitude of the first natural frequency (7.662 and 7.75 Hz, respectively)

and the second natural frequency (47.23 and 48.08 Hz, respectively). However, the damage index magnitude of the second natural frequency of the experimental data was outweighed by that of the noise. This could be attributed in part to the limitation in the sampling rate of the sensors used in the experiments.

In conclusion, the proposed angular-velocity-based damage-detection method was able to detect, localize, and relatively quantify damage in numerical and laboratory testing even with the presence of a significant level of noise. Also, the method successfully detected multiple damages. The damage index presented in this work uses the difference between the PSD curvature of the damaged and artificial healthy structures at the different natural frequencies; the results of this work indicated successful outcomes even when using the first natural frequency only. The use of only the first natural frequency may provide a safer way to avoid the effects of the artificial jumps, which can be seen with high noise levels and low impact loads, and which can outweigh the real physical jumps.

CHAPTER THREE: TRANSMISSIBILITY BASED ON ANGULAR-VELOCITY DAMAGE DETECTION

3.1. Introduction and Background

As stated in Chapter 1, early detection of damage and health monitoring in structural systems have become more involved in the past decades to avoid unexpected failure of due service and environmental loading [2, 3]. Vibration-based damage-detection methods have been among the most popular methods of structural health monitoring. The objective of these methods is to detect and locate abnormal characteristics of structures to evaluate and extend their service lives [6-8]. Some of these methods used the modal parameters or the frequency response functions of healthy structures [9-11, 16, 17] as a baseline for comparison with the ongoing status of the structures [12-14], therefore detecting whether or not damage has occurred. The transmissibility is one practical method that showed very encouraging results [21, 26].

Most vibration-based damage-detection methodologies use accelerometers in measuring the response of the structures. Due to their high sensitivity to motion, accelerometers are considered the most prominent sensors in damage detection of structures under vibrational loadings. However, there are some drawbacks to using accelerometers. One of these drawbacks is that accelerometers are affected by vibration and sound, and thus the acoustic effects on the accuracy of accelerometer readings can become considerable in noisy environments [30]. Also, accelerometers, especially those that work the best at low frequency, such as the seismic type, measure gravity as part of their design, and therefore their readings are sensitive to their locations and orientations on the structure such as arches and curved beams. Therefore, several studies [30-33] have investigated the potential and limitations of using different sensors as an alternative or complement to accelerometers, such as dynamic strain sensors and gyroscopes in

different applications including structural health monitoring [36-39]. Sung et al. combined accelerometers and gyroscopes and developed a multi-scale sensing system for the health monitoring of structures [39]. They put many sensors on the structure and estimated the natural frequencies and deflection mode shapes using acceleration data and rotational modes using angular velocity data. They created a damage index based on the changes in the modal parameters of the structure. Castro et al. investigated the effect of acoustic noise on the performance of four types of MEMS gyroscopes [31]. They showed that the acoustic environmental noise had large effects on some sensors but did not affect others, and that it may depend on how each gyroscope is oriented inside the sensors and on the acoustic isolation method used.

In this chapter, a damage index based on the transmissibility of the angular velocity between two points on the structure is presented and compared with that based on the transmissibility of the accelerations. High coherence is adopted in the present study [23] to choose the frequency band of the transmissibility function for the damage index. Inertial sensors housing gyroscopes and accelerometers were used to measure the angular velocity and acceleration between two points near the expected damage location. Three numerical examples of simply supported, fixed-fixed beam, and cantilever beams are presented. In addition, one experimental cantilever (similar to the numerical beam) is presented to investigate the efficacy of the proposed method compared to the acceleration-based approach.

3.2. Theoretical Background

The transmissibility function in the frequency domain can be defined directly from output-only responses at two locations [25].

$$T_{ij}(\omega) = \frac{Y_i(\omega)}{Y_j(\omega)} \tag{3-1}$$

where T_{ij} is the transmissibility between node i and node j as a function of frequency(ω), Y_i is the response at location i in the frequency domain, and Y_j is the response at location j in the frequency domain. The transmissibility based on the angular velocity is introduced in this work as shown in Equation 3-2.

$$T_{ij}(\omega) = \frac{\dot{\theta}_i(\omega)}{\dot{\theta}_j(\omega)} \tag{3-2}$$

where $\dot{\theta}_i$ and $\dot{\theta}_j$ are the output angular velocities at locations i and j, respectively.

Because of the complexity of the operational loading and boundary conditions, there are certain frequency ranges where the transmissibility function has low energy and therefore cannot be determined accurately. At these ranges of frequency, it is expected that the ratio between the responses Y_i and Y_j will maintain a non-linear relationship. Thus, the coherence function is used in the present work to locate the frequency ranges where the transmissibility between i and j has meaningful linear characteristics [23]. The coherence function can be acquired through the following equation:

$$\gamma_{ij}(\omega) = \frac{|S_{ij}(\omega)|^2}{S_{ii}(\omega)S_{jj}(\omega)} \tag{3-3}$$

where γ_{ij} is the coherence between sensors at locations i and j, S_{ij} is the cross-spectral density between sensors at locations i and j, S_{ii} is the auto-spectral density of the sensor at location i, and

S_{jj} is the auto-spectral density of the sensor at location j. The coherence function is a good indicator of the changes in the characteristics of signals.

The damage index value in this work is calculated by normalizing the difference between the transmissibility of the unhealthy (damaged structure) and the transmissibility of the baseline (healthy or undamaged structure) for a chosen frequency range φ

$$DI = \frac{\left\| T_{ij}^{D}(\varphi) - T_{ij}^{BL}(\varphi) \right\|}{\left\| T_{ij}^{BL}(\varphi) \right\|} \tag{3-4}$$

where DI is the damage index value, T_{ij}^{D} is the transmissibility for the damaged structure, and T_{ij}^{BL} is the transmissibility for the baseline. The frequency range φ was chosen based on the regions of high coherence.

3.3. Numerical Testing

A study has been conducted to investigate the differences between the damage indices at two points on the structure using the angular velocity and the acceleration. Numerical models have been created and solved using the finite element software ABAQUS/CAE 6.12, and the collected responses have been handled in MATLAB (R2016A). The following subsections present examples of simply supported (pin-ended), fixed-fixed beam, and cantilever beam cases to investigate the feasibility of the proposed method.

3.3.1. Simply Supported Beam

A pin-ended beam was used for this analysis. The beam was 0.6096 m in length and had a rectangular cross-section 0.0254 m wide and 0.00635 m deep. It was made from steel with a density of 7860 kg/m3 and a Young's Modulus of 204.77 GPa. The beam was considered healthy or undamaged. The beam was loaded with an impulse point loading of 4.45 N/s 0.127 m

from its right support as shown in Figure 3-1a. A damage was introduced to the beam by reducing the stiffness at a location 0.127 m from the left end of the beam as shown in Figure 3-1a. Two levels of damage severity (5% and 10%) were introduced at the damaged element to investigate the effect of damage intensity on the resulting damage index.

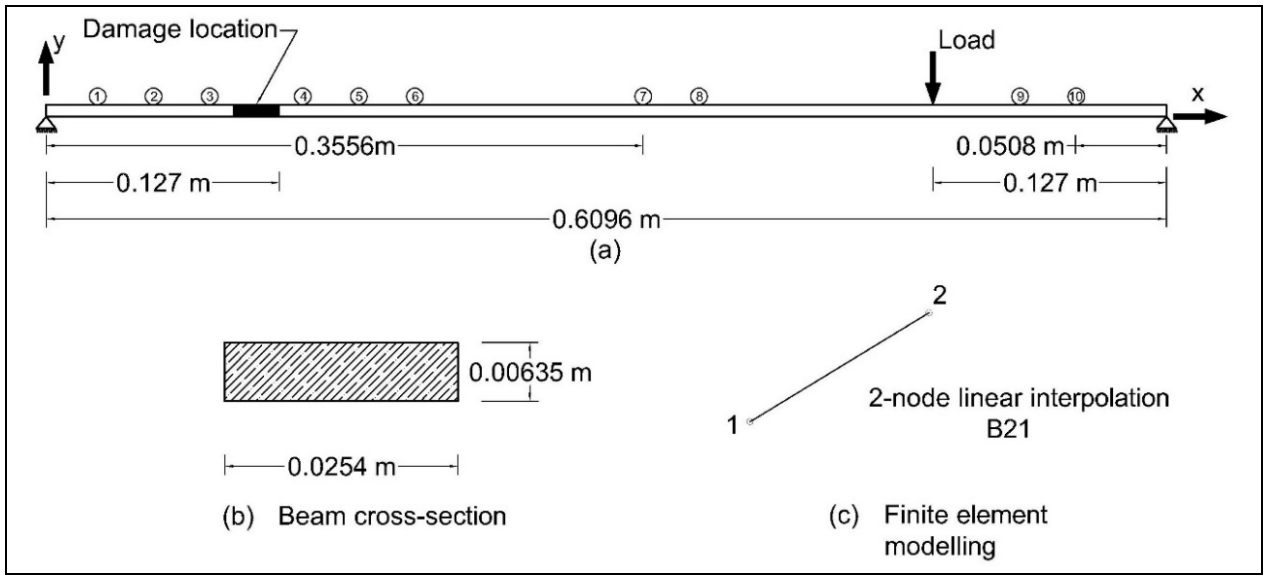

Figure 3-1 (a) Schematic representation of a pin-ended beam showing the damage location and the location of the applied load, (b) dimension of the cross-sectional area of the beam, and (c) finite element beam model used in the analysis.

In both the healthy and damage scenarios, the angular velocity and the linear acceleration responses in the time domain were measured at three pairs of nodes (1-2, 3-4, and 5-6) in the vicinity of the damage area and at two pairs of nodes (7-8 and 9-10) at remote locations from the damage area (Figure 3-1a). Figures 3-2a and 3-2b show the responses for pair 3-4 as an example. The time domain signals were taken to the frequency domain using a Blackman window (with 128 sampling points) [40] inside MATLAB (R2016a). Figures 3-2c and 3-2d show the resulting coherence functions of the angular velocity and linear acceleration of Figures 3-2a and 3-2b, respectively. Figure 3-2e shows the transmissibility function for the healthy and damage (5%) scenarios using the angular velocity, while Figure 3-2f shows the latter information when the

linear acceleration is used. A frequency band between 85-100 Hz was selected for both the angular velocity and linear acceleration since the coherence function showed a high level of linearity and was close to 1 at these frequencies, as shown in Figures 3-2c and 3-2d. The transmissibility of the healthy beam (for each pair) was considered as the baseline in the damage index.

The calculated damage index, for the 5% damage scenario, for pairs 1-2, 3-4, and 5-6, 7-8, and 9-10 using the transmissibility based on the angular velocity and the transmissibility based on acceleration, are shown in Figure 3-3. As shown in the figure, the damage indices based on the angular velocity and the acceleration were very effective in detecting the damage on the beam at pair 3-4. Additionally, the damage index at pair 3-4 is much larger than those further from the damage location, indicating that the method can localize the damage on the beam. Furthermore, the magnitude of the damage index at pair 3-4 using the angular velocity was many times higher than that using the acceleration. Figure 3-4 shows the damage indices based on the transmissibility of the angular velocity and the acceleration for the two damage scenarios (5% and 10%) considering only pair 3-4. As shown in Figure 3-4, the damage index based on the angular velocity showed larger magnitudes than that of the acceleration for both damage scenarios.

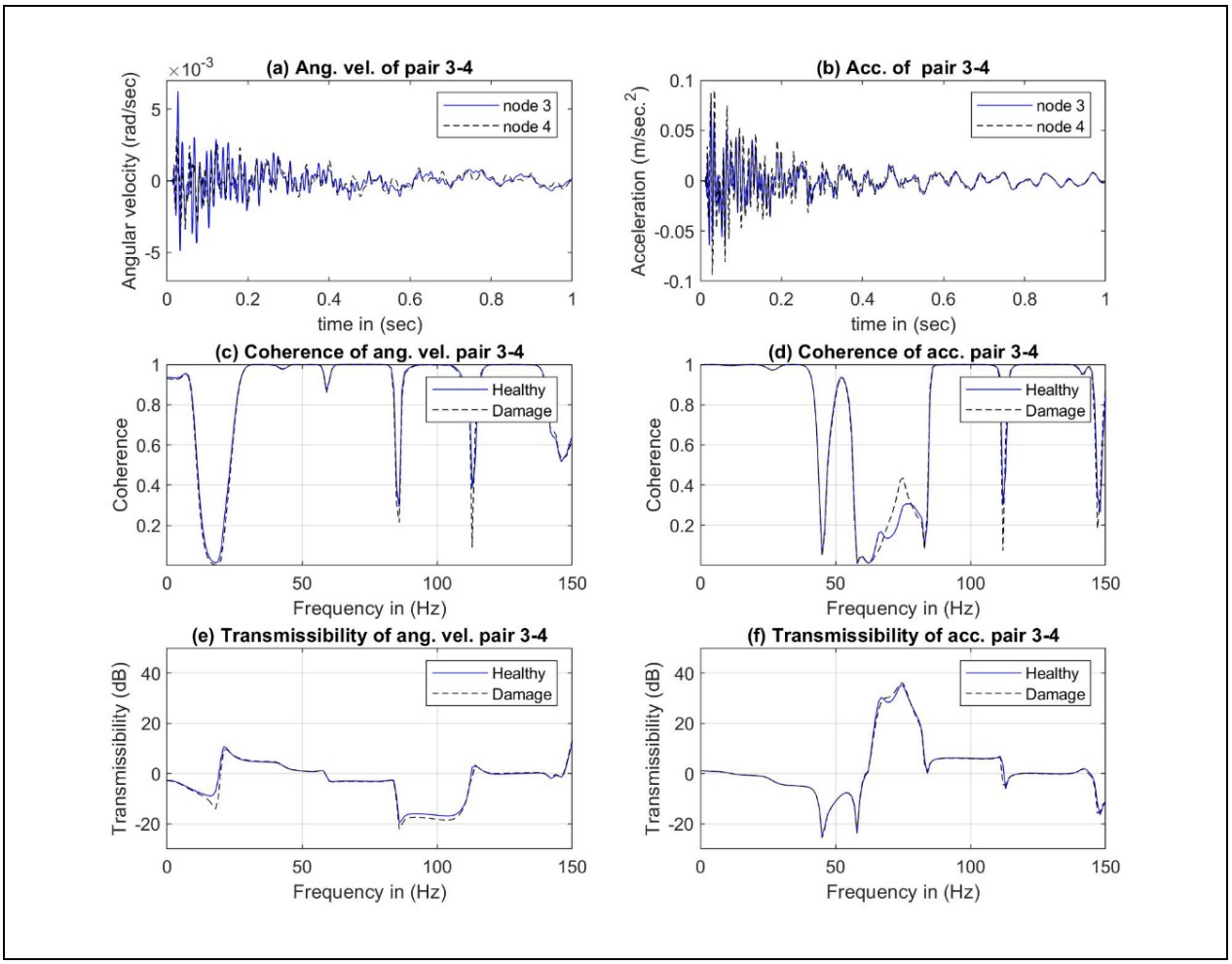

Figure 3-2 Angular velocity and linear acceleration of healthy and 5% damage beams at pair 3-4: (a) the angular velocity signal in the time domain, (b) the acceleration signal in the time domain, (c) the coherence of the angular velocity signal, (d) the coherence of the acceleration signal, (e) the transmissibility of the angular velocity, and (f) the transmissibility of the acceleration.

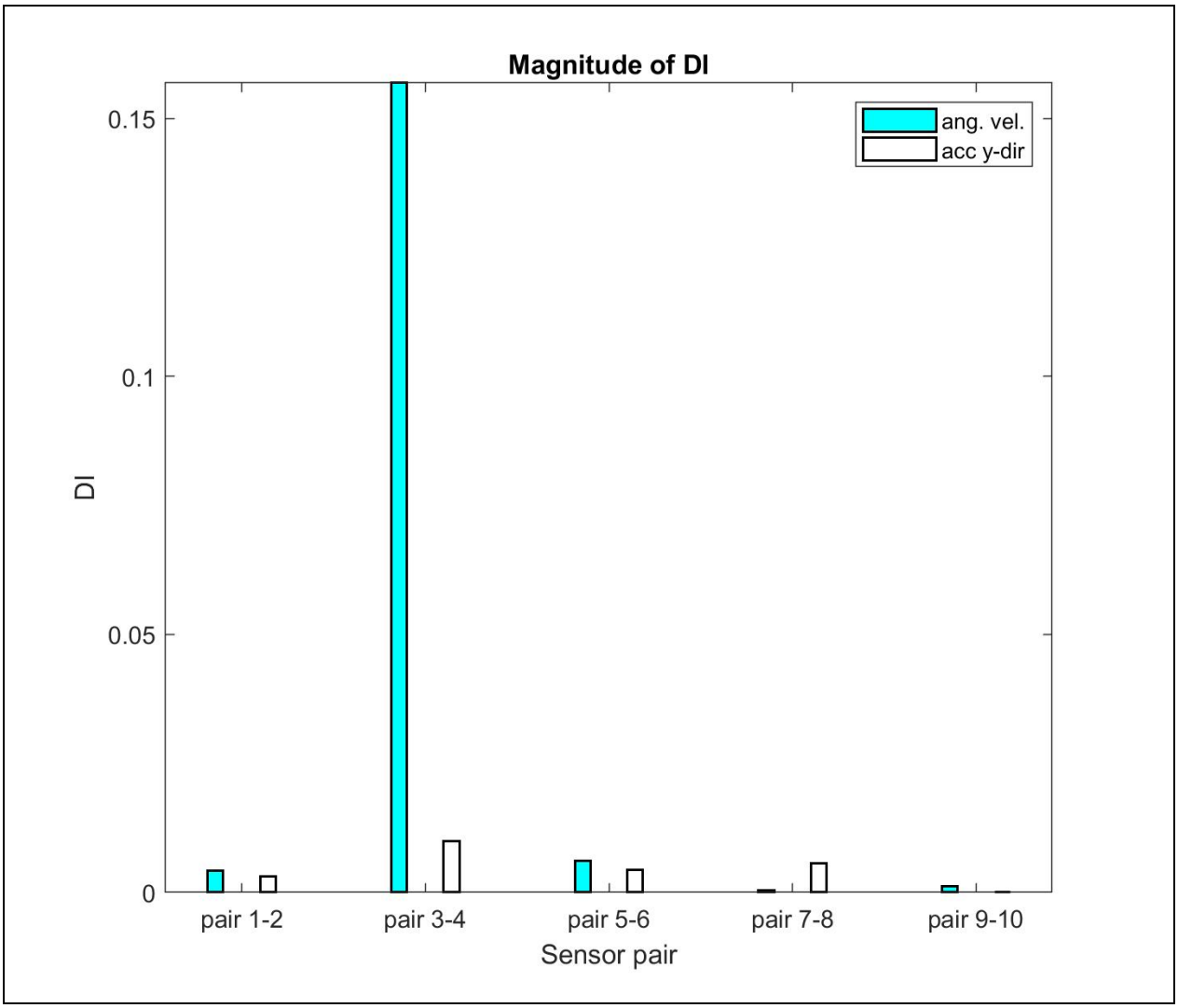

Figure 3-3 Damage index based on the transmissibility of the angular velocity and linear acceleration at pairs 1-2, 3-4, 5-6, 7-8, and 9-10 on the beam, for the case of 5% reduction in stiffness at pair 3-4.

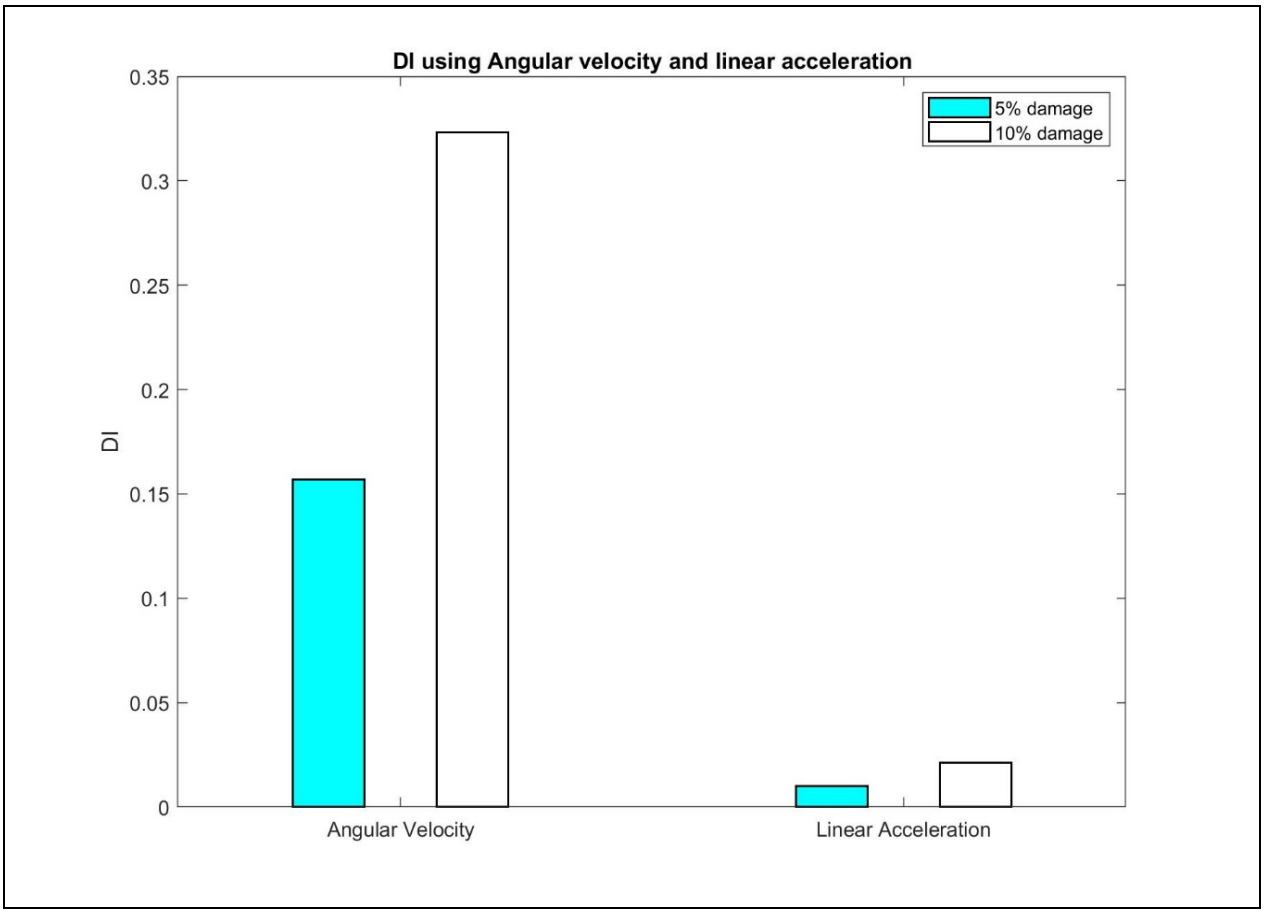

Figure 3-4 Damage index based on the transmissibility of the angular velocity and linear acceleration calculated for the case of the 5% and 10% reduction of stiffness between pair 3-4 (damage location).

The methodology presented in this example can be extended to a real-life situation where sensors can be permanently attached on the structure at the location where damage may occur, and data obtained from the sensors can be streamed and used to calculate the transmissibility and coherence functions and then a damage index. Structural failure can be triggered when a sudden change or jump in the damage index is observed.

3.3.2 Fixed-Fixed Beam

A study has been conducted on a numerical beam to investigate the sensitivity of the transmissibility based on the angular velocity damage index and compare it with that based on the acceleration. A numerical model of a fixed-fixed beam has been created and solved using the finite element software ABAQUS/CAE 6.12 using 20900 elements (8-node quadratic element type S8R as shown in Figure 3-5c), and the collected responses have been handled in MATLAB (R2016A).

A fixed-ended beam was used for this analysis. The beam was 0.8 m in length and had a rectangular cross-section 0.0381 m wide and 0.00635 m deep. It was made from steel with a density of 7800 kg/m3 and a Young's Modulus of 210 GPa. The beam was considered healthy or undamaged. The beam was loaded with an impact point loading of 1 N/s 0.4 m from its right support as shown in Figure 3-5a. A damage was introduced to the beam by reducing the stiffness at a location 0.325 m from the left end of the beam as shown in Figure 3-5a. Six levels of damage severity (1%, 0.5%, 0.1%, 0.05%, 0.01%, and 0.005%) were introduced at the damaged element (length of 0.000781 m) to investigate the sensitivity of the method to the damage intensity on the resulting damage index.

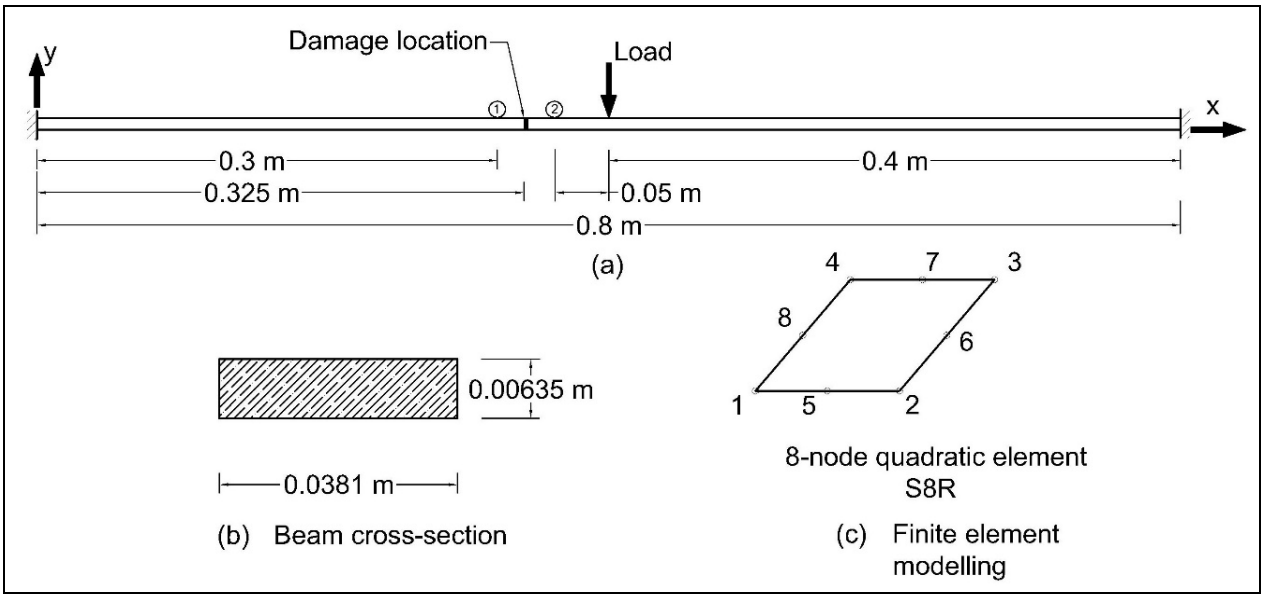

Figure 3-5 (a) Schematic representation of a fixed-ended beam showing the damage location and the location of the applied load, (b) dimension of the cross-sectional area of the beam, and (c) finite element beam model used in the analysis.

Figure 3-6 shows the 3D representation of the deformed shape of the finite element model with the deformation scale factor of 15000 at time frame of 0.0048 sec. Figures 3-7a and 3-7b show the time domain signal responses at sensor pair 1-2 of the acceleration and angular velocity, respectively. Sensor 1 is located at a distance of 0.3 m from the left support, while sensor 2 is located at a distance of 0.35 from the left support, as shown in Figure 3-5a.

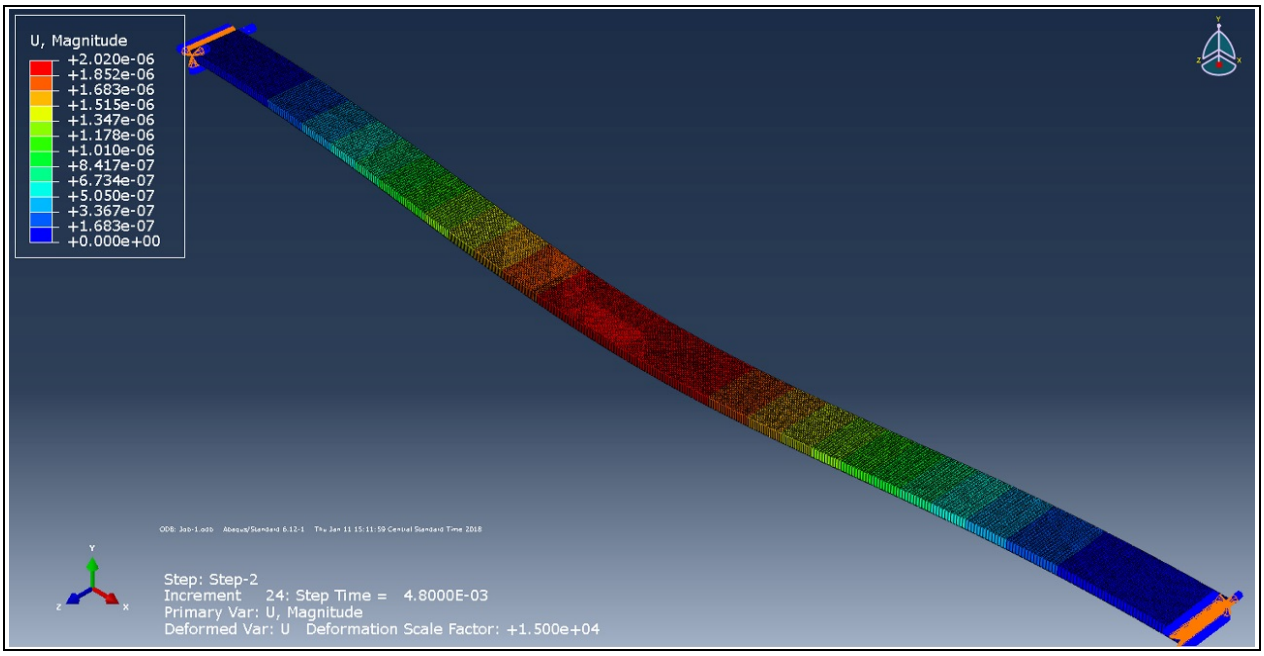

Figure 3-6 3D representation of the deformed shape of the finite element model.

In both the healthy and damaged scenarios, the linear acceleration and angular velocity responses in the time domain were measured at sensors 1 and 2 (Figures 3-7a and 3-7b) in the vicinity of the damage area. Figure 3-8a shows the resulting coherence functions of the linear acceleration and the angular velocity of Figures 3-7a and 3-7b. Figure 3-8b shows the transmissibility function of sensor pair 1-2 for the healthy and damage scenarios using the linear acceleration, while Figure 3-8c shows the latter information when the angular velocity is used. A frequency band between 250-420 Hz was selected for both linear acceleration and angular velocity since the coherence function showed a high level of linearity and was close to 1 at these frequencies, as shown in Figure 3-8a. The transmissibility of the healthy beam was considered as the baseline in the damage index.

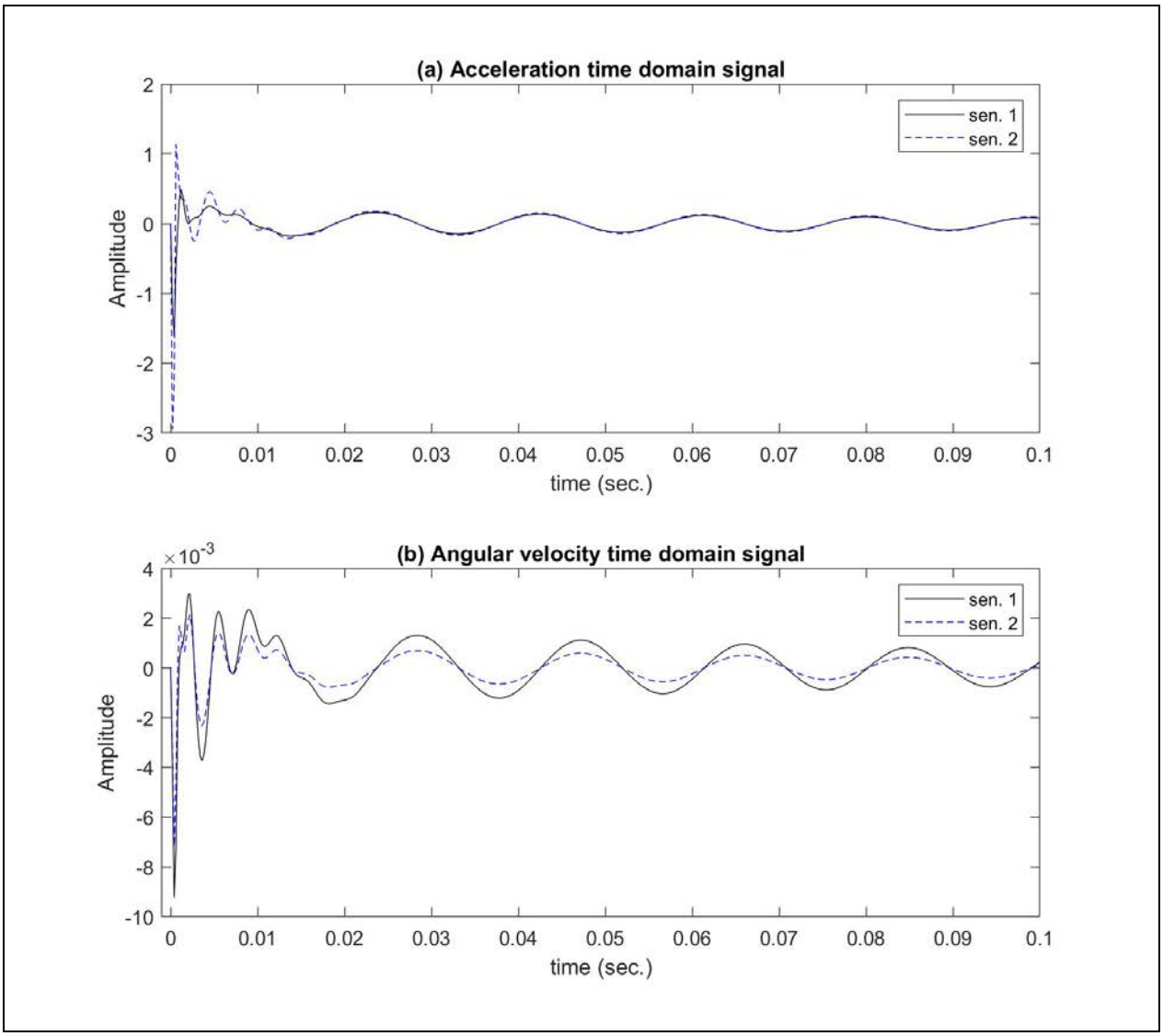

Figure 3-7 (a) The acceleration response in the time domain of sensors 1 and 2, (b) the angular velocity response in the time domain of sensors 1 and 2.

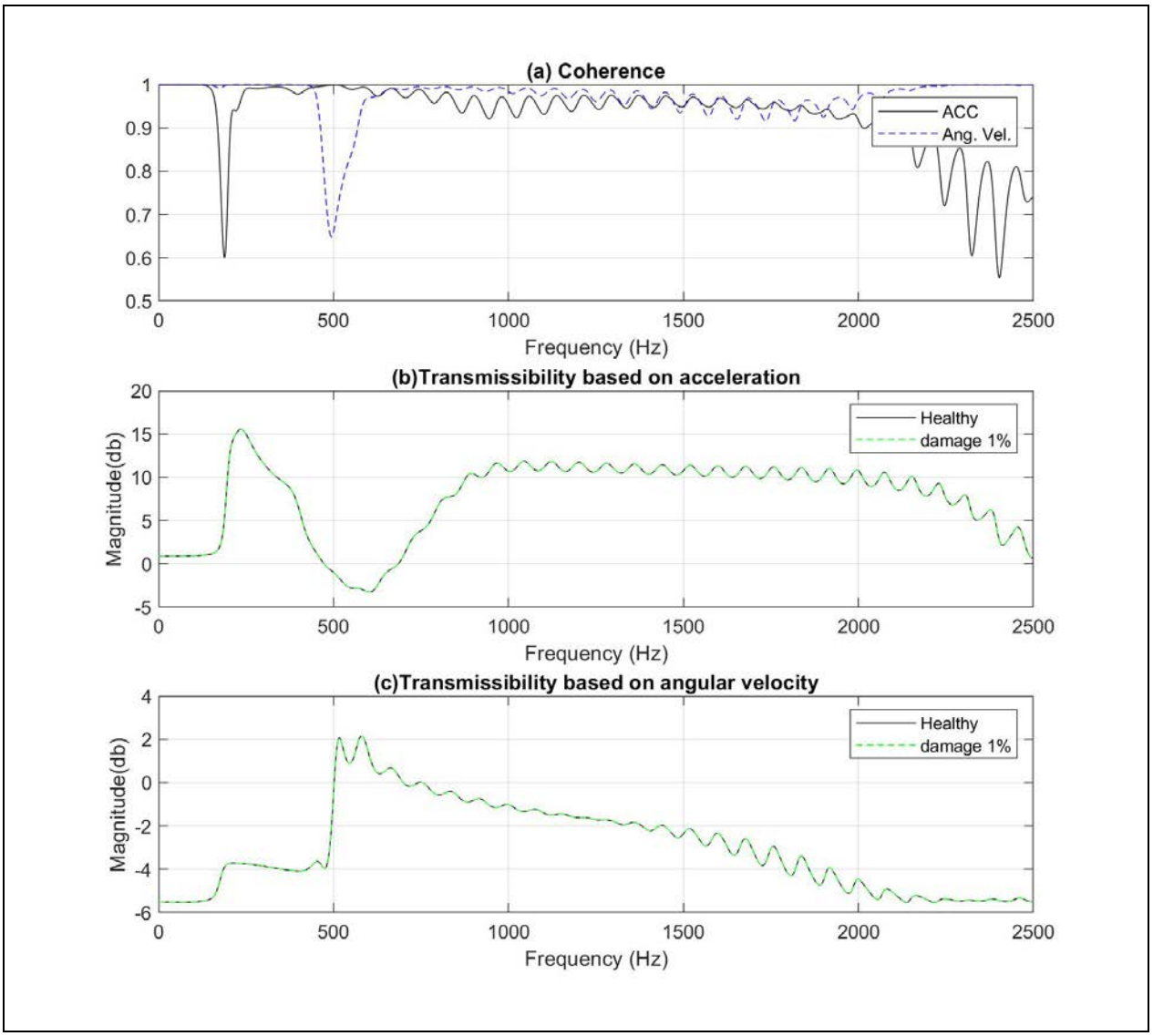

Figure 3-8 (a) The coherence of the acceleration and the angular velocity signal of sensors pair 1-2, (b) the transmissibility of the acceleration of sensors pair 1-2, and (c) the transmissibility of the angular velocity of sensors pair 1-2.

The calculated damage index for the 1%, 0.5%, 0.1%, 0.05%, 0.01%, and 0.005% reduction of stiffness damage scenarios for sensor pair 1-2 using transmissibility based on the acceleration and that based on angular-velocity are shown in Figure 3-9. As shown in the figure, the damage indices for both the acceleration and the angular velocity were very effective in locating the damage on the beam at pair 1-2. However, the magnitude of the damage index using the angular velocity was many times higher than that using the acceleration, thus it is more sensitive to the damage. In addition, Figure 3-9 shows that the damage index of the angular velocity could indicate the damage of 0.01% reduction of stiffness of 0.781 mm element. In contrast, the damage index of the acceleration could detect the damage up to 0.05% reduction of stiffness of a 0.781 mm element, which is five times lower when using transmissibility based on the angular velocity damage detection.

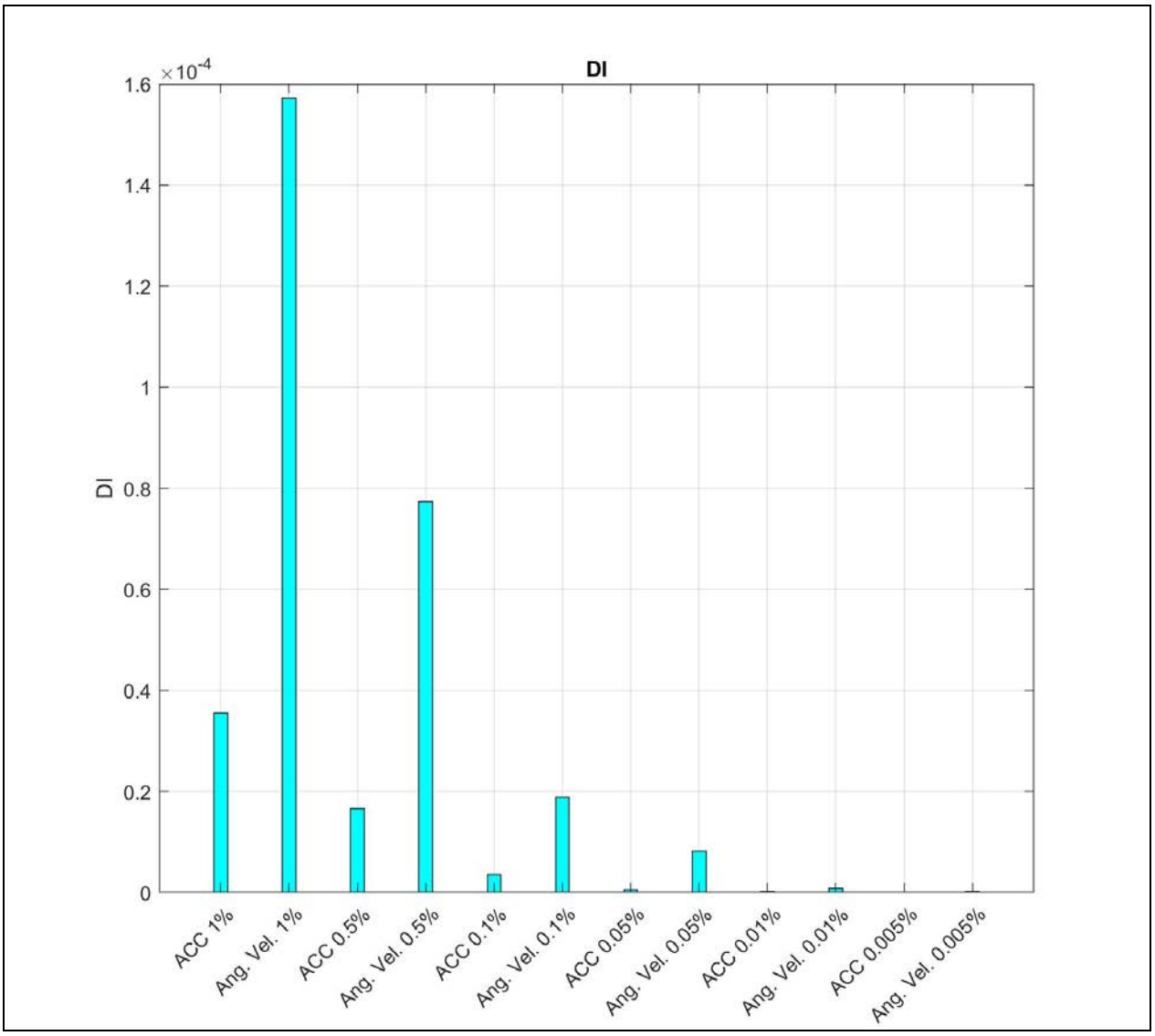

Figure 3-9 Damage index of transmissibility based on linear acceleration in the Y-direction and that based on angular velocity calculated for the 1%, 0.5%, 0.1%, 0.05%, 0.01%, and 0.005% reduction of stiffness between sensor pair 1-2 (damage location).

3.3.3. Cantilever Beam

A cantilever beam 0.79 m in length and a rectangular cross-section 0.076 m wide and 0.006 m deep was used in the analysis (Figure 3-10). The beam was made from steel with a density of 7860 kg/m3 and a Young's Modulus of 200 GPa and was considered healthy or undamaged. The beam was loaded with an impulse point loading of 1 N/s at the end as shown in Figure 3-10.

A damage 0.002 m in length was introduced into the beam in its longitudinal direction by reducing the depth of the beam. Figure 3-10 shows the damage location on the beam. Three levels of damage severity are considered in this example as reductions in the depth of beam at the damage location: 16.6%, 33%, and 50% reductions in the depth of beam at the damage location.

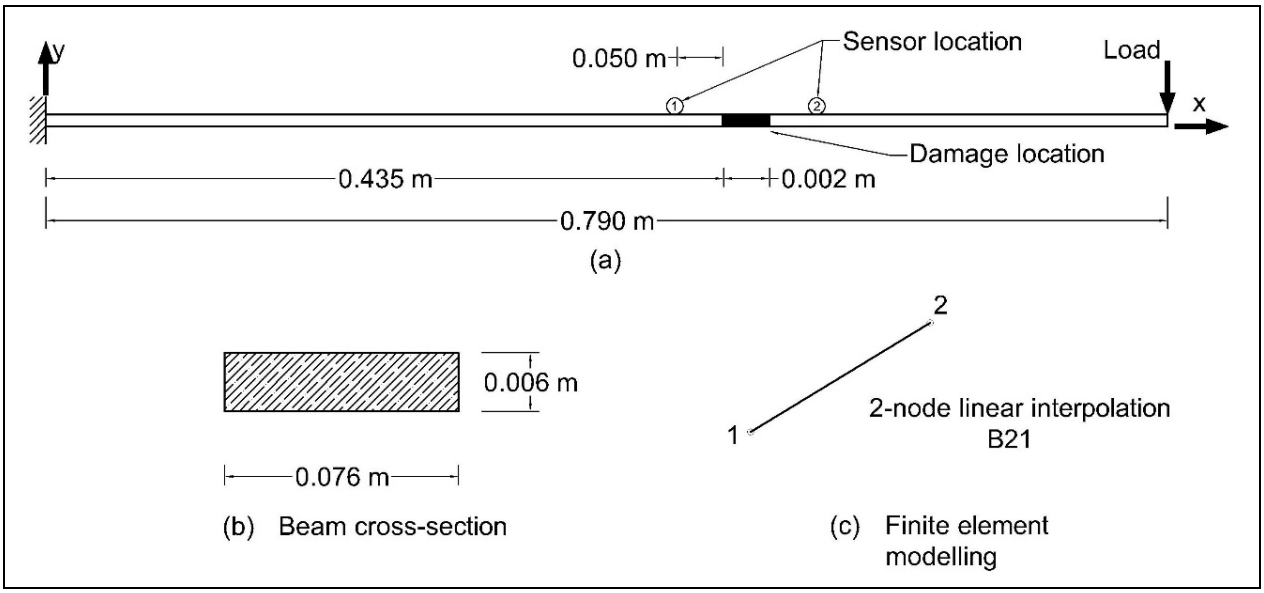

Figure 3-10 (a) Schematic representation of the cantilever beam, (b) dimension of the cross-sectional area of the beam, and (c) finite element beam model used in the analysis.

In both the healthy and damaged scenarios, the angular velocity and the acceleration responses in the time-history were measured at the pair of sensors (1-2) shown in Figures 3-11a and 3-11b. The time domain signals were taken to the frequency domain using a Blackman window (with 128 sampling points) [40] inside MATLAB (R2016a). The coherence (Figures 3-11c and 3-11d) and transmissibility (Figures 3-12a and 3-12b) between the two sensors were calculated for both angular velocity and acceleration at the same frequency band of 5-10 Hz where high coherence existed. For the damage index calculation, the transmissibility of the healthy beam was considered as the baseline of that of the three damage cases.

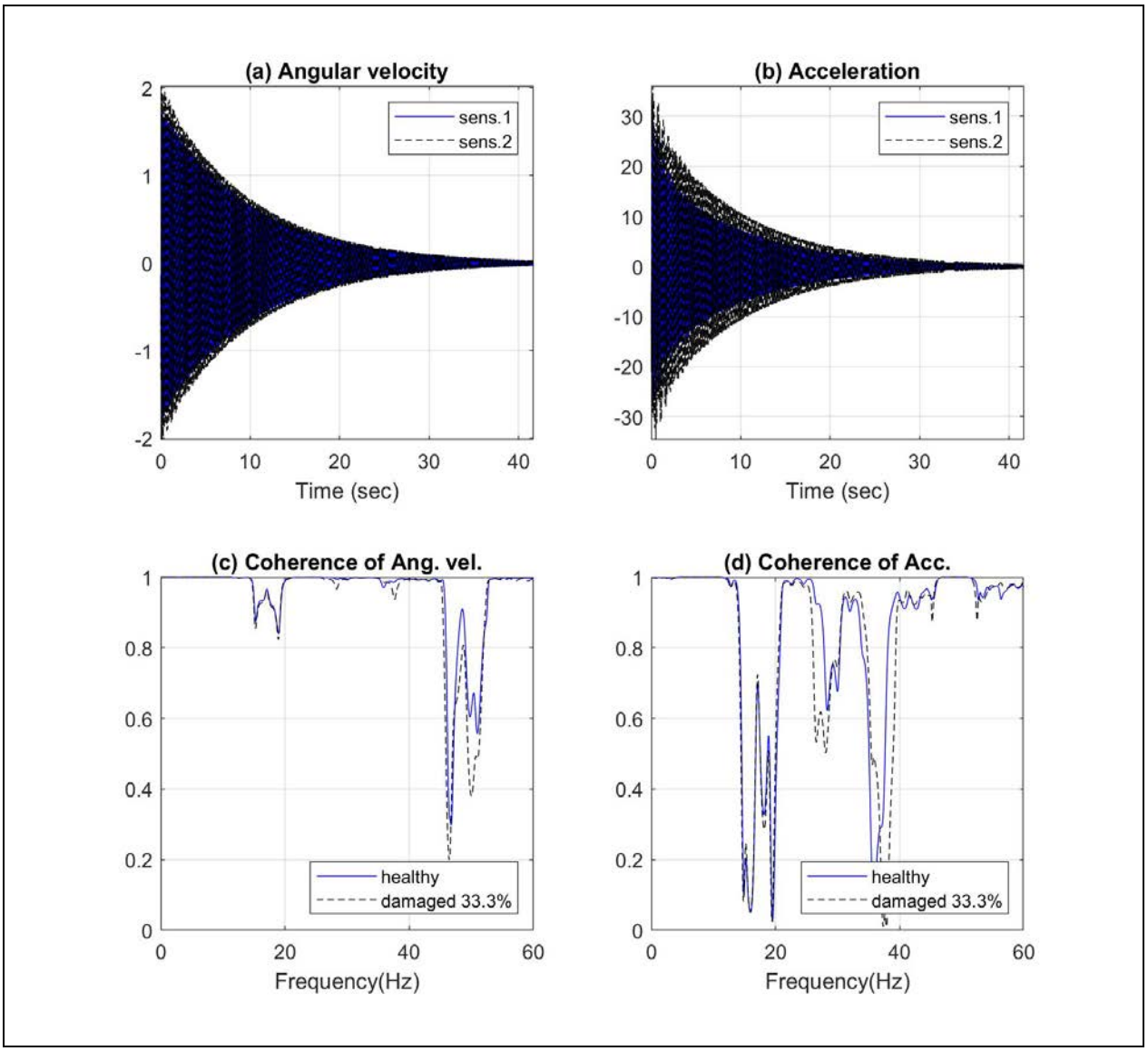

Figure 3-11 (a) Angular velocity in the time domain of the healthy beam at sensors 1 and 2, (b) acceleration in time domain of the healthy beam at sensors 1 and 2, (c) the coherence of the angular velocity signal of the healthy and damage case (33.3%), and (d) the coherence of the acceleration signal of the healthy and damage case (33.3%).

The transmissibility calculations have been repeated for the three damage scenarios under the same loading condition. Figures 3-12c and 3-12d show the corresponding damage indices for the three damage cases under investigation. It can be seen from Figures 3-12c and 3-12d that the damage indices for both the angular velocity and acceleration were able to capture and quantify the damage. However, the damage index of the angular velocity was consistently much higher than that of the acceleration for the three damage cases.

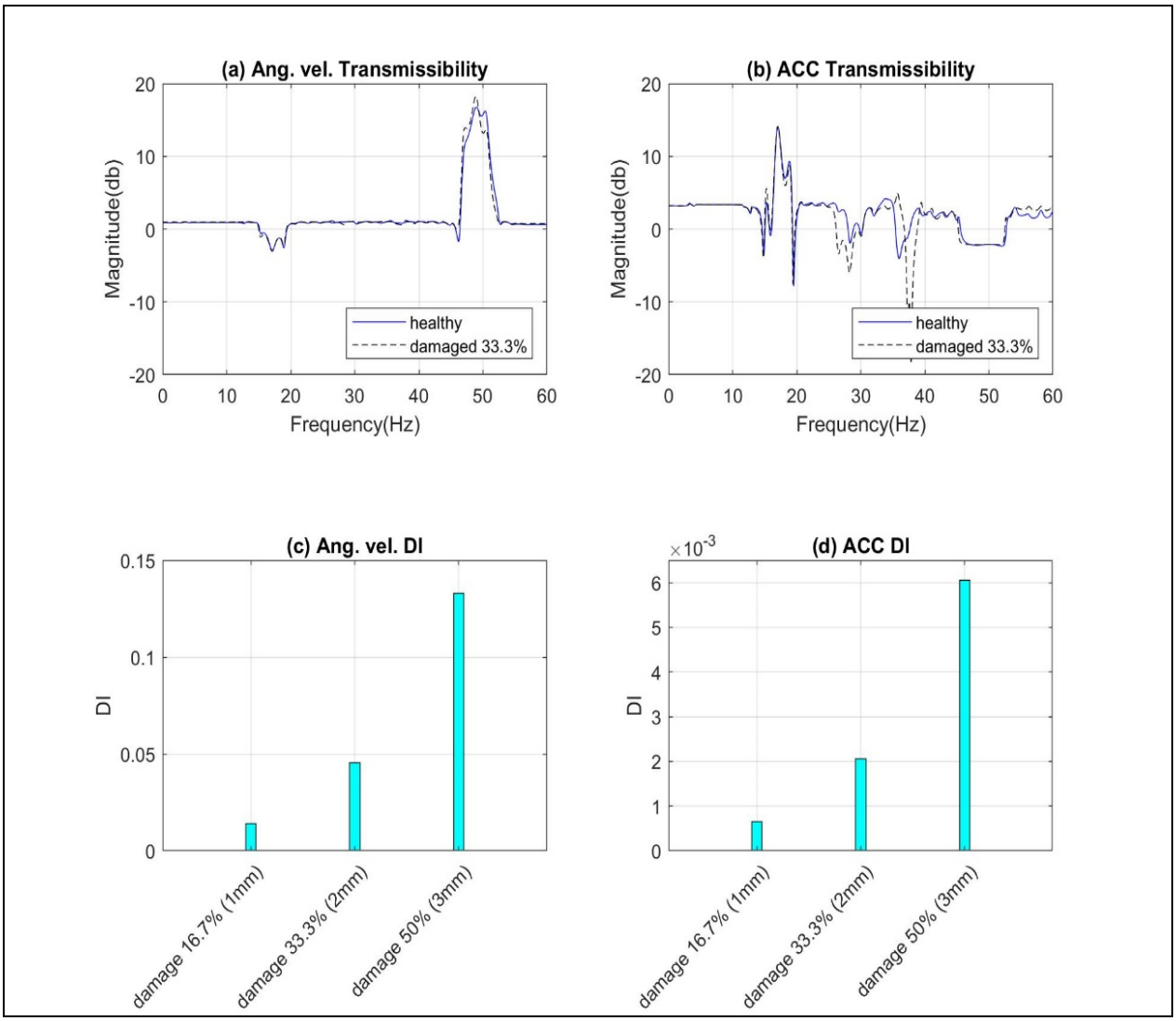

Figure 3-12 (a) Transmissibility based on the angular velocity, (b) transmissibility based on the acceleration, (c) damage index based on the transmissibility of the angular velocity, and (d) damage index based on the transmissibility of the acceleration.

The effect of including noise in the angular velocity and acceleration signals on the resulting damage index using a beam with 50% damage was investigated. Five percent white noise was added to the time domain of the response of angular velocity and acceleration, and the damage index of the angular velocity was 22.12 times higher than the damage index extracted from the acceleration measurement. In addition, the effect of 5% white noise on the damage

index based on angular velocity was only 4.22% of its original value, while the damage index based on acceleration was affected by 41.67%.

3.4. Experimental Testing

An experimental study was conducted to compare the effectiveness of the damage index based on the transmissibility of the angular velocity and that of the transmissibility of acceleration in detecting and quantifying damage on a structure. Acceleration and angular velocity data were collected at different points on the structure using accelerometers and gyroscopes. Four inertial sensors (manufactured by Xsens Technologies) [41] with a sampling rate of 120 Hz were used in the testing. Each inertial sensor unit (MTx-49A83G25) comprises 3D rate gyroscopes measuring angular velocities (in the range ±1200 ^{o}/s) and 3D linear accelerometers measuring accelerations (in the range ±5g) including gravitational acceleration. The weight of each inertial sensor is 24 g.

3.4.1. Experimental Setup

A rectangular cross-section cantilever steel beam with dimensions of 790 x 76 x 6 mm was selected to test the effectiveness of the proposed damage-detection method. The beam was fixed to an isolated frame as shown in Figure 3-13b. Four inertial sensors were placed at distances of 0.585 m (sensor 1), 0.485 m (sensor 2), 0.385 m (sensor 3), and 0.285 m (sensor 4) from the fixed end of the beam to measure the angular velocity and acceleration at the same time, as shown in Figure 3-13a. An impact load was applied at a distance of 25 mm from the free end of the cantilever. Twenty-five measurements were collected for each experiment, and the mean of the 25 coherence and transmissibility functions of the angular velocities and the accelerations was calculated in the frequency domain and then used to calculate the damage index. All calculations were handled in MATLAB (R2016A).

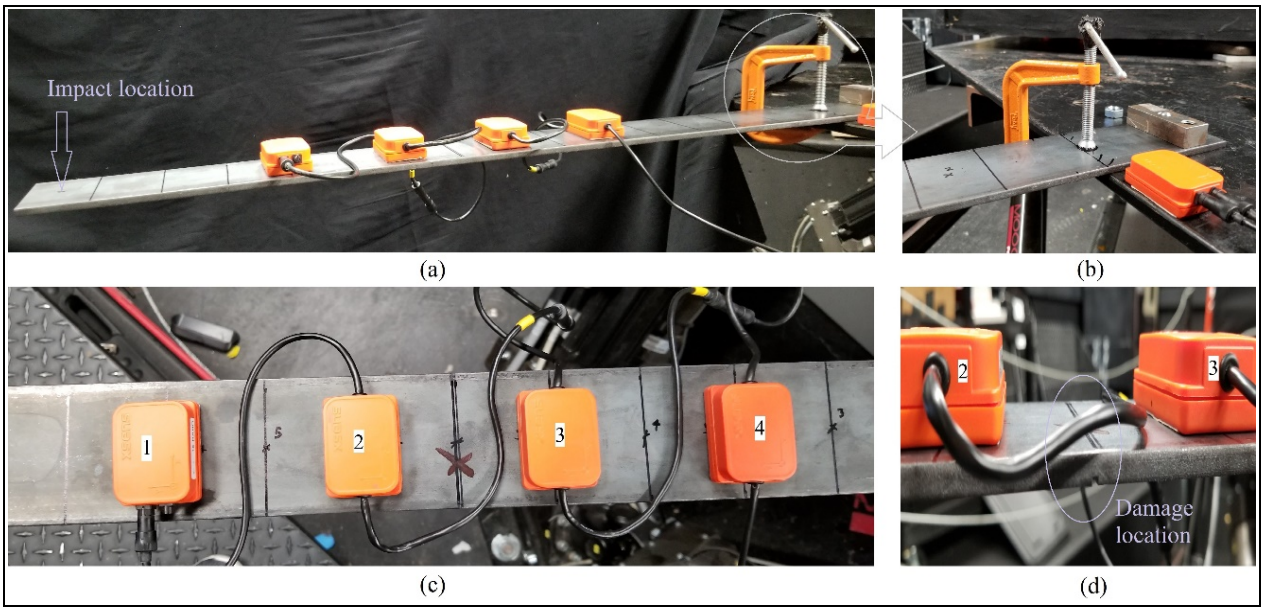

Figure 3-13 (a) The experiment setup of the cantilever beam and the location of the sensors, (b) the fixed end of the beam, (c) the location of the sensors, (d) the location of the damage (2 mm * 2 mm slot along the width of the beam) between sensor 2 and sensor 3.

Two scenarios of the experiment were conducted on the cantilever beam: healthy and damaged. In the first scenario, a healthy cantilever beam was used, and the angular velocities and acceleration were collected at each sensor under each of the 25 impacts. In the second scenario, the cantilever beam was damaged at a distance of 0.435 m from the fixed end by introducing a slot (2 mm * 2 mm) across the width of the beam between sensors 2 and 3, as shown in Figure 3-13d. The angular velocities and accelerations were then measured under 25 impact-loading conditions.

3.4.2. Experimental Result

After acquiring the data in the time domain for both angular velocity and acceleration, as shown in Figures 3-14a and 3-14b, the coherence (Figures 3-14c, 3-14d) and transmissibility (Figures 3-15a, 3-15b) were then calculated for each impact load for the healthy and damage scenarios. All frequency analyses were carried out in the frequency domain using the Blackman window applied to the time domain responses (with 64 sampling points) [40] inside MATLAB

(R2016a). The mean of the 25 coherences and transmissibilities of the angular velocities and accelerations was extracted and used to calculate the damage index for each scenario, as shown in Figures 3-15c and 3-15d.

The magnitude of the transmissibility between sensors 2 and 3 was calculated for the two scenarios and for both acceleration and angular velocity at the same frequency band (high coherence 5-10 Hz). Figures 3-15c and 3-15d showed that both the angular-velocity-based and the acceleration-based transmissibility successfully detected the damage at the damage location. The magnitude of the angular velocity damage index, though, is larger than the magnitude of the damage index based on the acceleration, indicating that the angular velocity is more sensitive to the same amount of damage.

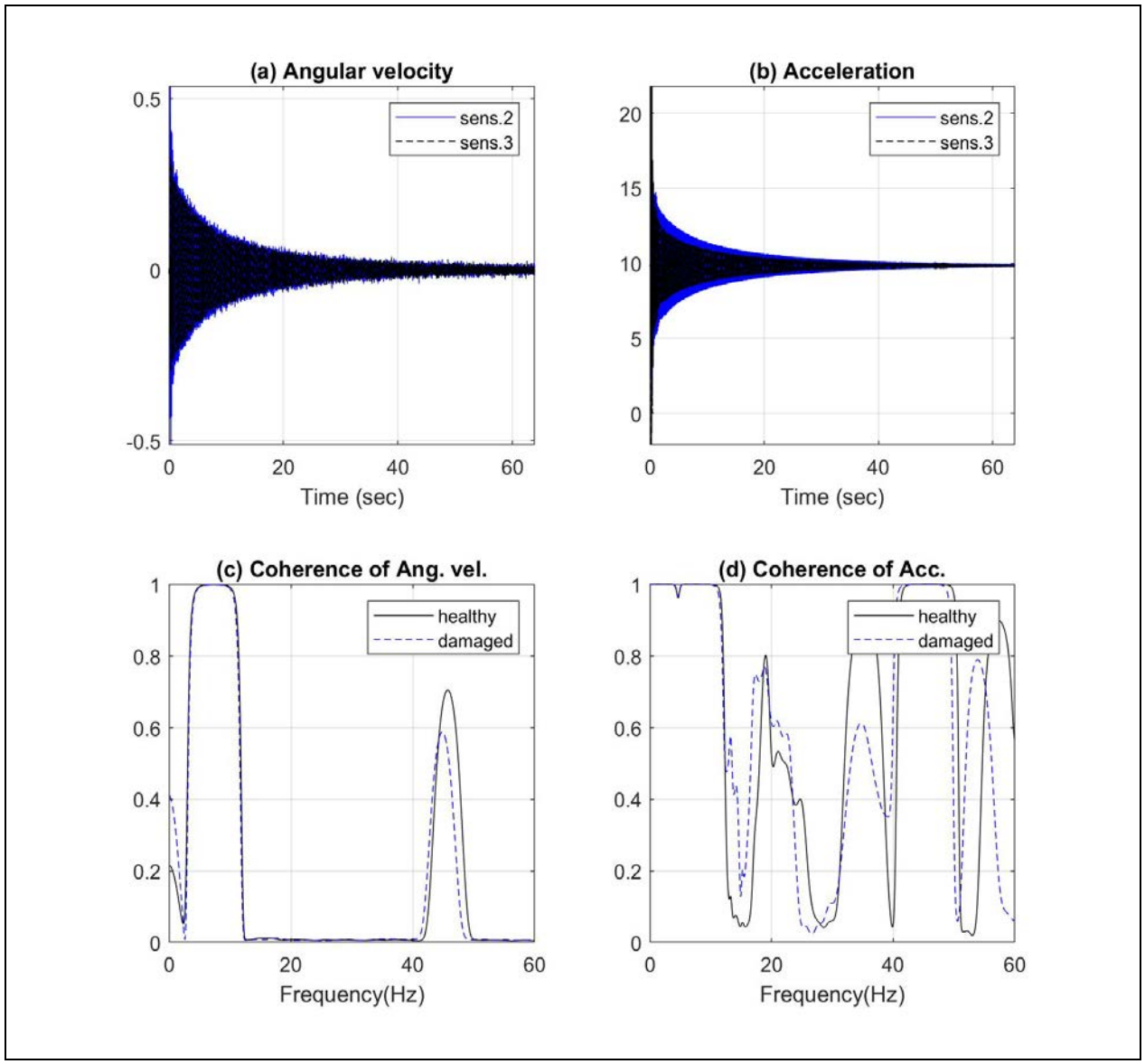

Figure 3-14 (a) Angular velocity in time domain of the healthy scenario at sensors 2 and 3, (b) acceleration in time domain of the healthy scenario at sensors 2 and 3, (c) the coherence of angular velocity signal for the healthy and damage beams, and (d) the coherence of acceleration signal for the healthy and damage beams.

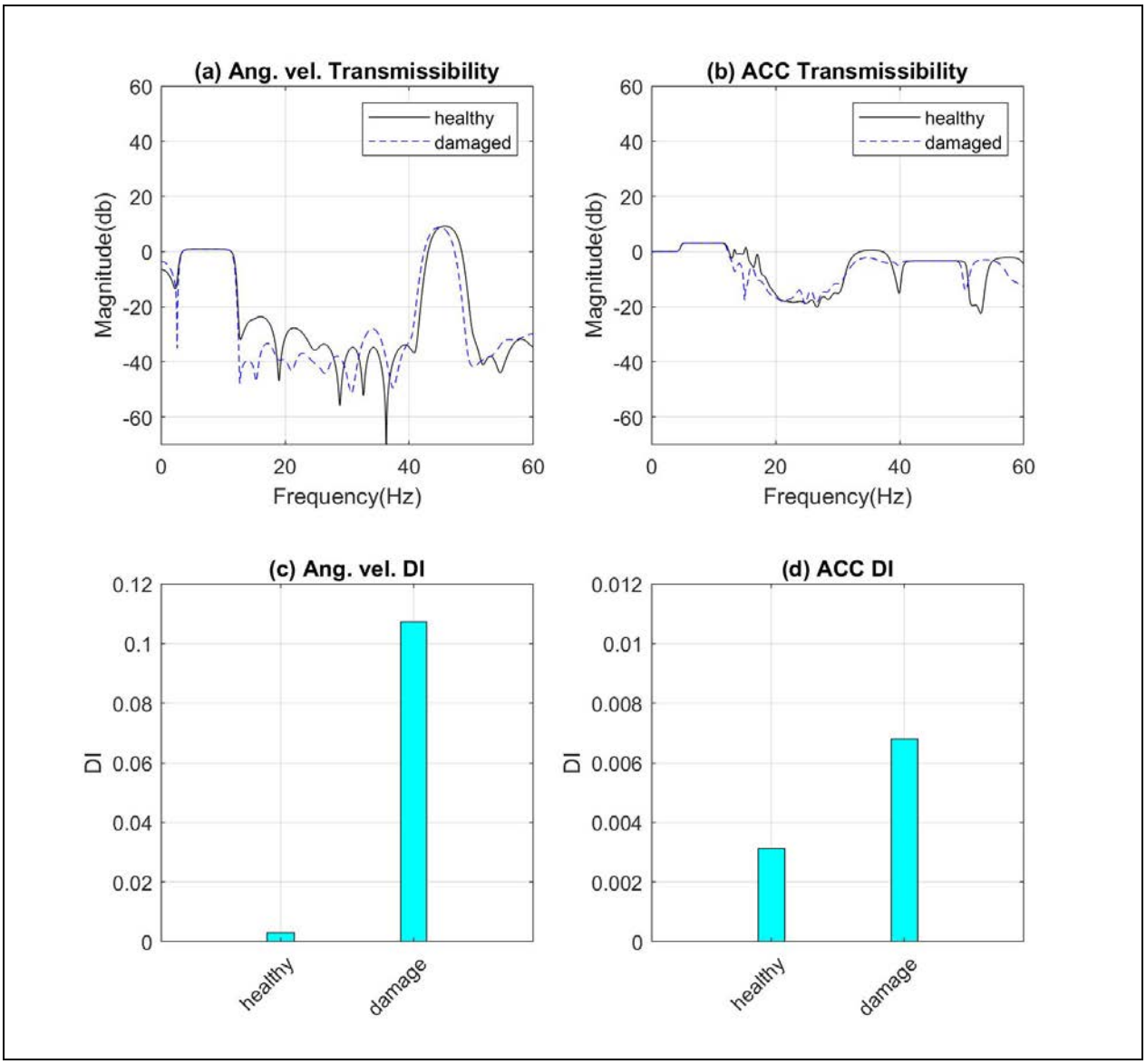

Figure 3-15 (a) The transmissibility based on the angular velocity, (b) the transmissibility based on acceleration, (c) damage index based on the transmissibility of angular velocity, and (d) the damage index based on the transmissibility of acceleration.

3.5. Conclusion

A new damage-detection methodology is presented in this work. It uses a damage index based on the changes in the transmissibility of the angular velocity between healthy and damaged beams. The transmissibility and coherence of the angular velocity between two points on the structure under vibration were used to construct a damage index. The proposed method demonstrated an excellent capability in detecting damage on straight beams. The method showed superiority when compared with the traditional transmissibility based on the linear-acceleration damage index for the tested beams. The damage index showed higher magnitudes when using the angular velocity compared to linear acceleration. A ratio between the angular velocity damage index and the linear acceleration damage index reached 15.8 for the damaged scenario without noise for the experiment result.

CHAPTER FOUR: ACOUSTIC NOISE EFFECT ON TRANSMISSIBILITY-BASED DAMAGE DETECTION

4.1. Experimental Testing

The effect of the acoustic noises in the surrounding environment was investigated when the experimental study in the previous chapter was conducted. The transmissibility based on angular velocity and acceleration damage-detection approaches were compared in detecting and quantifying damage on the cantilever beam with the presence of different levels of acoustic noises in the surrounding environment. As stated in Chapter Three, angular velocity and acceleration data were collected at different points on the structure using gyroscopes and accelerometers. Four inertial sensors (manufactured by Xsens Technologies) [41] with a sampling rate of 120 Hz were used in the testing. Each inertial sensor unit (MTx-49A83G25) comprises 3D rate gyroscopes measuring angular velocities (in the range ±1200 ^{o}/s) and 3D linear accelerometers measuring accelerations (in the range ±5 g) including gravitational acceleration.

4.1.1. Experimental Setup

A rectangular cross-section cantilever steel beam with dimensions of 790 x 76 x 6 mm was selected. The beam was fixed to an isolated frame as shown in Figure 4-1a. Four inertial sensors were placed at distances of 0.585 m (sensor 1), 0.485 m (sensor 2), 0.385 m (sensor 3), and 0.285 m (sensor 4) from the fixed end of the beam to measure the angular velocity and acceleration at the same time, as shown in Figures 4-1a and 4-1c. An impact load was applied at a distance of 25 mm from the free end of the cantilever (Figure 4-1c). Twenty-five measurements were collected for each experiment, and the mean of the 25 coherence and transmissibility functions of the angular velocities and the accelerations was calculated in the frequency domain

and then used to calculate the damage index. All calculations were handled in MATLAB (R2016a).

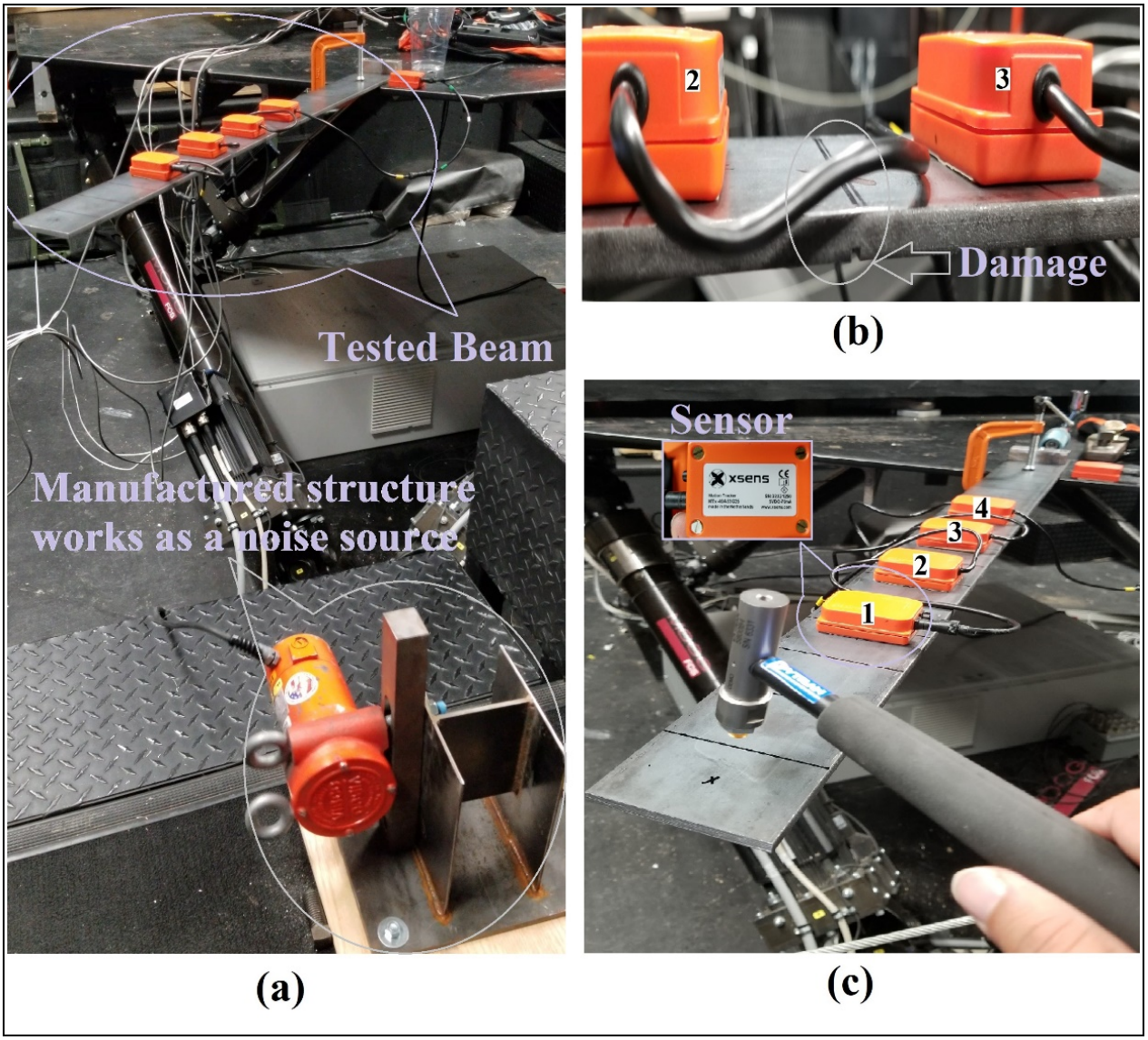

Figure 4-1 The experiment setup of the cantilever beam, (a) cantilever beam clamped from one end to a ground-isolated platform, and a variable-speed motor as the source of acoustic noise attached to a manufactured plate approximately 1 meter away from the cantilever, (b) a close look at the location of the damage area and the sensors surrounding it, and (c) a close look at the location of the impact load on the beam.

The beam was tested under healthy condition with and without acoustic noise and under damage condition with and without acoustic noise. The acoustic noise was generated by a variable-speed-vibrator DC motor attached to a manufactured plate structure that was approximately 1 meter from the cantilever beam, as shown in Figure 4-1a. The manufactured plate was isolated from the cantilever beam, such that the vibration generated from the DC motor would not affect the cantilever beam, i.e., the cantilever beam would only be affected by the acoustic noise of the DC motor and would not be affected by its vibration.

In the healthy beam scenario, the angular velocities and acceleration were collected at each sensor under each of the 25 impacts without acoustic noise and with acoustic ambient noise of different intensities at an average of 78 dB and 85 dB. In the damage scenario, the cantilever beam was damaged at a distance of 435 mm from the fixed end by introducing a slot (2 mm * 2 mm) across the width of the beam between sensors 2 and 3, as shown in Figure 4-1b. Again, the beam was tested without acoustic noise and with acoustic noise with different intensities at an average of 65 dB and 75 dB. Figure 4-2a shows the time domain of the noise signal in the testing room without and with the presence of the acoustic noise generated from the variable-speed-vibrator DC motor. Figure 4-2b shows the power spectrum of the noise signals in Figure 4-2a.

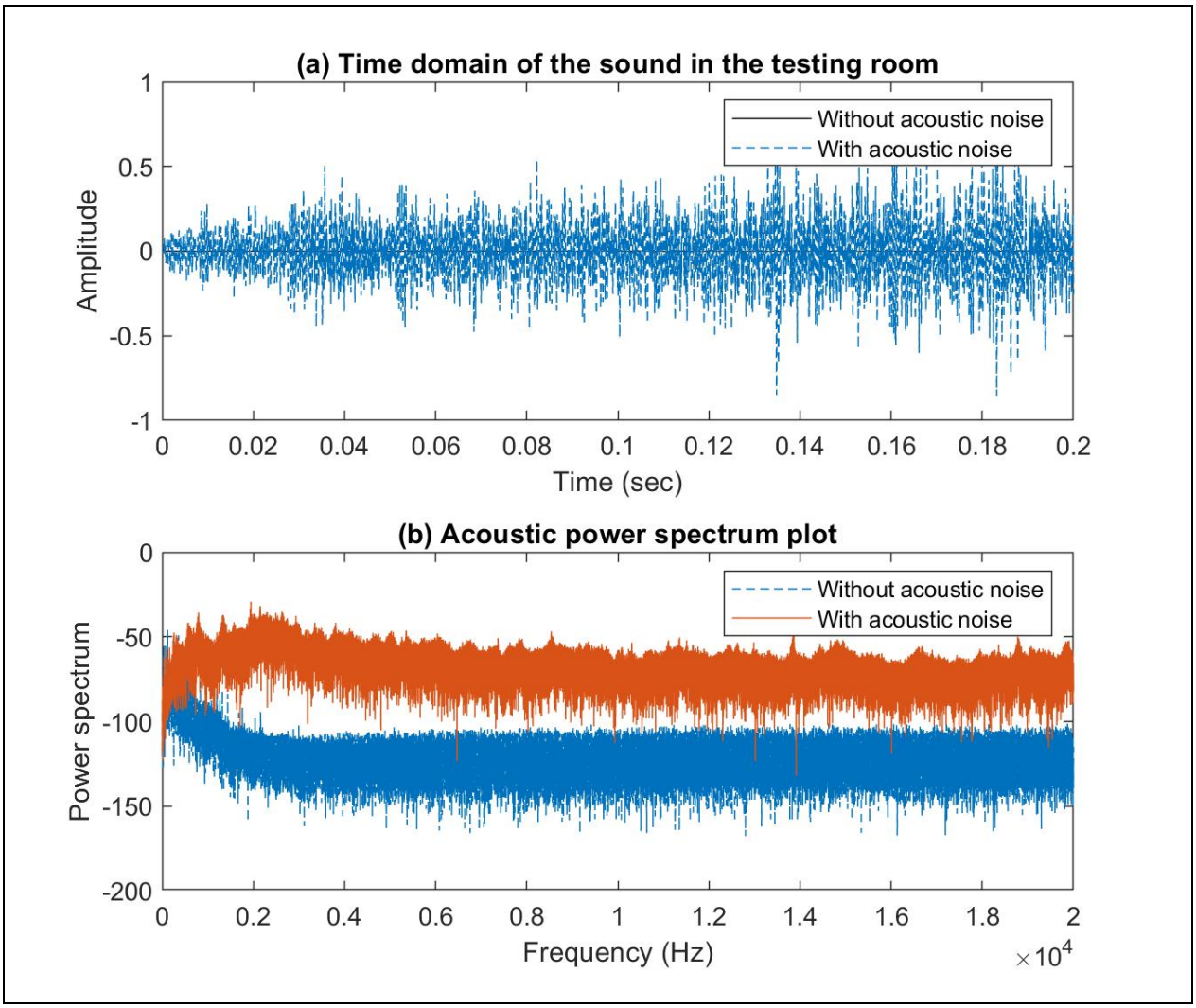

Figure 4-2 (a) Time domain of the noise signal in the testing room without noise and with acoustic noise generated from the operation of the variable-speed-vibrator DC motor, and (b) power spectrum plot of the noise in the room without noise and with acoustic noise generated from the operation of the variable-speed-vibrator DC motor.

4.1.2. Experimental Result

After acquiring the data in the time domain for both angular velocity and acceleration, as shown in Figures 4-3a and 4-3b, the coherence (Figures 4-3c, 4-3d) and transmissibility (Figures 4-4a, 4-4b) were then calculated for each impact load for all scenarios: healthy without noise, healthy with noise, damage without noise, and damage with noise. All frequency analyses were carried out in the frequency domain using the Blackman window applied to the time domain responses (with 64 sampling points) [40] inside MATLAB (R2016a). The mean of the 25 coherences and transmissibilities of the angular velocities and accelerations was extracted and used to calculate the damage index for each scenario, as shown in Figures 4-4c and 4-4d.

Figures 4-4c and 4-4d showed that the damage index (at high coherence between 5-10 Hz) of both the transmissibility based on the angular velocity and the transmissibility based on the acceleration successfully detected the damage at the damage location for the scenario with no ambient noise. The magnitude of the damage index based on the transmissibility of the angular velocity, however, was larger than that based on the transmissibility of the acceleration and was less affected by the acoustic noise, for the acoustic noises under consideration, as compared with the acceleration.

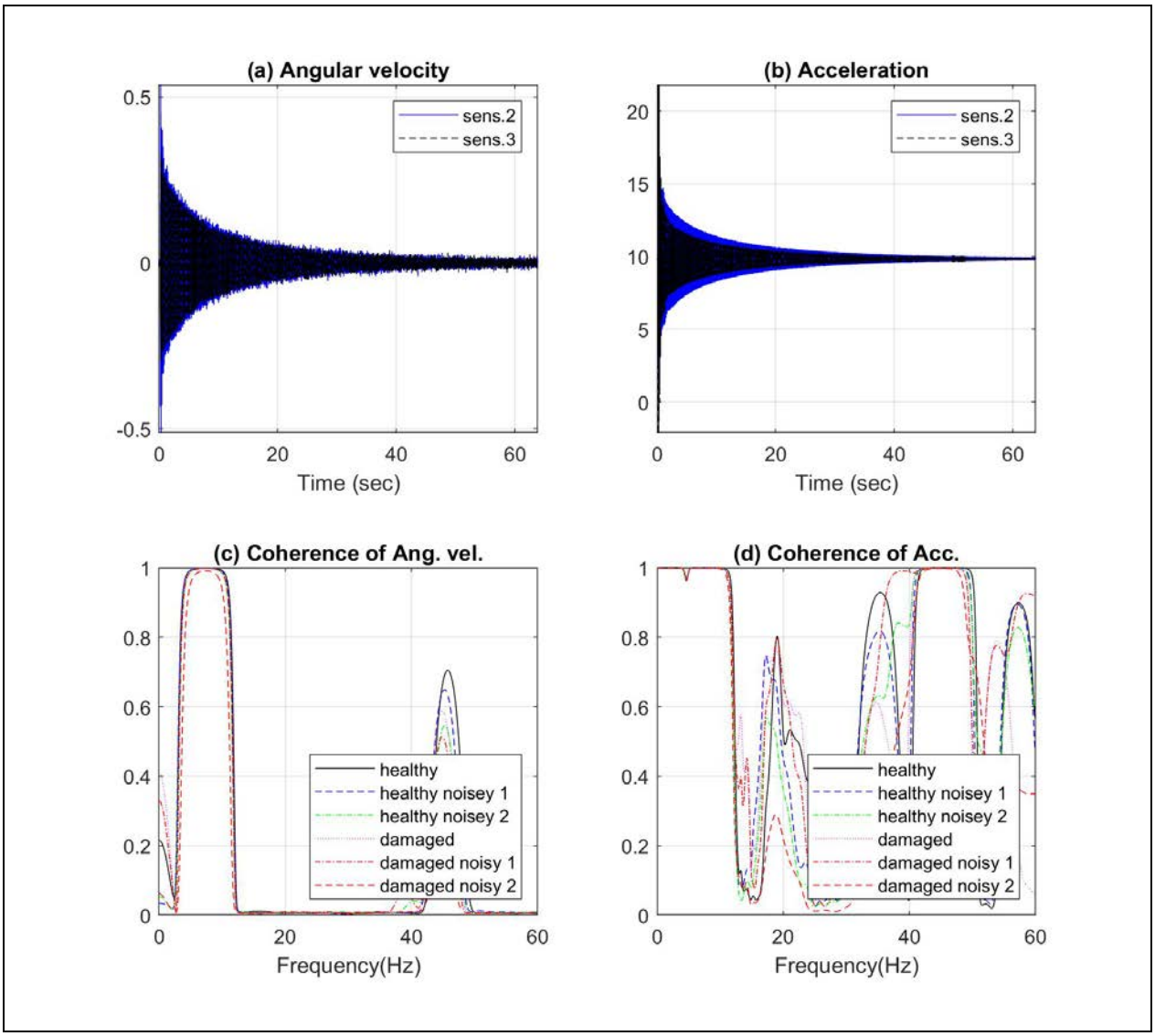

Figure 4-3 (a) Angular velocity in time domain of the healthy scenario at sensors 2 and 3, (b) acceleration in time domain of the healthy scenario at sensors 2 and 3, (c) the coherence of angular velocity signal for the healthy and damage beams without and with noise conditions, and (d) the coherence of acceleration signal for the healthy and damage beams without and with noise conditions. Healthy (noise 1):78 dB; healthy (noise 2): 85 dB; damage (noise 1): 65 dB; damage (noise 2): 75 dB.

The presence of acoustic noise showed a significant impact on the transmissibility of acceleration damage index, as shown in Figure 4-4d. As can be seen from the second, third, and fourth bars in Figure 4-4d, the transmissibility based on the acceleration damage index had a hard time distinguishing between an undamaged beam with acoustic noise and a damaged beam

without acoustic noise, generating a false detection. In contrast, the transmissibility based on the angular-velocity damage index was less affected by the presence of acoustic noise, as shown in Figure 4-4c. The damage index for the healthy beam without noise is very similar to that with noise.

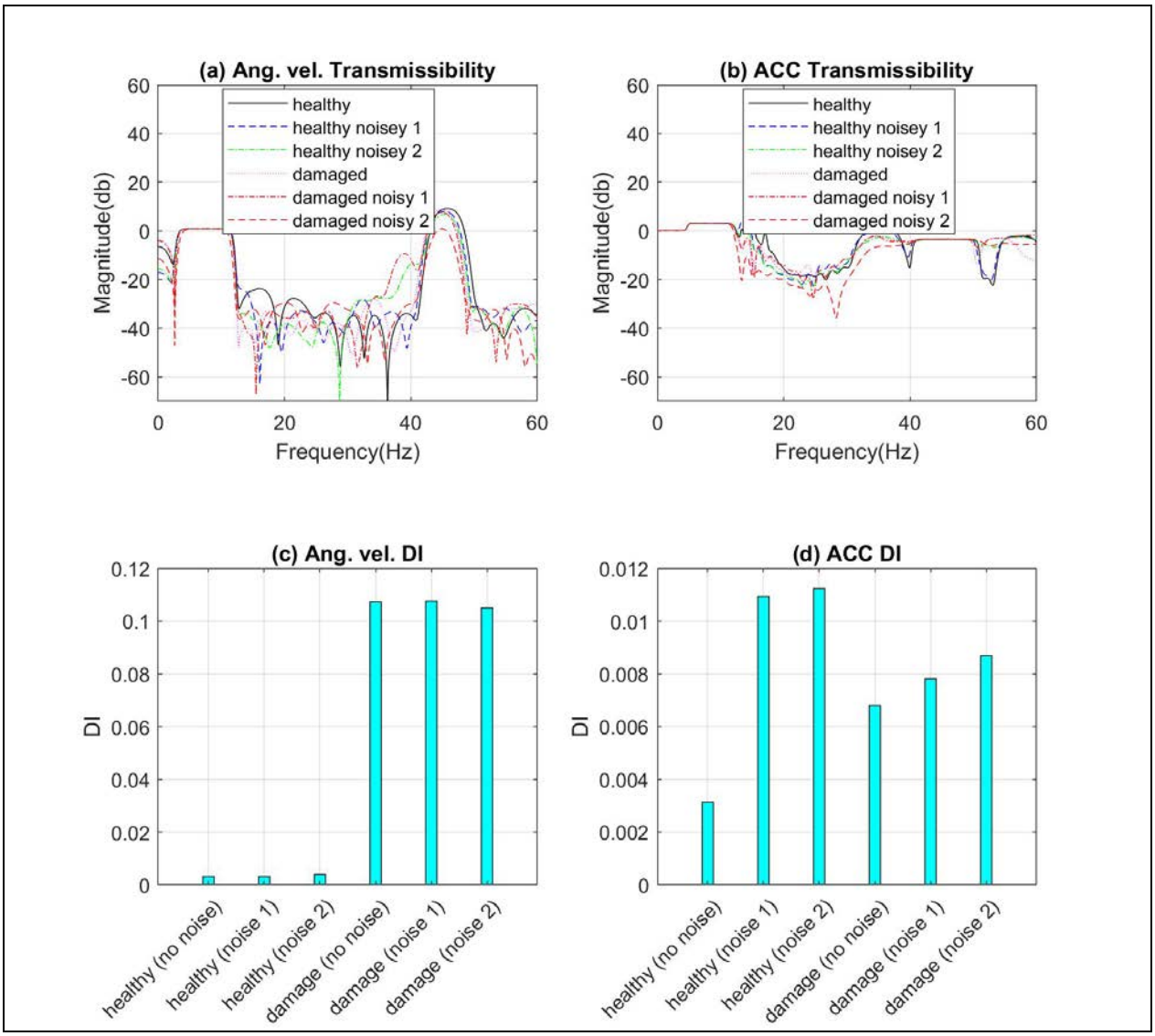

Figure 4-4 (a) Transmissibility based on the angular velocity, (b) transmissibility based on acceleration, (c) damage index based on the transmissibility of angular velocity, and (d) damage index based on the transmissibility of acceleration. Healthy (noise 1):78 dB; healthy (noise 2): 85 dB; damage (noise 1): 65 dB; damage (noise 2): 75 dB.

When the damage index using pairs 1-2, 2-3, and 3-4 (as shown in Figure 4-1a) was considered, the damage was successfully detected at the damage location (pair 2-3) using the angular velocity under no noise and under the two noise levels (Figures 4-5a, 4-5c, and 4-5e). On the other hand, the transmissibility based on acceleration damage index predicted damage between sensors 3-4 instead of 2-3 (Figures 4-5b, 4-5d, and 4-5f).

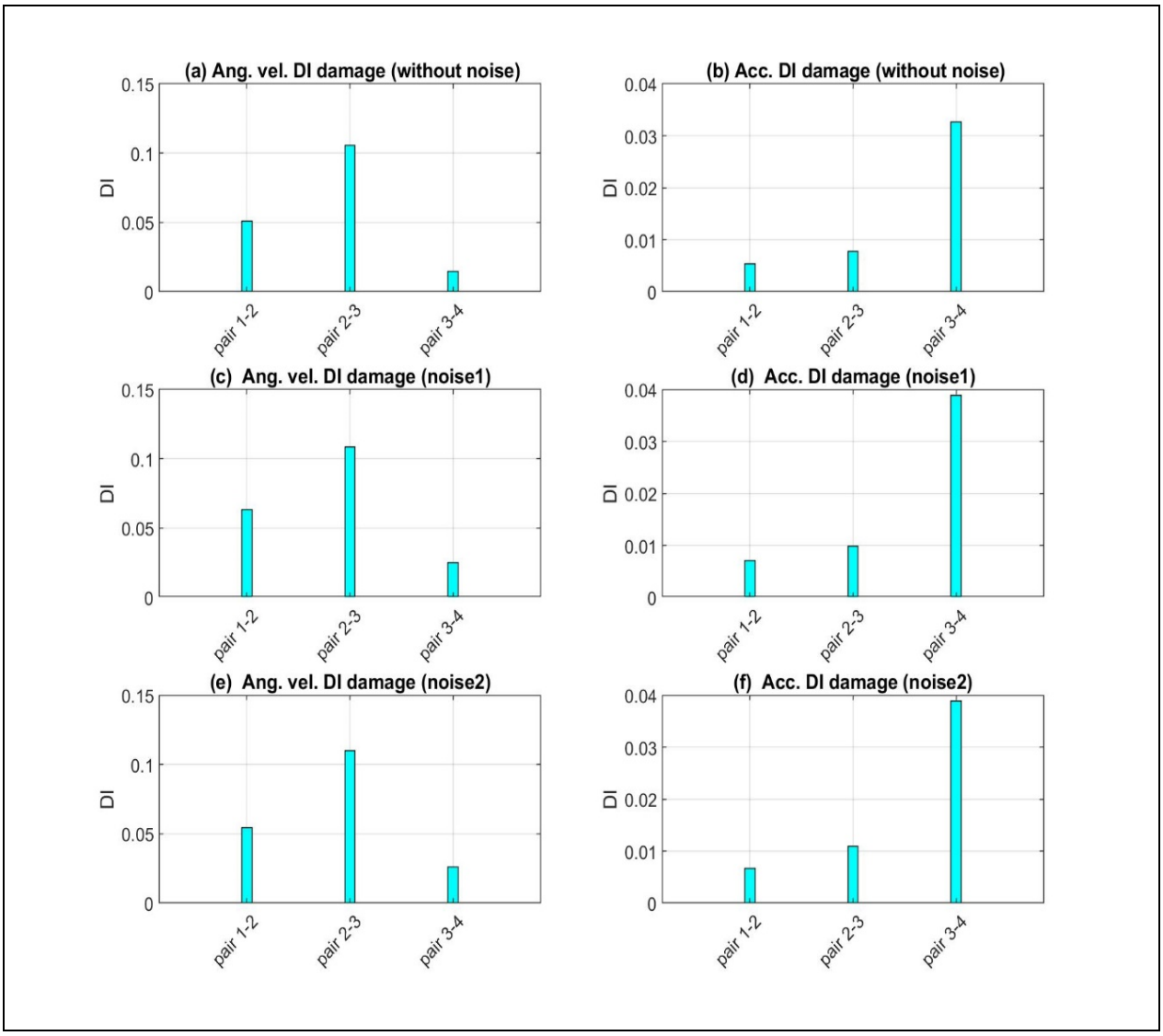

Figure 4-5 Damage index based on transmissibility of angular velocity and acceleration between pairs 1-2, 2-3, and 3-4, (a-b) without ambient noise, (c-d) with ambient noise (intensity of 65 dB), (e-f) with ambient noise (intensity of 75 dB).

During the lab experimentation, the beam existed with a very small impact load, but still the resulting signals of the gyroscopes and accelerometers had enough power to show the difference between the healthy and damage conditions. While the resulting deflection under such small forces can be small, it appears that the angular velocity signal, similar to acceleration, can sense these small changes in angular velocities resulting from the impact. These characteristics of the gyroscope show promise for performance in a real-life situation where the signal to noise ratio can be very small under small operational loads.

4.2. Conclusion

As illustrated in the experimental results, the surrounding acoustic noise could mask the damage index based on the linear acceleration by giving a false detection for the healthy scenario with ambient noise. In contrast, the transmissibility based on angular-velocity damage index was less affected by the presence of acoustic noise; the damage index was almost the same for the healthy scenario with and without ambient acoustic noise. The proposed damage index showed superiority when compared with the traditional damage index based on the transmissibility of acceleration. The experimental results showed that the surrounding acoustic noise under consideration (65-85 dB) has more effect on the damage index based on acceleration than that based on angular velocity. It should be noted that the results of this work were based on the use of accelerometers and gyroscopes embedded in the inertial sensors by Xsens [41], and the results may change when using different types of sensors or using acoustic noise with different intensities [31, 32]. Further investigation could be performed on more complicated structures such as buildings, bridges, mechanical systems, and aerospace applications, and it is believed that the proposed damage index based on the transmissibility of the angular velocity may open new venues for using gyroscopes as part of the damage-detection process.

CHAPTER FIVE: CURVED BEAM

5.1. Introduction

Curved beam components are widely used in structural and mechanical systems. Compared to straight beam components, fewer studies have been conducted to investigate the damage detection and health monitoring of curved structures such as domes, arches, and curved beams and girders. Yang et al. [42] investigated the effect of vertical and horizontal moving load on the dynamic response of a horizontally curved beam. The effect of the crack location and its length on the changes of the dynamic characteristics (natural frequency and mode shape) of a finite element clamped-clamped arch was studied by Krawczuk and Ostachowicz [43]. In another study, Viola et al. [44] investigated the free vibration of circular arches in healthy and damaged configurations using the analytical and differential quadrature methods. Karaagac et al. [45] investigated the effect of a single-edge crack and its location on the dynamic characteristics and stability of a circular curved beam. Zheng et al. [46] developed and implemented a real-time damage-detection approach to detect and locate the changes in stiffness of steel domes subjected to earthquake using the wavelet transform. Barr et al. [47] investigated the effect of changing the state of the boundary conditions on the dynamic response of a curved steel I-girder bridge in Salt Lake City, Utah.

In the present work, the transmissibility-based damage-detection method using the angular velocity is used compared with another method that uses accelerations and the magnitude of the acceleration. High coherence is adopted in the present study [23] to choose the frequency band of the transmissibility function for the damage index. Two types of curved beams (horizontally curved and vertically curved beams) with sensitivity analysis including

different chord-height-to-length ratios are investigated in the current chapter to investigate the efficacy of the proposed method.

5.2. Numerical Example

5.2.1. Numerical Example (Vertical Curved Beam)

A fixed-ended beam is used in this example to show the capability of the proposed transmissibility based on angular-velocity methodology in detecting damage. The chord length of the beam was 0.75 m, the chord height was 0.05 m, and it had a rectangular cross-section of 0.0381 m width and 0.00635 m depth. It was made from steel with a density of 7860 kg/m^3 and a Young's Modulus of 210 GPa and was considered healthy or undamaged. The beam was loaded with an impulse point loading of 5 N/s at the middle as shown in Figure 5-1.

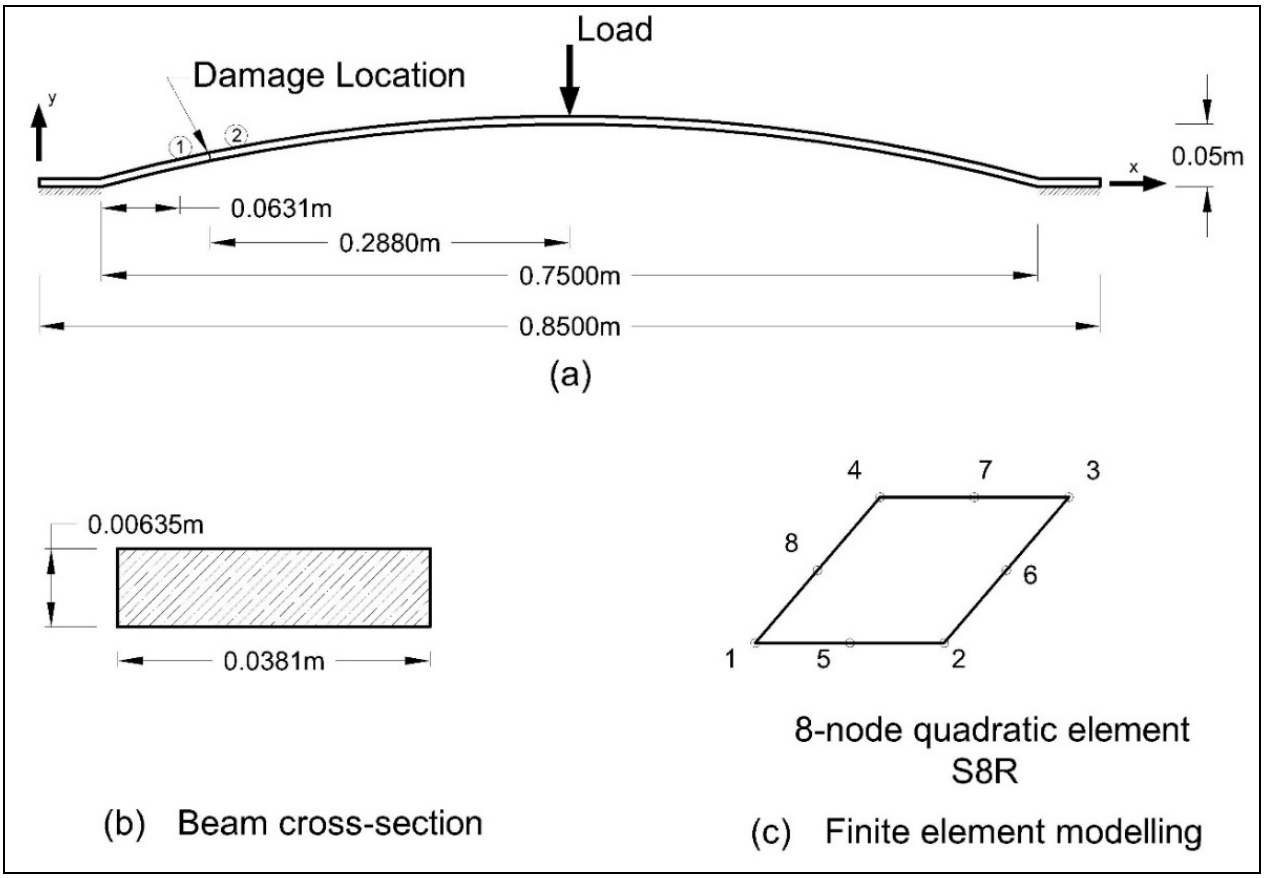

Figure 5-1 (a) Schematic representation of the fixed-ended beam with 0.05 m chord height, (b) dimension of the cross-sectional area of the beam, and (c) finite element beam model used in the analysis.

Figure 5-2 shows the deformable shape of the finite element beam. A damage of 0.001 m in length and 1% severity was introduced to the left side of the beam by reducing its stiffness, as shown in Figure 5-1a.

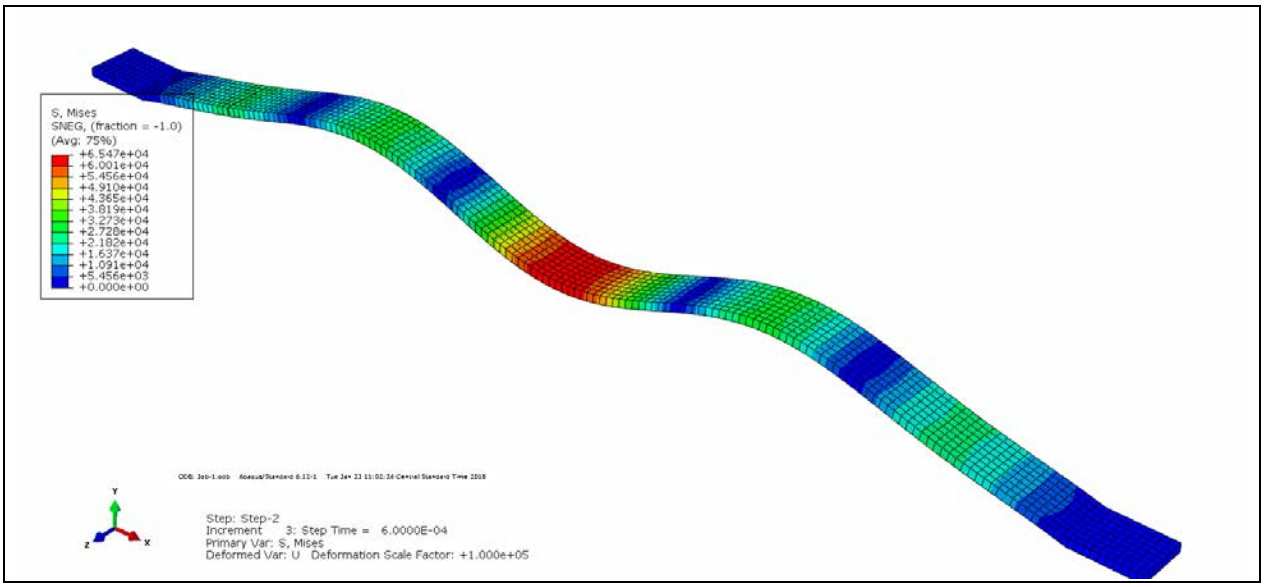

Figure 5-2 Stress distribution along the curved at 0.0006 sec time increment (deformation scale 1:10000).

In both the healthy and damaged scenarios, the angular velocity and the linear acceleration responses in the time-history were measured at node pairs (1-2), Figure 5-3. The transmissibility between each pair was calculated for both scenarios (healthy and damaged) and for both angular velocity and linear acceleration using the same frequency band (high coherence 150-390 Hz), as shown in Figure 5-4. The transmissibility of the undamaged scenario was considered as the baseline of the damage index calculations.

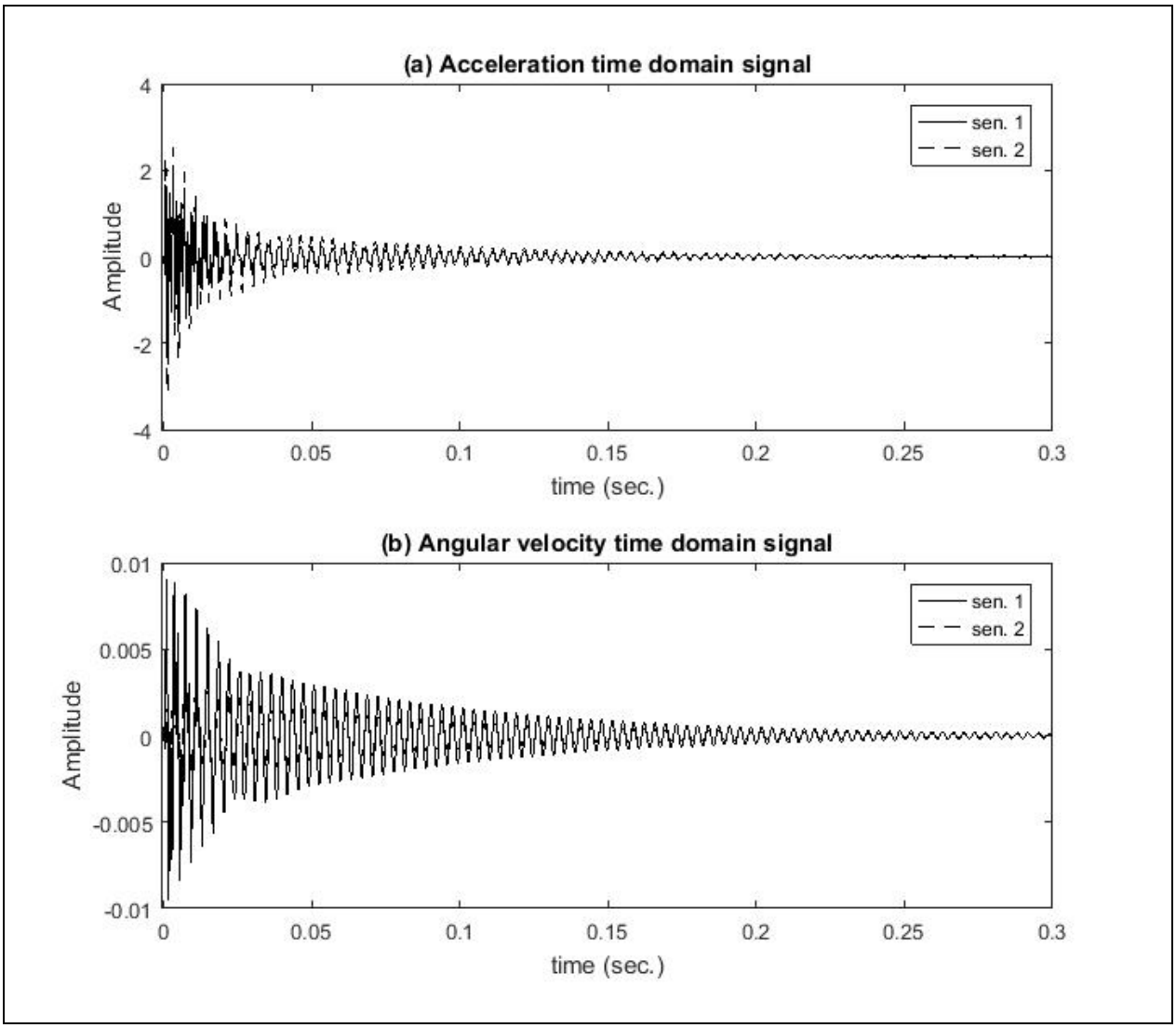

Figure 5-3 (a) Acceleration in the time domain of the healthy scenario of sensors 1 and 2, and (b) angular velocity in the time domain of the healthy scenario of sensors 1 and 2.

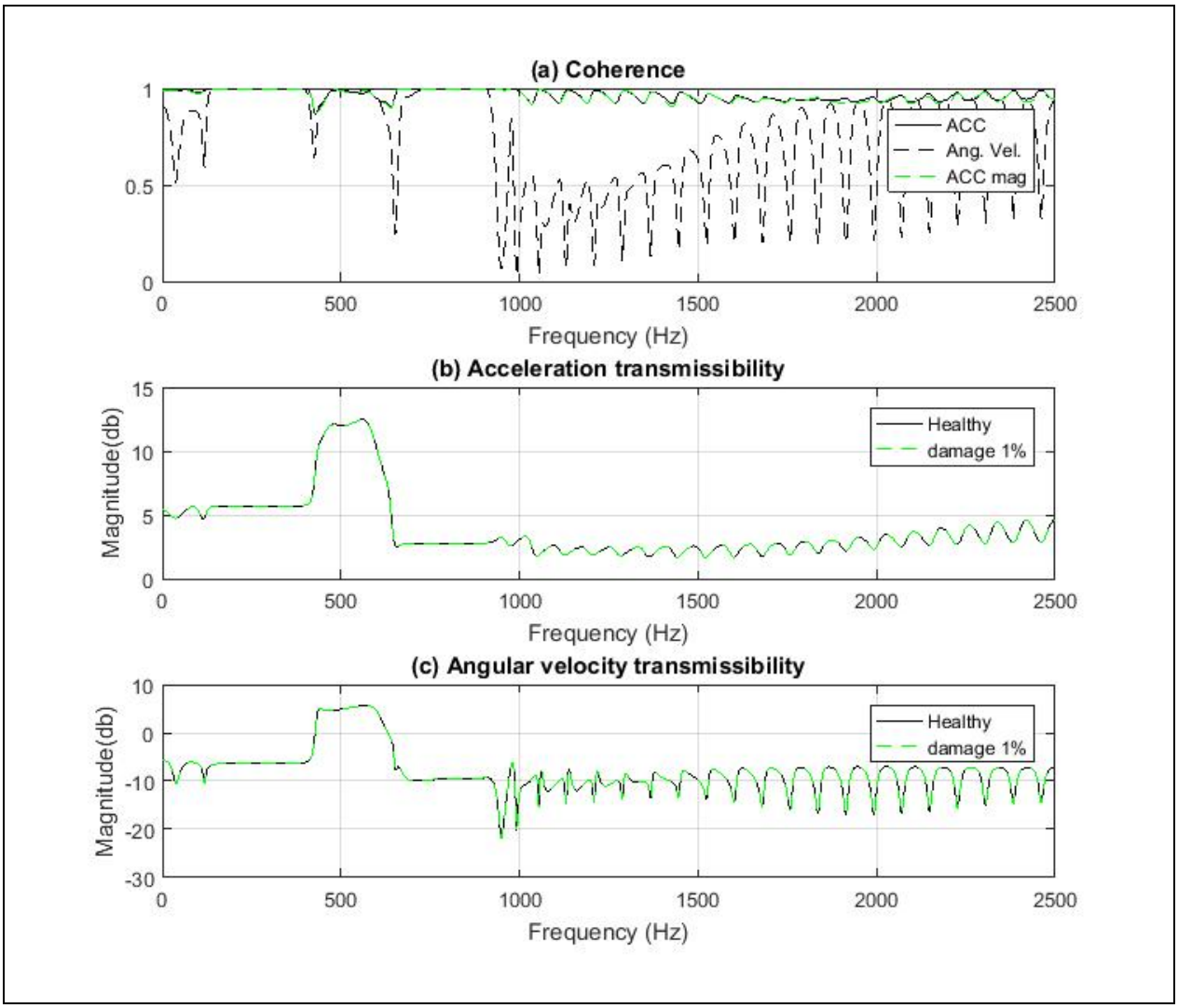

Figure 5-4 (a) The coherence of the acceleration signal, the angular velocity signal, and the acceleration magnitude signal, (b) the transmissibility based on acceleration, (c) the transmissibility based on angular velocity.

Figure 5-5 shows that the transmissibilities based on angular velocity, linear acceleration and the magnitude of acceleration were successfully detecting the damage at the damage location. The magnitude of the damage indictor based on the angular velocity was much larger than the magnitude of that based on the linear acceleration and that based on the acceleration magnitude, indicating that the angular velocity is more sensitive to the same amount of damage.

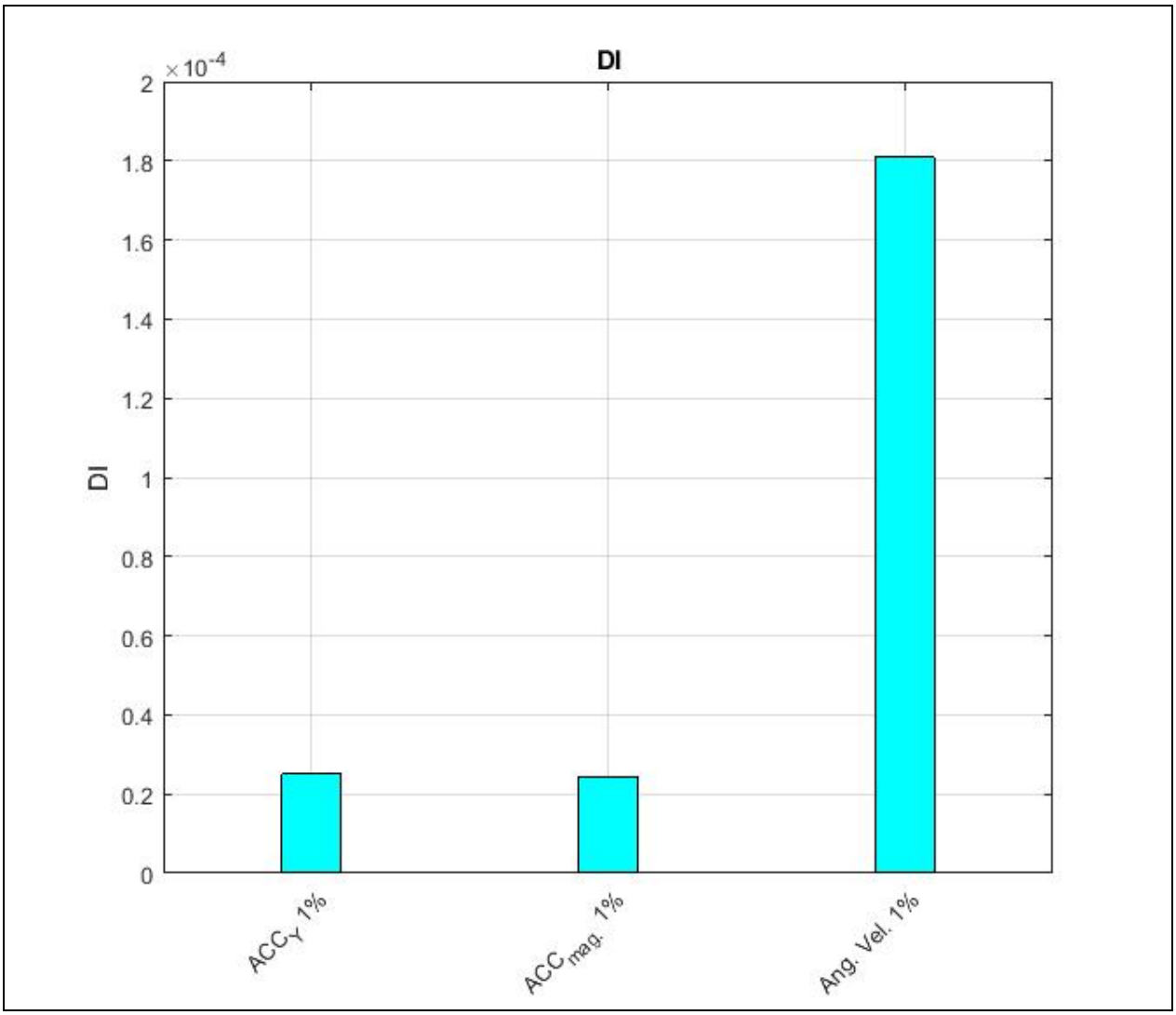

Figure 5-5 The transmissibility based on linear acceleration in the Y-direction, the magnitude of the acceleration, and the angular velocity damage indices of a curved beam calculated for the 1% reduction of stiffness between pair 1-2 (damage location). ACC_Y: acceleration in the Y-direction, ACC_{mag}: acceleration magnitude of the Y-direction and X-direction.

5.2.2. Sensitivity Analysis (Vertical Curved Beam)

A sensitivity analysis was conducted to investigate the effect of the orientation of the collected data on the transmissibility based on the acceleration damage detection and compare it with the transmissibility based on angular velocity. Four scenarios with different chord-height-to-length ratios have been considered to accomplish this purpose. Similar boundary conditions and applied loads were imposed on the four scenarios with the same chord length and different chord height.

5.2.2.1 The Analysis Setup

The setup of the study is similar to the previous example, shown in Figure 5-1. Fixed-ended curved beams with higher chord-height-to-length ratios were used in the analysis. The chord length of this curved beam was 0.75 m and the chord heights were 0.01 m, 0.05 m, 0.1 m, and 0.15 m, respectively, as shown in Figure 5-6. The beams had a rectangular cross-section of 0.0381 m width and 0.00635 m depth. The beams were made from steel with a density of 7860 kg/m^3 and a Young's Modulus of 210 GPa and were considered healthy or undamaged. The beams were loaded with an impulse point loading of 5 N/s in the middle.

A damage was introduced to the beams by reducing the stiffness of the damage element by 1% (length of 0.001 m along the curved beams) at a location 0.0631 m from the left support of the beam (Figure 5-1a) to investigate the sensitivity of the method to the damage and to the orientation of the sensors on the beams.

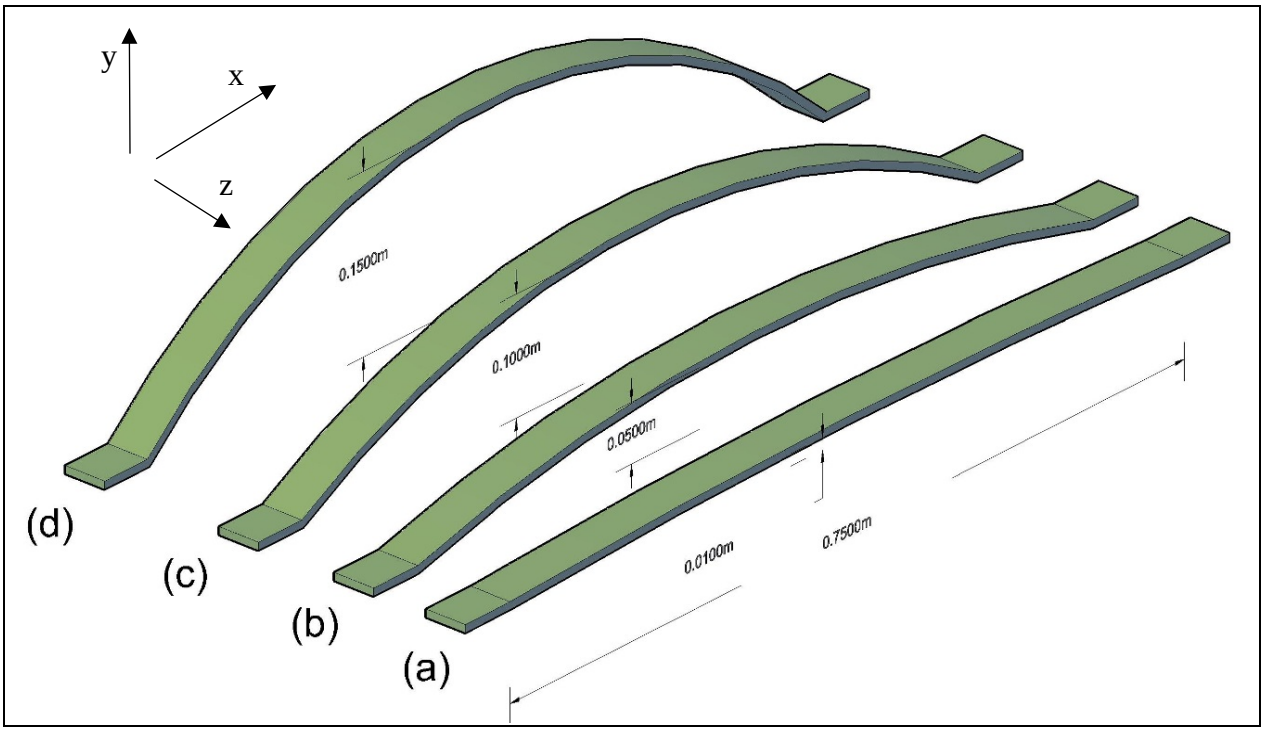

Figure 5-6 Sensitivity analysis setup with different chord-height-to-length ratios: (a) chord height 0.01 m, (b) chord height 0.05 m, (c) chord height 0.1 m, and (d) chord height 0.15 m.

As shown in Table 5-1 and Figure 5-7, the damage index for each scenario has been calculated. As shown in Table 5-1 and Figure 5-7, the damage indices based on angular velocity for the scenarios of the beams with chord heights of 10 mm to 150 mm are relatively similar values. In contrast, the damage indices based on the acceleration in the Y-direction increased as the beam chord height increased from 10 mm to 50 mm, 50 mm to 100 mm, and 100 mm to 150 mm by 99.9%, 114%, and 136%, respectively. Also, the damage indices based on the acceleration magnitude increased as the beam chord height increased from 10 mm to 50 mm by 148% and decreased when the beam chord height increased from 50 mm to 100 mm, and from 100 mm to 150 mm by 4.6% and 35.9%, respectively.

Table 5-1 Damage index of the damaged beams with different chord heights. ACC_Y: acceleration in the Y-direction, ACC_mag: acceleration magnitude of the Y-direction and X-direction.

Chord Height (mm)	Damage Index			
	ACC_Y	ACC_mag.	Ang. Velocity	Frequency band (Hz)
10	1.26E-05	9.86E-06	1.81E-04	210-450
50	2.51E-05	2.45E-05	1.81E-04	150-390
100	2.80E-05	2.33E-05	1.83E-04	155-380
150	3.18E-05	1.50E-05	1.85E-04	150-350

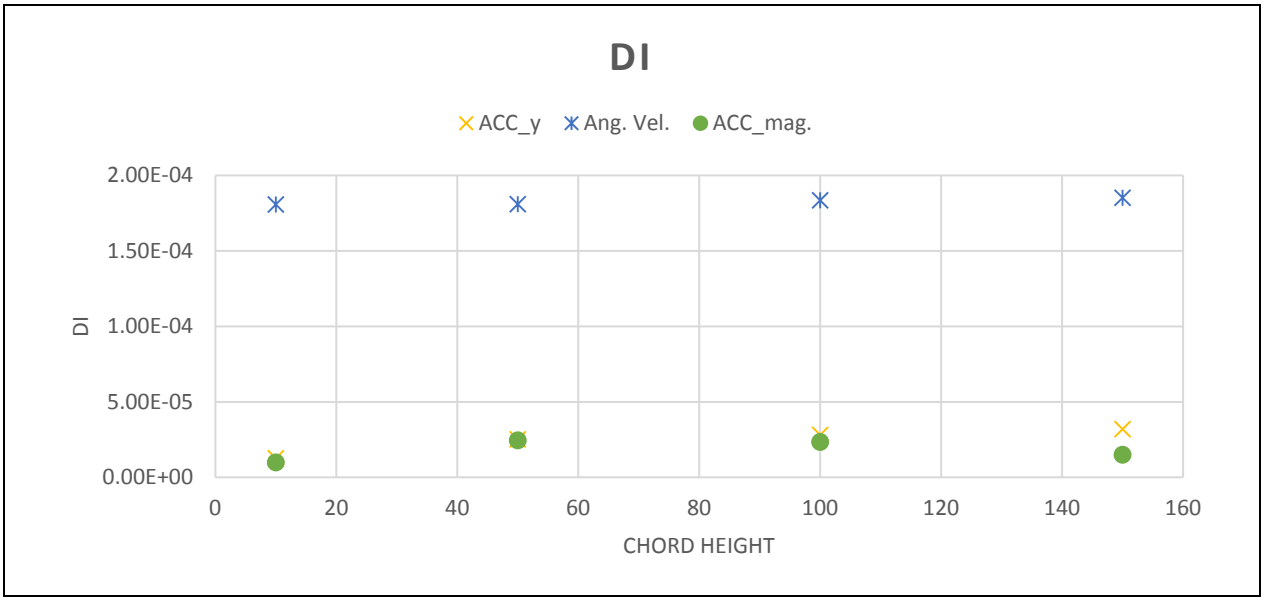

Figure 5-7 Transmissibility based on the acceleration in the Y-direction, angular velocity, and the acceleration magnitude damage index of the damaged beams with different chord heights. ACC_Y: acceleration in the Y-direction, ACC_mag: acceleration magnitude of the Y-direction and X-direction.

5.2.3. Numerical Example (Horizontally Curved Beam)

A fixed-ended beam is used in this section to investigate the capability of the proposed methodology in detecting damage for a horizontally curved beam, as shown in Figure 5-8. The horizontal distance between the fixed supports (chord length) was 0.75 m, the distance between the imaginary center line of the fixed supports and the mid-span of the curved beam (chord height) was 0.05 m, and the rectangular cross-section was 0.0381 m in width and 0.00635 m in depth. It was made from steel with a density of 7860 kg/m^3 and a Young's Modulus of 210 GPa and was considered healthy or undamaged. The beam was loaded with an impulse point loading of 5 N/s at the middle of the horizontally curved beam as shown in Figure 5-8. Figure 5-9 shows the deformable shape of the finite element beam. A damage of 0.001 m in length and 1% severity was introduced to the left side of the beam by reducing its stiffness, as shown in Figure 5-8a.

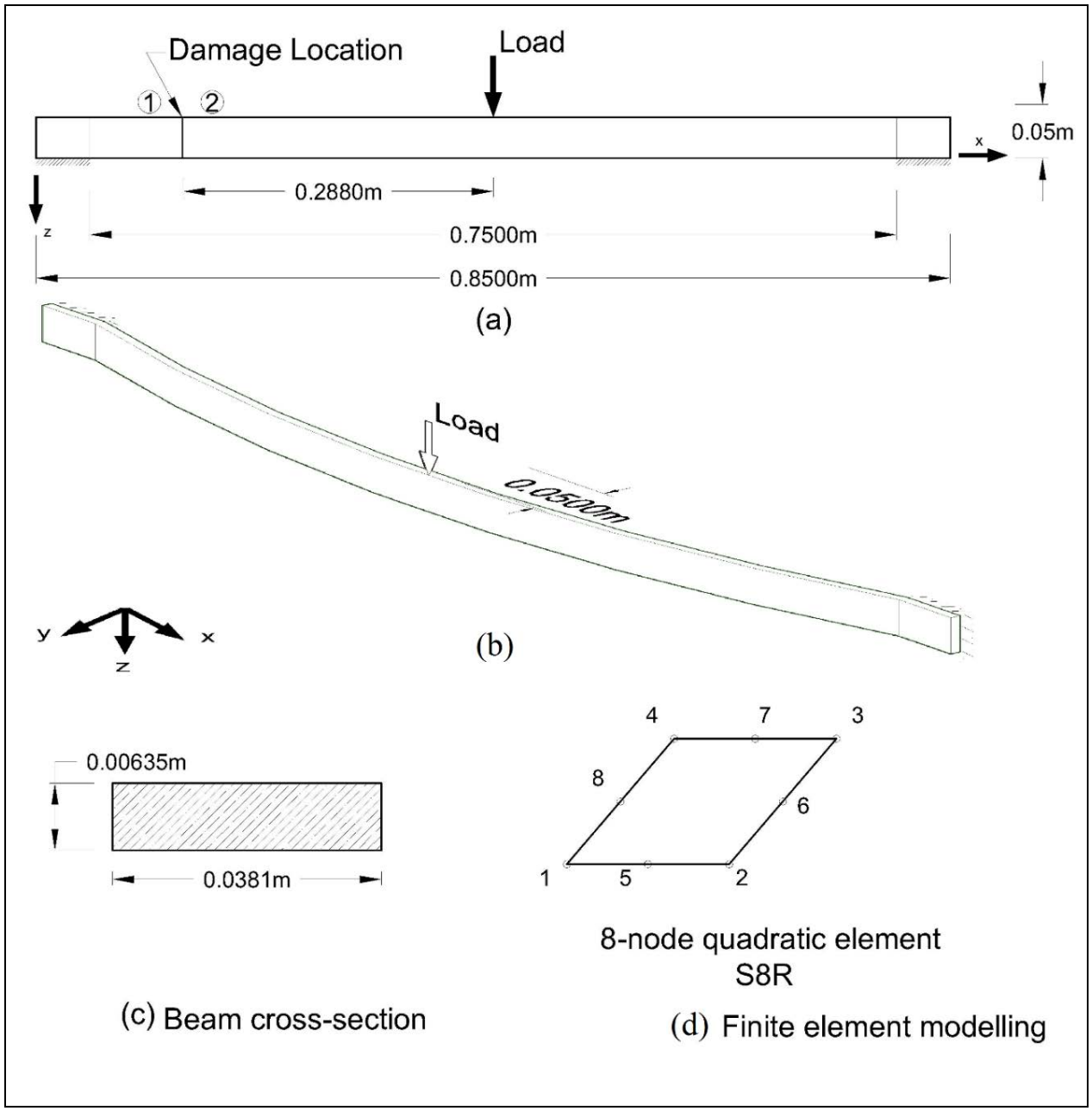

Figure 5-8 (a) Front layout schematic representation of the fixed-ended beam, (b) isometric view of the horizontally curved beam with 0.05 m chord height, (b) dimension of the cross-sectional area of the beam, and (d) finite element beam model used in the analysis.

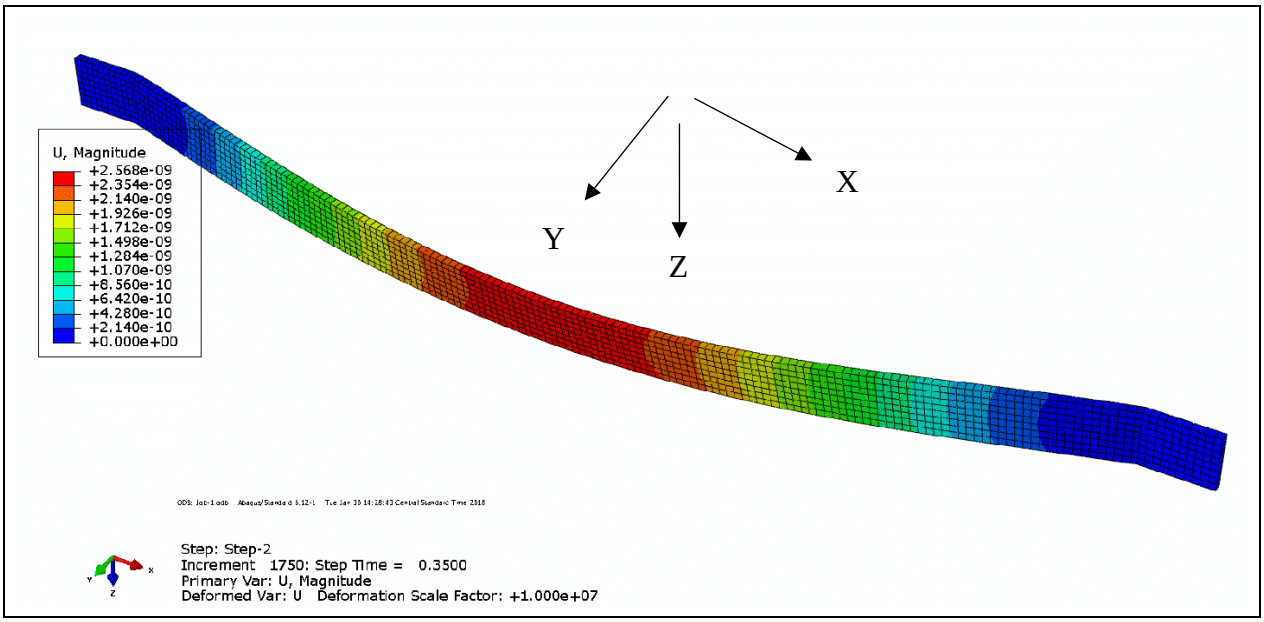

Figure 5-9 The deformed shape and the finite element modeling of the horizontally curved beam at 0.35 sec time increments (deformation scale 1:10000000).

As with the previous example, for both the healthy and damaged scenarios, the linear acceleration in the Z-direction (Figure 5-9) and the angular velocity in the Y-direction responses in the time-history were measured at node pairs (1-2) (Figure 5-10). The transmissibility between each pair was calculated for both scenarios (healthy and damaged) and for both linear acceleration and angular velocity using the same frequency band (high coherence 110-500 Hz), as shown in Figure 5-11. The transmissibility of the undamaged scenario was considered as the baseline for the damage index.

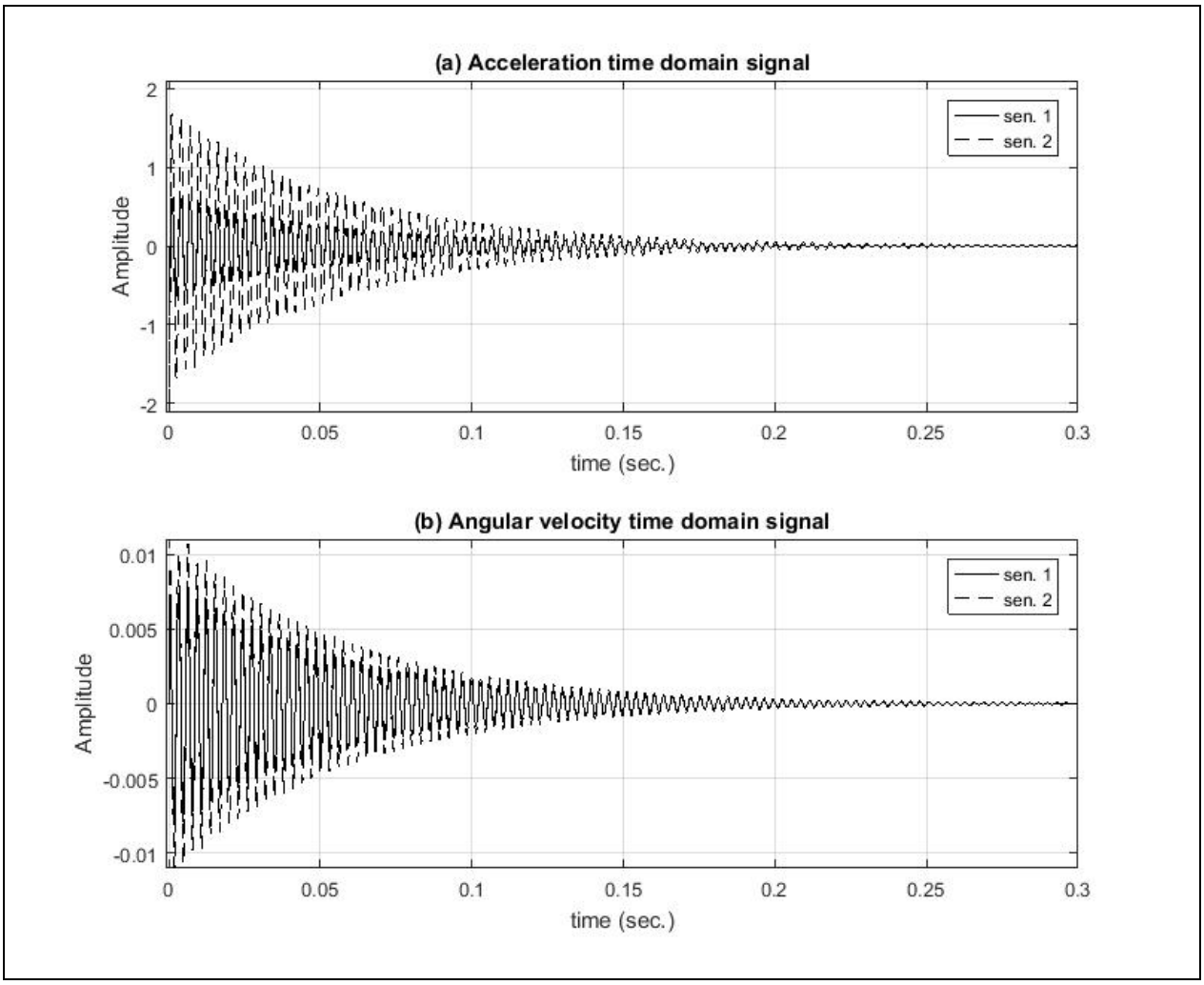

Figure 5-10 (a) Acceleration in the time domain in the Z-direction of the healthy scenario of sensors 1 and 2, and (b) angular velocity in the time domain in the Y-direction of the healthy scenario of sensors 1 and 2.

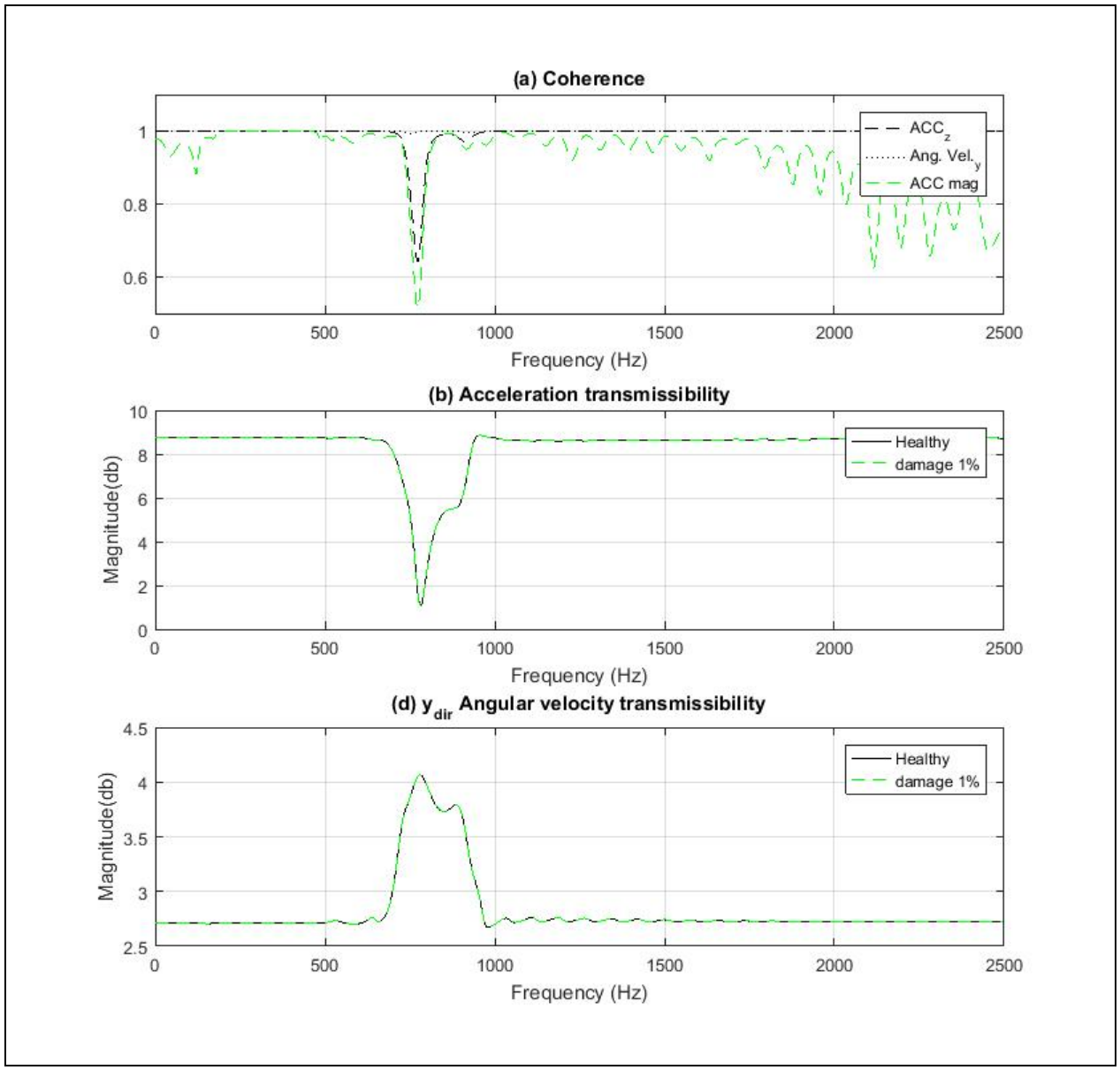

Figure 5-11 (a) The coherence of the acceleration signal in the Z-direction, the angular velocity signal in the Y-direction, and the acceleration magnitude signal, (b) the transmissibility based on acceleration, and (c) the transmissibility based on angular velocity.

As shown in Figure 5-12, the transmissibility based on linear acceleration, the magnitude of acceleration, and the angular velocity successfully detected the damage at the damage location. The magnitude of the damage index based on the angular velocity was 7.15 times larger than the magnitude of that based on the linear acceleration and 11.59 times larger than the damage index of that based on acceleration magnitude, indicating that the angular velocity is more sensitive to the same amount of damage.

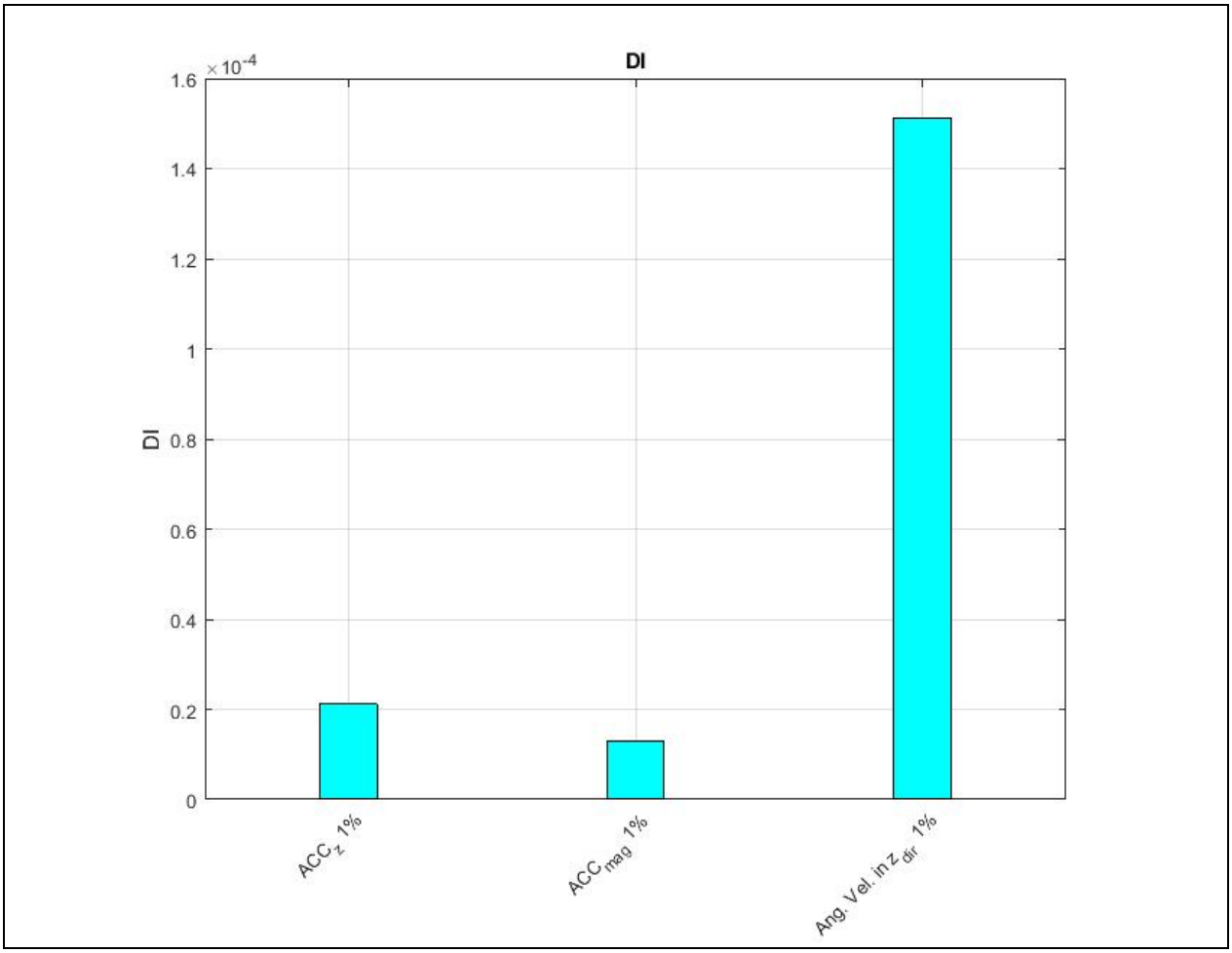

Figure 5-12 The transmissibility based on linear acceleration in the Y-direction, the magnitude of the acceleration, and angular velocity damage indices of a curved beam calculated for the 1% reduction of stiffness between pair 1-2 (damage location). ACC_z: acceleration in the Z-direction, ACC_{mag}: acceleration magnitude of the Z-direction and X-direction.

5.2.4. Sensitivity Analysis (Horizontally Curved Beam)

A sensitivity analysis was performed on the horizontally curved beam to investigate the effect of changing the length of the chord height on the damage index based on the acceleration in the Z-direction, acceleration magnitude, and angular velocity in the Y-direction. Four scenarios were considered to accomplish this purpose with different chord-height-to-length ratios. Similar boundary conditions and applied loads were imposed on the four scenarios with the same chord length and different chord heights.

5.2.4.1 The Analysis Setup

The setup of the study was similar to the previous example of the horizontally curved beam, shown in Figure 5-8. Fixed-ended curved beams with different chord-height-to-length ratios were used in the analysis. The chord lengths of the horizontally curved beams were 0.75 m and the chord heights were 0.01 m, 0.05 m, 0.1 m, and 0.15 m, respectively, as shown in Figure 5-8. The beams had a rectangular cross-section of 0.0381 m width and 0.00635 m depth. The beams were made from steel with a density of 7860 kg/m^3 and a Young's Modulus of 210 GPa and were considered healthy or undamaged. The beams were loaded with an impulse point loading of 5 N/s in the Z-direction on the middle of the beams.

A damage was introduced to the beams by reducing the stiffness of the damage element by 1% (length of 0.001 m along the curved beams) at a location 0.0631 m from the left support of the beam (Figure 5-8a), to investigate the sensitivity of the damage index of the different data measurements.

As shown in Table 5-2 and Figure 5-13, the damage index for each scenario has been calculated. The damage indices based on angular velocity for the scenarios of the beams with different chord heights of 10 to 150 mm were very similar. In the case of acceleration in the Z-direction, the damage index decreased by 17.3% when the beam chord height increased from 10 mm to 50 mm and increased by 6.3% when the chord height changed from 50 mm to 100 mm. When the chord heights changed from 100 to 150 mm, the damage index of the acceleration in the Z-direction decreased by 19.5%.

The damage indices based on the acceleration magnitude decreased by 33.6% when the beam chord height increased from 10 mm to 50 mm and increased by 66.8% when the beam chord height increased from 50 mm to 100 mm. When the chord heights changed from 100 to 150 mm, the damage index decreased by 8.3%, as shown in Table 5-2 and Figure 5-13.

Table 5-2 Damage index of the damaged beams with different chord heights for the horizontally curved beam. ACC_Z: acceleration in the Z-direction, ACC_mag: acceleration magnitude of the Z-direction and X-direction.

Chord Height (mm)	Damage Index			
	ACC_Z	ACC_mag.	Ang. Velocity_Y	Frequency band (Hz)
10	2.56E-05	1.97E-05	1.56E-04	200-490
50	2.12E-05	1.31E-05	1.51E-04	110-500
100	2.25E-05	2.18E-05	1.50E-04	140-400
150	1.81E-05	2.00E-05	1.51E-04	10-350

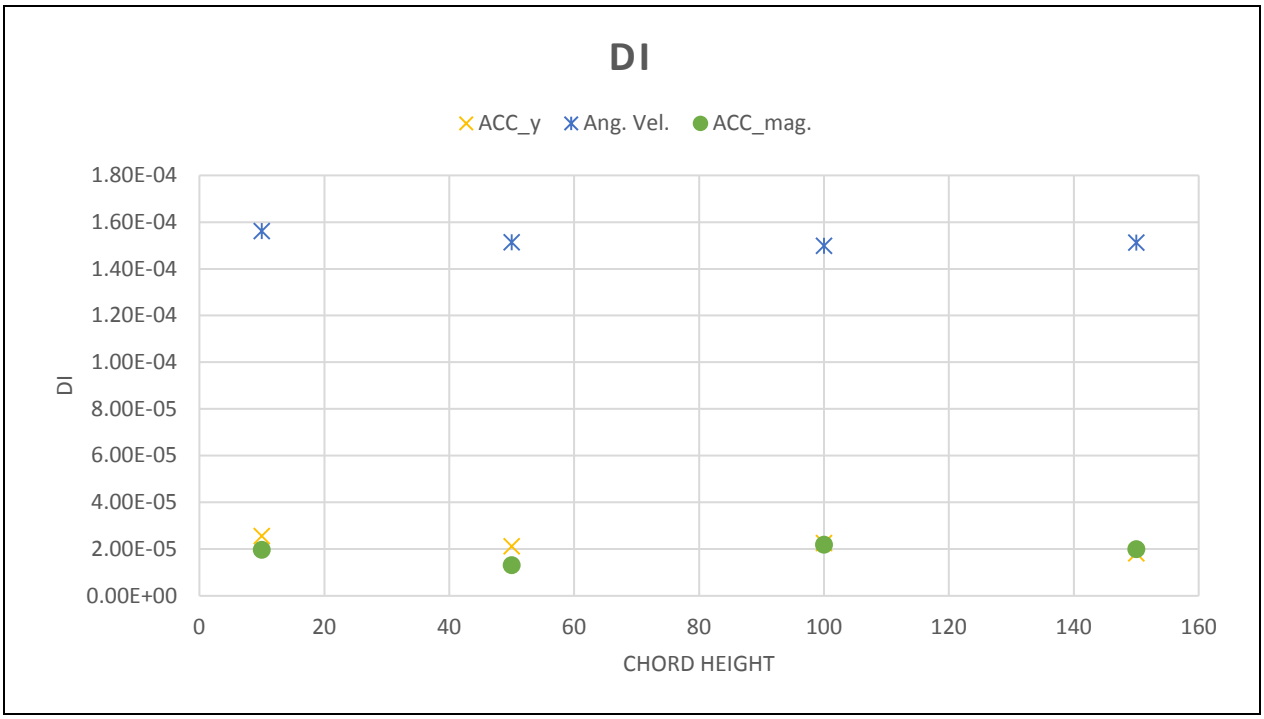

Figure 5-13 Transmissibility based on acceleration in the Z-direction, angular velocity in the Y-direction, and the acceleration magnitude damage index of the damaged horizontally curved beams with different chord height. ACC_Z: acceleration in the Z-direction, ACC_mag: acceleration magnitude of the Z-direction and X-direction.

5.3. Discussion and Conclusion

The transmissibility-based damage-detection method using the angular velocity was compared with another method that uses the accelerations and the magnitude of the acceleration. The acceleration in the vertical direction was used in this work as a measure for the acceleration, as it is expected that people may install the main axis of the accelerometers in the direction of gravity. However, if the axis of the accelerometers is orientated toward the center of the curved structures, then care should be taken to remove the measured gravity component from the acceleration measurements. The total acceleration magnitude of the horizontal and vertical directions was also calculated and used in this work for the damage index calculation for the sensitivity analysis for both the vertically and horizontally curved beams. The results, however, showed that the damage index based on the acceleration magnitude gave lower values than those calculated based on the vertical direction of the acceleration.

In addition, the transmissibility based on the angular velocity damage index magnitude was slightly affected when changing the chord height for the vertically and horizontally curved beams. In contrast, the transmissibility based on the acceleration in the vertical direction and the acceleration magnitude damage index varies significantly when the chord height changed for both vertically and horizontally curved beams.

CHAPTER SIX: HEALTH MONITORING AND UPDATING OF STRUCTURE SUPPORTS

6.1. Introduction

Structural supports are crucial elements in any structural system, but especially in bridges. In bridge systems, the supports or bearings hold the superstructure and transfer the loads to the substructure. Changes in the health conditions of the supports, such as rusting and cracking, can cause noticeable changes in the response of the superstructure and the way loads are transferred to the abutment and piers. Different types of bridge supports have been used to accommodate different purposes and the challenges presented by loads. Elastomeric, sliding, high-load multi-rotational, and fabricated steel supports are some common types of bearings used in bridge systems; each type has advantages and potential disadvantages [48]. Fabricated steel bearings are the focus of the current study since they have been widely used and are considered the oldest of the bearing types.

Various factors affect the service life of bridge bearings. One factor is corrosion of the exposed steel element and debris buildup at the bearing point, which affects the proper rotation and expansion movements of the superstructure. Debris may become impacted or wedged at the bearing location, restricting the movement of the bearing [48, 49]. If the bearing movement is not proper for the design specification, new or different stresses will be introduced and will be transmitted to the other members of the bridge [50], possibly generating different types of failure.

Early detection of support deficiency can allow maintenance or repair management before catastrophic failure can occur. A few studies have investigated the damage detection and health monitoring of bridge bearings. Barr et al. [47] investigated the effect of changing the state of the boundary conditions on the dynamic response of a curved steel I-girder bridge in Salt Lake

City, Utah. Cornwell et al. [51] studied the effect of environmental variability on the modal properties of the Alamosa Canyon Bridge in southern New Mexico. They suggested that, because of the inappropriate function of the expansion joints (due to accumulation of debris and the temperature differential), the boundary conditions of the structure were altered, causing alteration in the resonant frequencies of the bridge. González and Aied [52] employed the Hilbert-Huang transform to characterize the features and identify the changes in the response of a lead rubber bearing. However, the accuracy of the proposed method was limited by the noise level.

Besides the health monitoring of structural bearings, some of the research studies considered the boundary conditions in the model updating process. Park et al. [53] used a neural network to evaluate the boundary conditions and used artificial rotational spring constants at the supports to represent the effects of aging and constraining of the boundary conditions. Dilena et al. [54] highlighted the importance of considering the boundary condition by modeling the supports as linear elastic springs to obtain the damage evaluation in a reinforced concrete bridge using finite element model updating. Aktan et al. [55] introduced a manual finite element model update considering the boundary conditions of the bridge by implementing rotational and translational springs at the supports. Brownjohn et al. [56] modeled the abutment restraints as rotational springs in the assessment of a highway bridge's refurbishing and strength through dynamic testing and model updating. Some researchers simulated the resulting restraints on the supports by a change in the stiffness of rotational springs added to the support [57]. Zhang et al. [58] presented a finite element model updating of the Kap Shui Mun cable-stayed bridge based on the measured frequencies. The boundary conditions were considered as updating parameters in the updating process but could not be verified to the actual values.

Previous work has shown the effectiveness of using the transmissibility in structural health monitoring. The transmissibility function represents the ratio in the frequency domain of two measured responses (output-only) in the structure. Since it represents the antiresonance, it contains valuable information about the dynamic parameters, such as the mode shape and the natural frequencies of the structure [25, 59]. Recent studies have shown that certain frequency bands in the transmissibility function can be chosen to avoid the uncertainty in the information provided by the transmissibility function [22, 26-29, 34]. Schallhorn and Rahmatalla [23] employed the transmissibility function to assess the condition of a highway bridge on Highway 30 in Iowa and used the coherence as a guide to select the frequency bands.

Recently, Al-Jailawi and Rahmatalla [34] introduced the concept of angular-velocity-based transmissibility and showed its superiority to the traditional acceleration-based transmissibility in detecting damage on structural systems. The purpose of this chapter is to extend the application of the angular-velocity-based transmissibility and test its validity in detecting the health condition and in updating the model of the resistance of the supports. This chapter is organized as follows: Section 6.2 presents the theoretical background and mathematical foundation of the proposed method. Section 6.3 demonstrates the application of the proposed methodology on a simply supported numerical beam example, and Section 6.4 presents the experimental application of the method. Finally, Section 6.5 presents the discussion of the results.

6.2. Theoretical Background

The principle of superposition is employed in this work to extract the relationship between the structural response and the resistance at the support represented by a rotational spring. A simply supported pin-roller beam, with an added rotational spring at the right end, is presented in this section (Figure 6-1) to resemble a simplified bridge structure. The beam has a length (L), flexural rigidity (EI), and is subjected to a constant load (P) at its center. A rotational spring with stiffness (K_θ) is attached to the right support of the beam to resemble the changes in the bearing's rotational resistance that can result from deterioration.

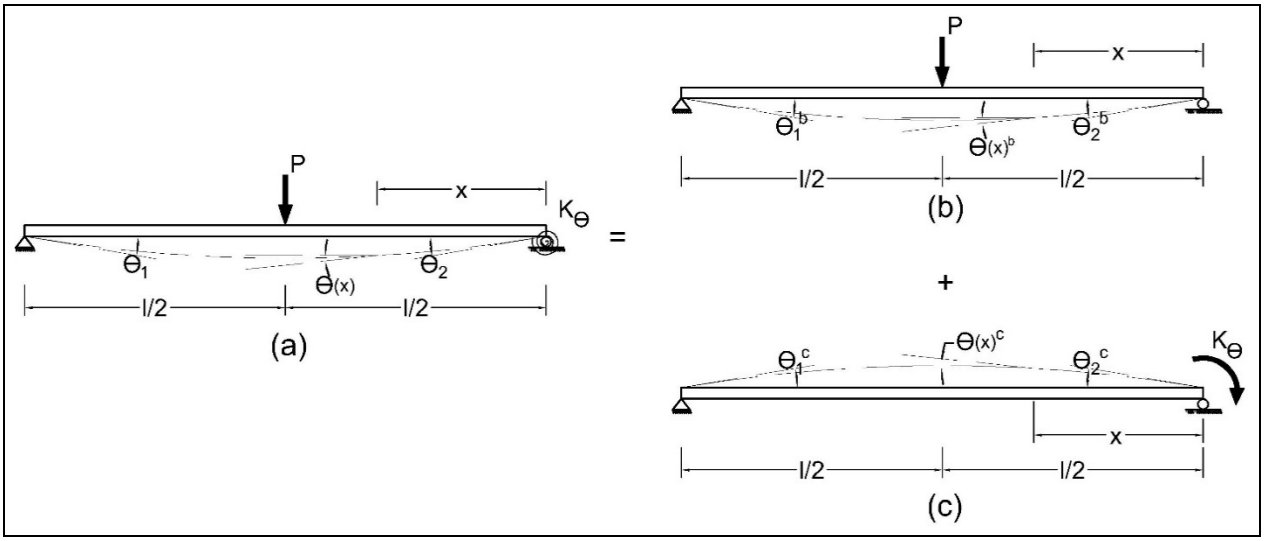

Figure 6-1 Principle of superposition of the simply supported beam with rotational spring: (a) original loading, (b) equivalent loading using the principle of super-position.

Figure 6-1a represents the original beam, while Figure 6-1b and Figure 6-1c represent the original beam with two loading cases that are equivalent to the original loading of the beam.

Using the principle of superposition:

$$\theta_{(x)} = \theta_{(X)}{}^{b} - \theta_{(X)}{}^{c} \tag{6-1}$$

where $\theta_{(x)}$ is the rotation at the right support of the original beam in Figure 6-1a, ${\theta_{(X)}}^{b}$ is the rotation at the right support due to the load at the middle of the beam in Figure 6-1b, and ${\theta_{(X)}}^{c}$ is the rotation at the right support due to the resistance at the right support of the beam in Figure 6-1c.

$${\theta_{(X)}}^{b} = \frac{P(L^2-4x^2)}{16\text{EI}} \qquad 0 \le x \le \frac{L}{2} \tag{6-2}$$

$${\theta_{(X)}}^{c} = \frac{M(2L^2-6Lx+3x^2)}{6\text{EI}L} \qquad 0 \le x \le L \tag{6-3}$$

Substitute in Eq. 6-1:

$$\theta_{(X)} = \frac{P(L^2-4x^2)}{16\text{EI}} - \frac{M(2L^2-6Lx+3x^2)}{6\text{EI}L} \qquad 0 \le x \le \frac{L}{2} \tag{6-4}$$

At x = 0 and $= K_\theta\ L$:

$$\theta_2 = \theta_{(X=0)} = -\frac{K_\theta L^2}{3\text{EI}} + \frac{L^2 P}{16\text{EI}} \tag{6-5}$$

Introducing the rotational ratio ζ, where

$$\zeta = \frac{\theta_{(X=0)}}{\theta_{(X)}} = \frac{L^2(16K_\theta-3P)}{-3P(L^2-4x^2)+8K_\theta(2L^2-6Lx+3x^2)} \tag{6-6}$$

Figure 6-2 shows a plot of the relationship between ζ and K_θ. As shown in this figure, the ζ value decreases as the rotational stiffness K_θ value increases, indicating that the beam will show less rotation at its right-end support when the stiffness resistance of the support becomes larger.

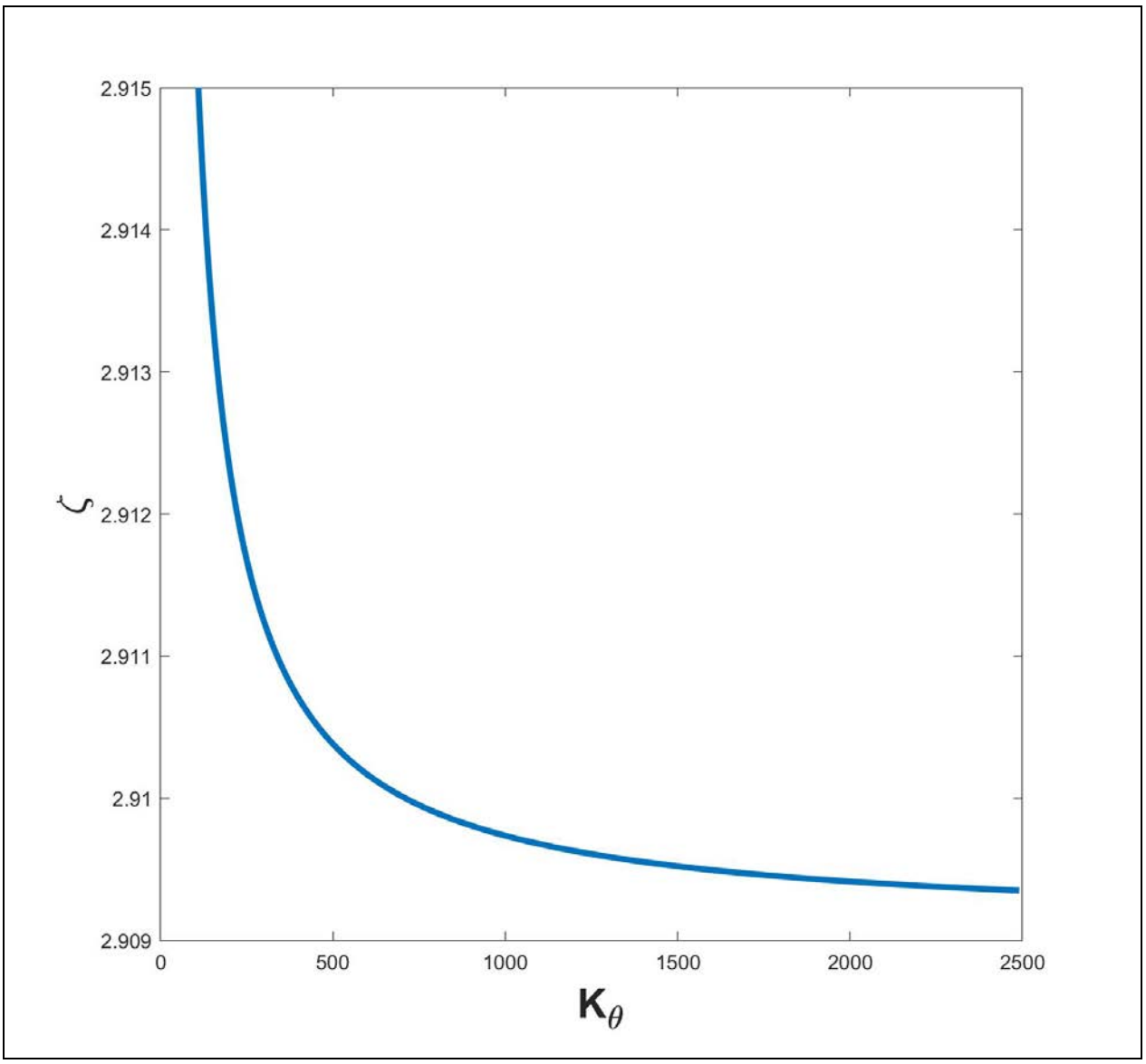

Figure 6-2 The relationship of the ratio ζ with K_θ assuming EI, L, P, and x constants.

6.2.1 Support Health Monitoring Index (SHMI)

The support- health-monitoring index (SHMI) in the current work is calculated by normalizing the difference between the transmissibility of the unhealthy and the transmissibility of the baseline or healthy for a selected frequency range φ.

Mathematically, SHMI can be evaluated using the following equation:

$$SHMI = \frac{\left\| \sum_{\varphi=i}^{n} T_{ij}^{d}(\varphi) - \sum_{\varphi=i}^{n} T_{ij}^{bl}(\varphi) \right\|}{\left\| \sum_{\varphi=i}^{n} T_{ij}^{bl}(\varphi) \right\|} \tag{6-7}$$

where T_{ij}^{d} is the transmissibility of the damaged structure and T_{ij}^{bl} is the transmissibility of the baseline (healthy) structure. The transmissibility in this work is defined as the ratio between the angular velocity at locations i and j in the neighborhood of the support [34]:

$$T_{ij}(\omega) = \frac{\dot{\theta}_i(\omega)}{\dot{\theta}_j(\omega)} \tag{6-8}$$

where $\dot{\theta}_i$ and $\dot{\theta}_j$ are the output angular velocities at locations i and j, respectively. The frequency range φ (Eq. 6-7) was selected based on the regions of high coherence γ_{ij} at locations i and j:

$$\gamma_{ij}(\omega) = \frac{|S_{ij}(\omega)|^2}{S_{ii}(\omega) S_{jj}(\omega)} \tag{6-9}$$

S_{ii} is the auto-spectral density of the sensor at location i, S_{ij} is the cross-spectral density between the sensors at locations i and j, and S_{jj} is the auto-spectral density of the sensor at location j.

6.2.2 Support Stiffness Resistance Updating (SSRU)

The same transmissibility and coherence functions used in the previous section for SHMI calculation are used in this section to update the changes in the stiffness of the support. A flow chart that illustrates the updating algorithm is shown in Figure 6-3. As shown in Figure 6-3, the updating process comprises two charts. In the first chart (the left side of Figure 6-3), an optimization process is carried out to update a finite element model (FEM) of the structure in its healthy condition. This is an important step in the process to make sure that the FEM adequately represents the healthy physical structure. In the second chart (on the right side of Figure 6-3), another optimization process is introduced to update the changes in the rotational resistance of the support (K_θ) as a result of the deterioration.

The optimization algorithm (Equation 6-10) was used in the left chart in Figure 6-3 to update the FEM of the healthy structure and can be stated as follows:

$$\min_{k} \left\| \sum_{\varphi=i}^{n} T_{ij}^{m}(\varphi) - \sum_{\varphi=i}^{n} T_{ij}^{u}(\varphi) \right\| \tag{6-10}$$

Subject to:

$E^{lo} \leq E \leq E^{up}$, $\rho^{lo} \leq \rho \leq \rho^{up}$, $d^{lo} \leq d \leq d^{up}$, $\alpha^{lo} \leq \alpha \leq \alpha^{up}$,

and $\beta^{lo} \leq \beta \leq \beta^{up}$

where T_{ij}^{m} is the measured transmissibility, T_{ij}^{u} is the updated transmissibility, and the frequency range φ was chosen based on the regions of high coherence. E^{lo} and E^{up} are the lower and upper limits of the modulus of elasticity of the material, ρ^{lo} and ρ^{up} are the lower and upper limits of the density of the material, d^{lo} and d^{up} are the lower and the upper limits of the dimensions of

the structure, and α^{lo} and α^{up}, β^{lo} and β^{up} are the lower and the upper limits of the damping ratios of the structure.

The following optimization algorithm (Equation 6-11) was used in the chart on the right side of Figure 6-3 to update the rotational resistance of the support:

$$\min_{k} \left\| \sum_{\varphi=i}^{n} T_{ij}^{m}(\varphi) - \sum_{\varphi=i}^{n} T_{ij}^{u}(\varphi) \right\| \tag{6-11}$$

Subject to:

$$K_{\theta}{}^{lo} \leq K_{\theta} \leq K_{\theta}{}^{up}$$

where $K_{\theta}{}^{lo}$ and $K_{\theta}{}^{up}$ are the lower and upper limits of the rotational stiffness at the support. The MATLAB function called “fminbnd” is used for the updating process. This algorithm is based on the golden section search and parabolic interpolation [60, 61].

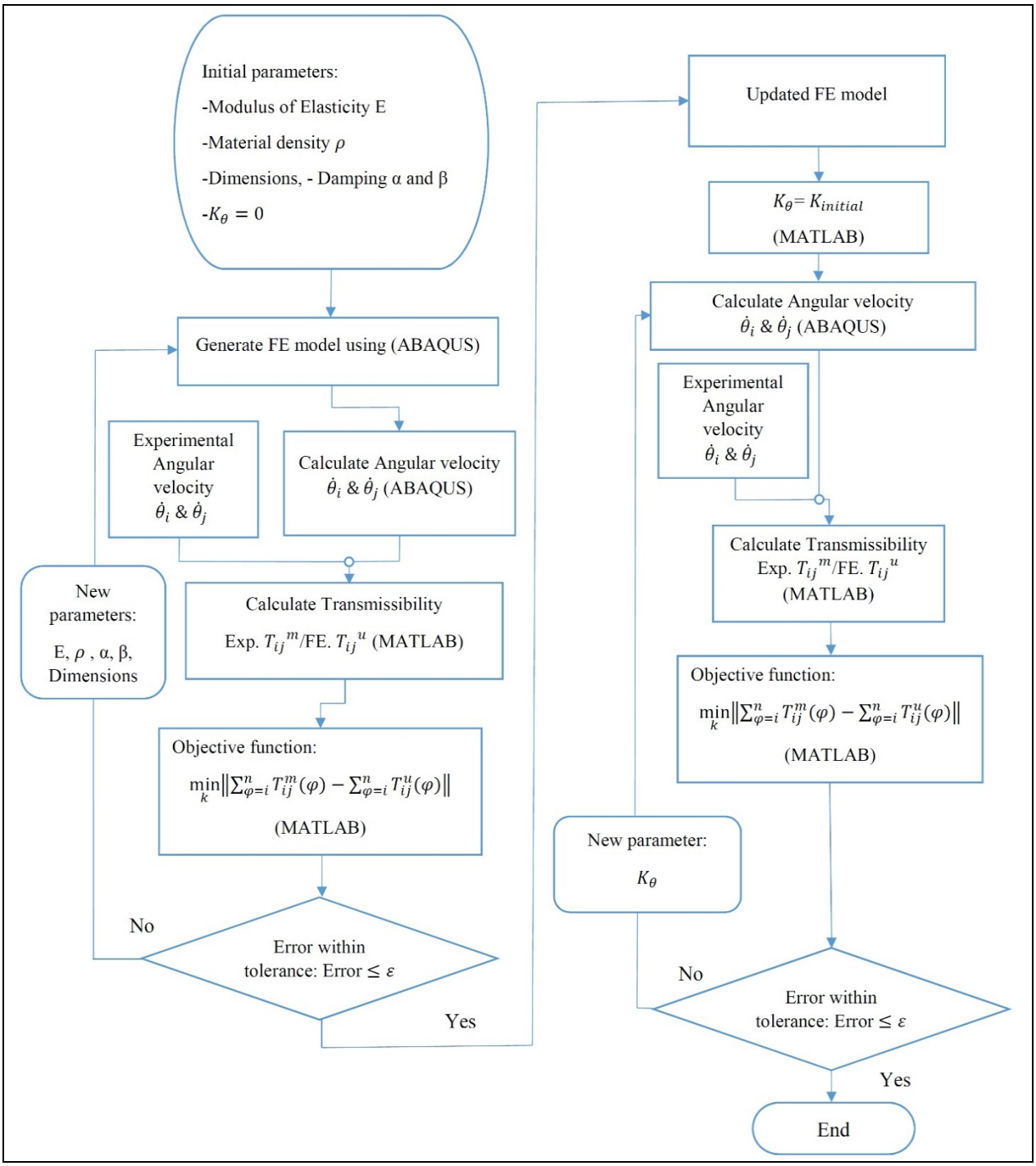

Figure 6-3 Flowchart of the updating process; the chart on the left represents the updating scheme of the healthy structure, and the chart on the right represents the updating process of the rotational resistance of the support due to deterioration.

6.3. Numerical Analysis

6.3.1. Simply Supported Beam Setup

A simply supported beam is used in this example to show the feasibility of the proposed SHMI and SSRU in detecting and updating the changes in the support stiffness conditions. The length of the beam was 0.8 m, and it had a rectangular cross-section of 0.0381 m width and 0.00635 m depth. It was made from steel with a density of 7860 kg/m^3 and a Young's Modulus of 200 GPa and was considered healthy or undamaged. The beam was loaded with an impulse point loading of 5 N/s at the middle as shown in Figure 6-4.

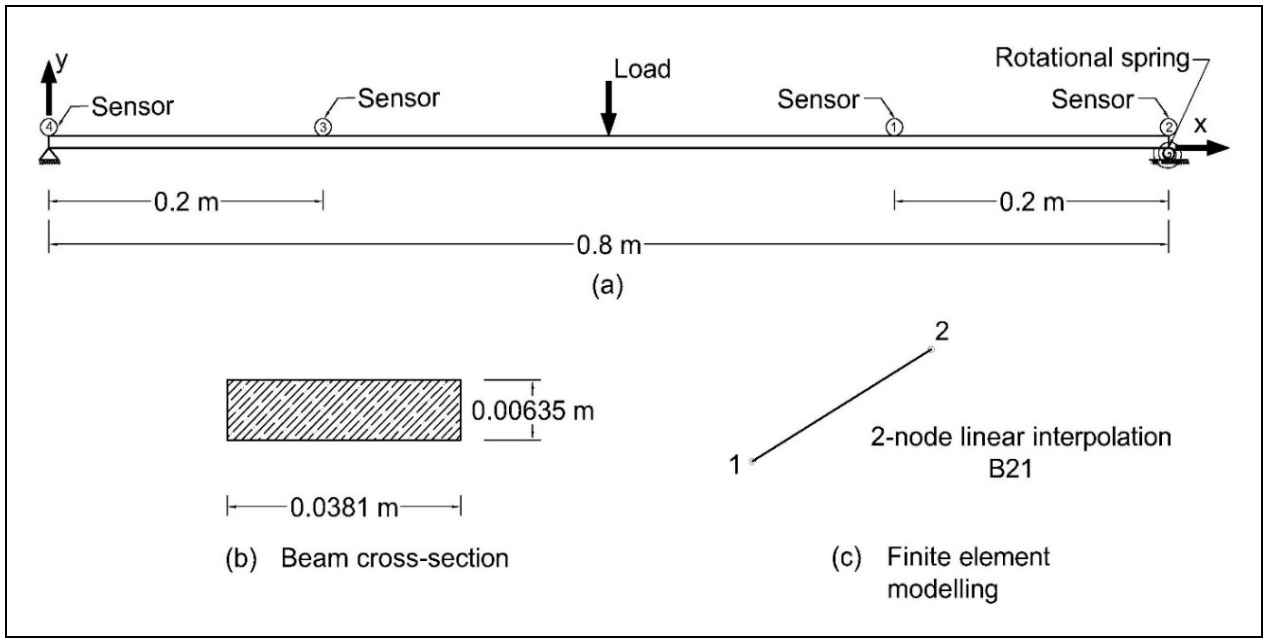

Figure 6-4 Schematic representation of a simply supported beam showing (a) the rotational spring with sensor locations 1,2 and 3,4 at the right and left supports, respectively, and the location of the applied load, (b) the dimension of the cross-sectional area of the beam, and (c) the finite element beam model used in the analysis.

A rotational spring was added to the right support to simulate the additional resistance caused by the deterioration at the support. The angular velocity was collected at locations x = 0 and x = 0.2 m on the left side of the beam, and at x = 0.6 m and x = 0.8 m on the right side of the beam. The rotational resistance of the roller support for the healthy condition will be considered to be negligible as compared to other deteriorated conditions; based on that, a stiffness of zero will be assigned to the support resistance for the healthy condition. Five cases of rotational stiffness deterioration scenarios (500, 1000, 1500, 2000, 2500 N.m/m/rad) were considered in this example.

6.3.2. Support Health Monitoring Index (SHMI)

The angular velocity, coherence, and transmissibility of the sensor pair 1-2 for the healthy and deteriorated support were calculated as shown in Figure 6-5 and Figure 6-6, respectively. A frequency band between 1-100 Hz was selected for the angular velocity response since the coherence function showed a high value and it was close to 1 at these frequencies, as shown in Figure 6-6a.

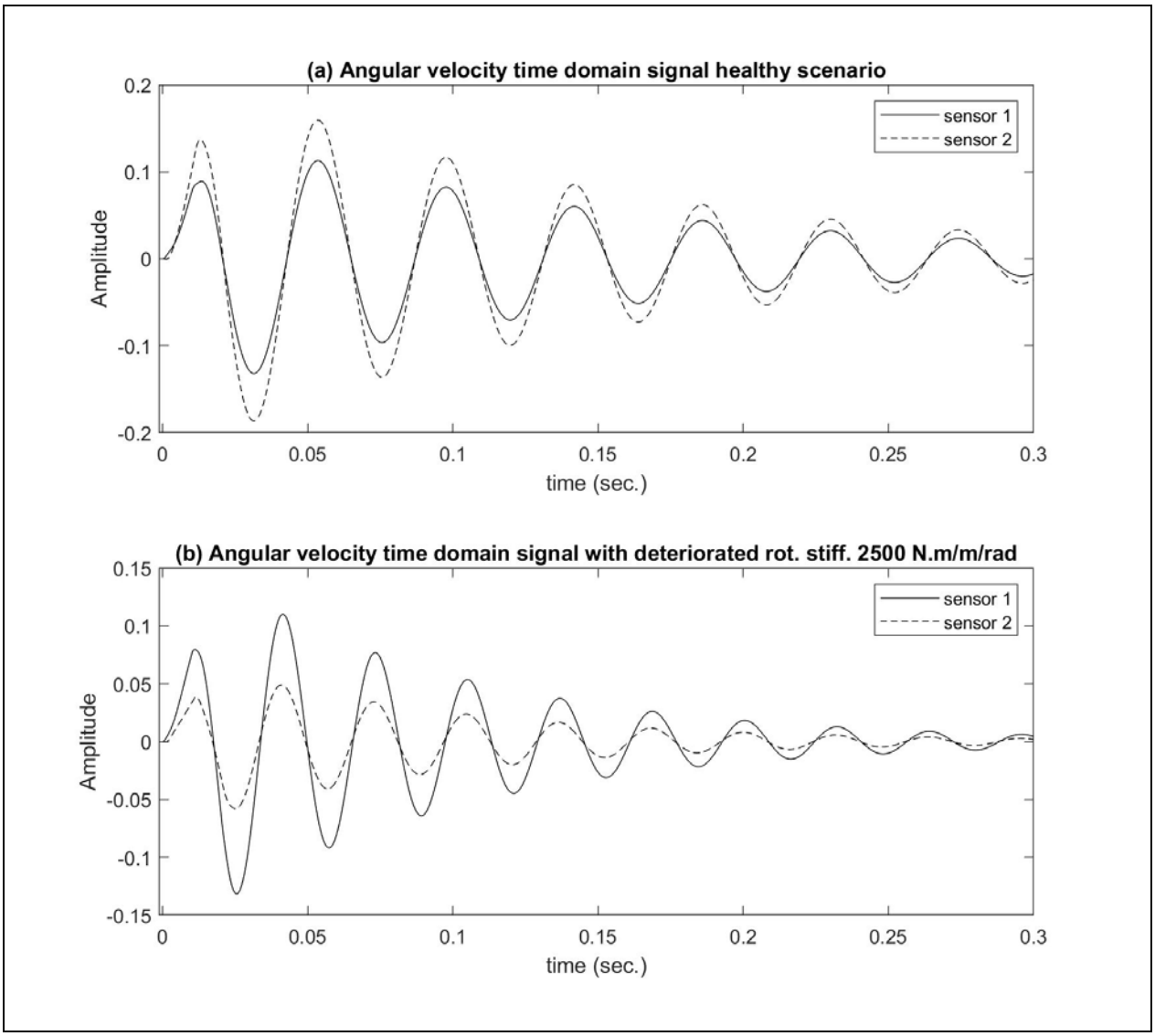

Figure 6-5 Angular velocity in (a) the time domain of the healthy scenario of sensors 1 and 2 with no rotational resistance at the right support, and (b) the time domain of sensors 1 and 2 of the scenario with rotational stiffness of 2500 N.m/m/rad at the right support.

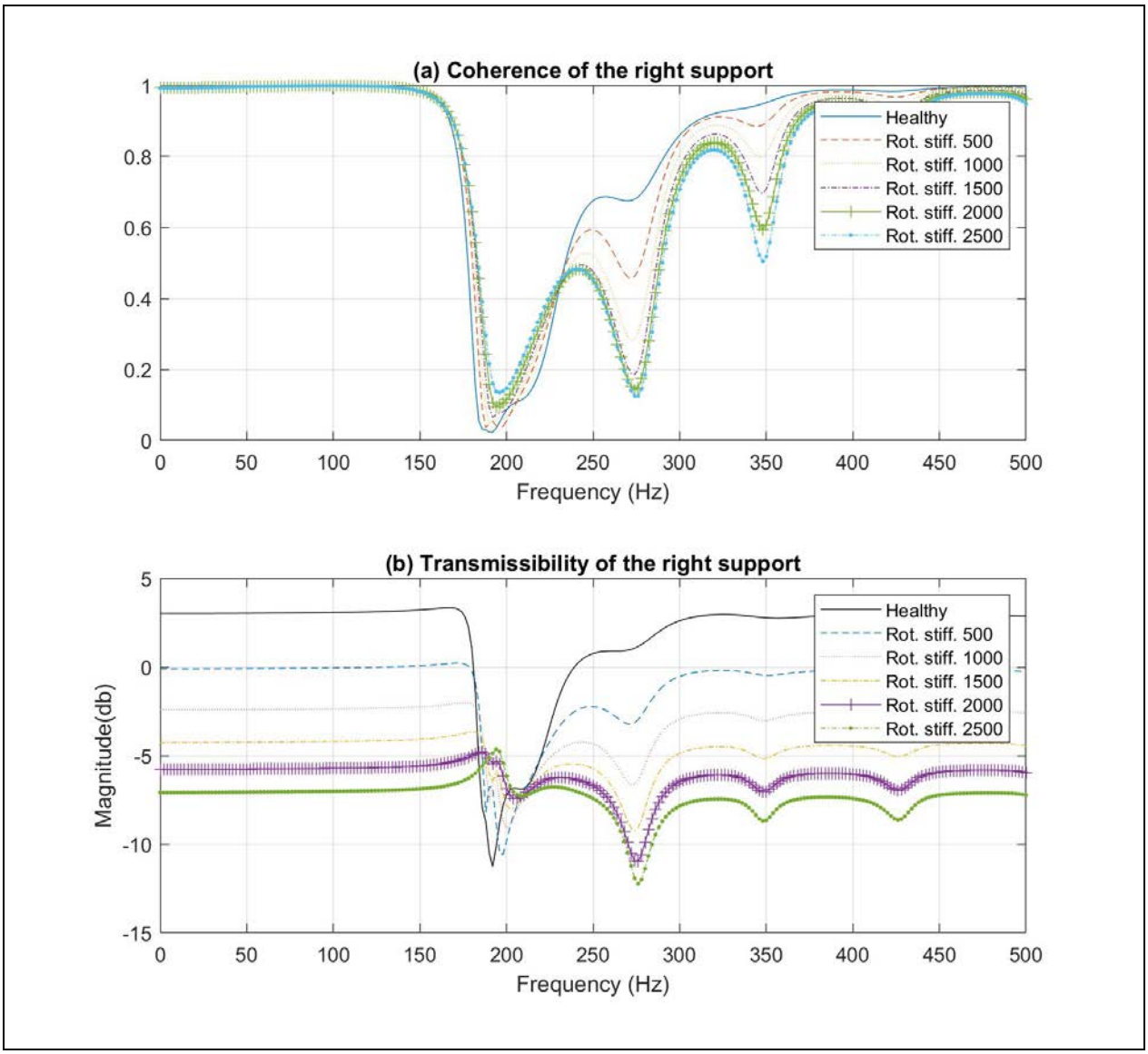

Figure 6-6 The coherence and transmissibility of the healthy scenario, and the scenarios with variable rotational stiffness at sensors 1 and 2: (a) coherence of the angular velocity signal, and (b) transmissibility of the angular velocity.

The calculated SHMI for the scenarios of increasing the rotational stiffness resistance (500, 1000, 1500, 2000, 2500 N.m/m/rad) for sensor pair 1-2 are shown in Figure 6-7. As can be seen from the figure, the magnitude of SHMI increases when the rotational stiffness increases from 500 N.m/m/rad to 2500 N.m/m/rad.

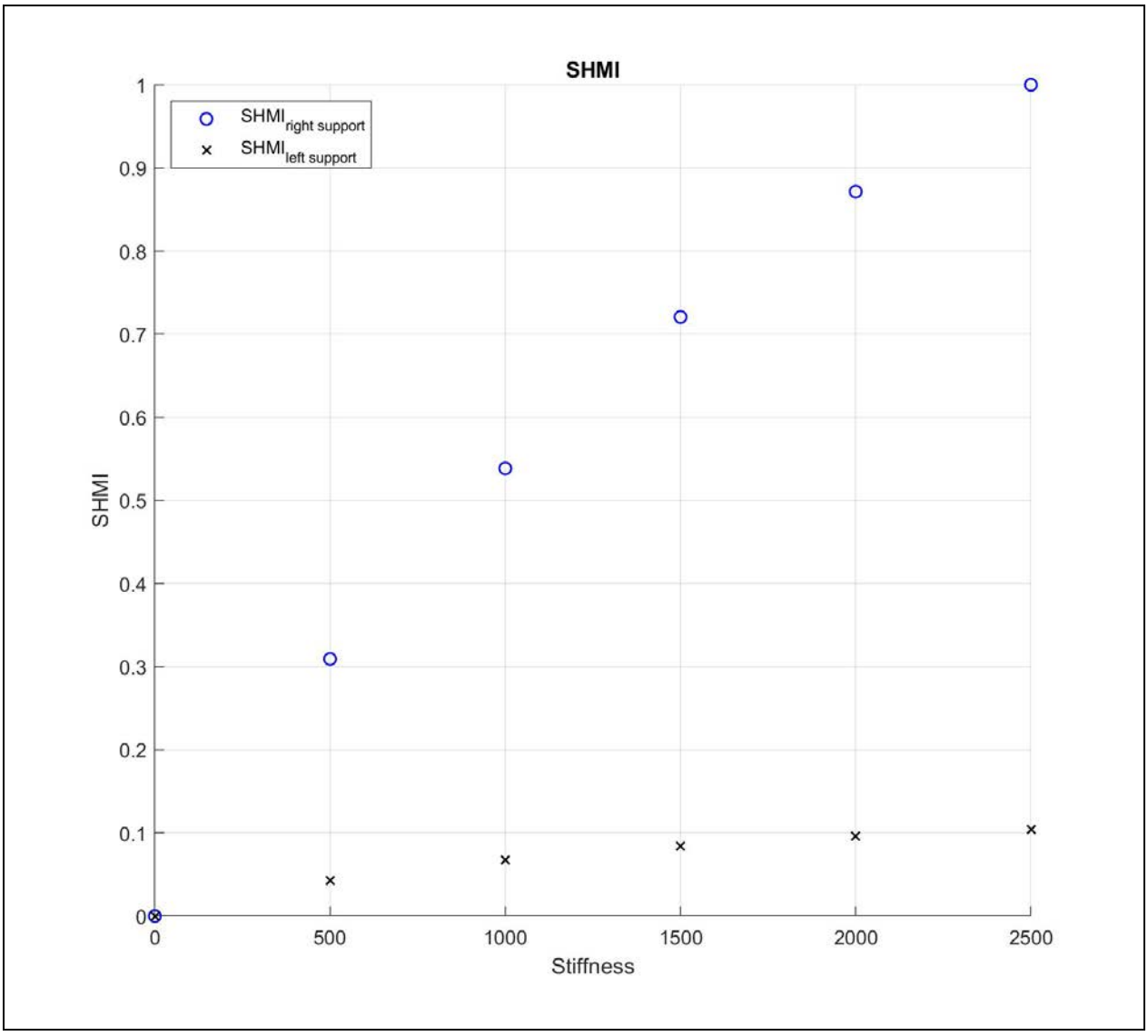

Figure 6-7 Support-health-monitoring index (SHMI) at different values of rotational stiffness (500, 1000, 1500, 2000, 2500 N.m/m/rad) at the right support. Data point symbol (o) represents the relationship at the right support, while data point symbol (x) represents the relationship at the left support.

In order to investigate the effect of changing the stiffness condition of the right support on the response of the left support, the SHMI at the left support was calculated using the different stiffness scenarios. In this case, the angular velocity at sensors 3 and 4 was used in the analysis. Again, the analysis was conducted using a frequency band between 1-100 Hz. As shown in the lower part of Figure 6-7, the SHMI values at the left support were not affected as much by the changes of stiffness of the right support, indicating a weak-coupled effect.

6.3.3. Support Stiffness Resistance Updating (SSRU)

The same transmissibility and coherence functions used to generate SHMI in Section 6.3.2 are used in this section to update the stiffness properties of the support. The support updating process was carried out using ABAQUS/CAE 6.14 for the finite element analysis and MATLAB (2018a) for the numerical analysis.

In this case, the stiffness value at the right support with a rotational spring stiffness of 2500 N.m/m/rad was considered. The response of the angular velocity of sensors 1 and 2 was acquired, then mixed with 5% white noise. The coherence and the transmissibility were calculated, and only the frequency band of 1-100 Hz of the transmissibility was considered for the updating process, since it has higher coherence (Figure 6-8a). As shown in Figure 6-8b, the transmissibility was significantly affected by the presence of noise for the frequencies above 100 Hz but was not much affected in the frequency band of 1-100 Hz. The MATLAB function "fminbnd" was used for the updating process. Constraint limits for the rotational stiffness in the updating process were chosen to be between 1 N.m/m/rad and 10000 N.m/m/rad. Also, a tolerance of 1e-1 was selected for minimizing the objective function (Equation 6-11) to be satisfied before the termination of the updating process.

The resulting updated value of the rotational stiffness of the contaminated data with 5% noise was 2501.99 N.m/m/rad. As shown in Figure 6-9, the updating process took 18 iterations to find a feasible solution for the noisy data scenario. The percentage difference of the updated rotational stiffness and the correct rotational stiffness was 0.08%, indicating that the proposed methodology was successfully updating the rotational stiffness at the right support, even with the presence of 5% noise.

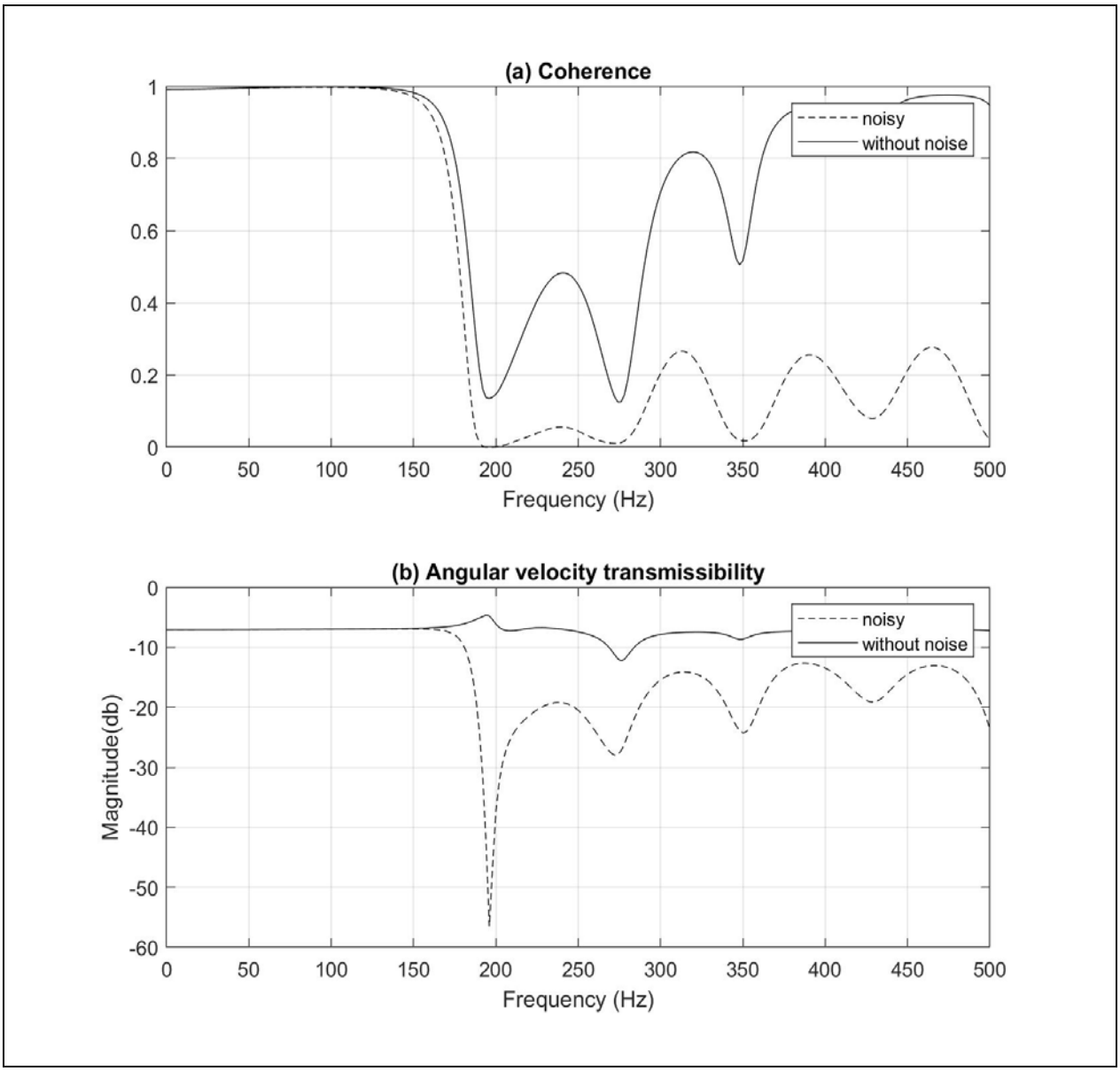

Figure 6-8 The coherence and transmissibility of the right support with 2500 N.m/m/rad scenarios: (a) coherence of the angular velocity with and without added white noise, and (b) transmissibility of the angular velocity with and without added white noise.

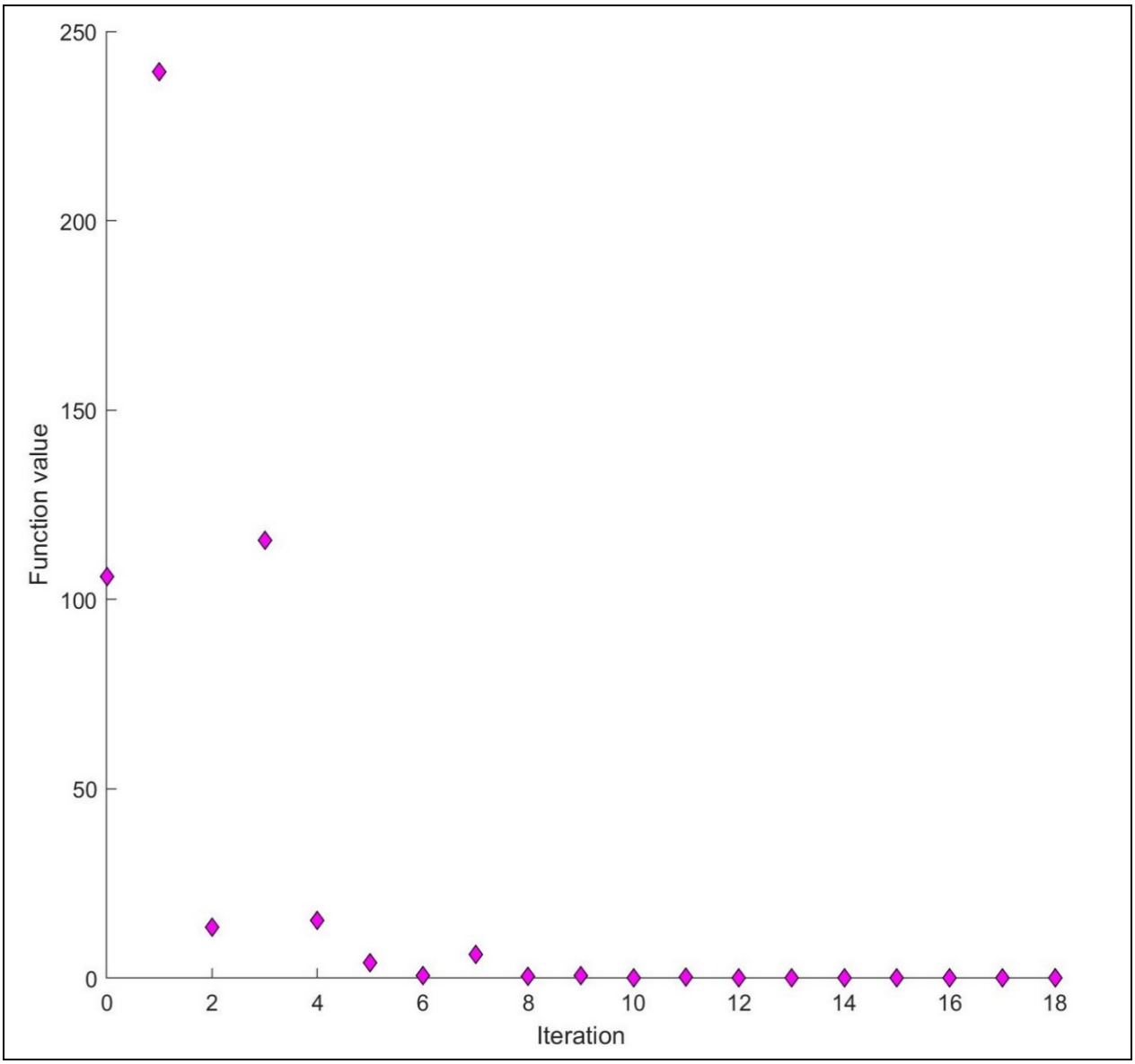

Figure 6-9 Optimization-iteration process for updating the rotational stiffness of the right support with the 2500 N.m/m/rad scenario.

As shown in Table 1, a small percentage of error was generated for the different scenarios despite the presence of noise in the measured time domain signal.

Table 6-1 Updated value of the rotational stiffness scenarios with 5% noise to the time domain signal.

Identified Nm/m/rad	Updated Nm/m/rad	Iteration (Number)	Difference %
500	502.64	21	0.53
1000	1004.7	21	0.47
1500	1505.39	18	0.36
2000	2006.51	18	0.33
2500	2501.99	18	0.08

6.4. Experimental Examples

Two experimental examples are presented in this section to investigate the feasibility of the proposed SHMI and SSRU using simply supported pinned-pinned beams with hinged supports. In the first experiment, the frictional properties of the right hinge of the beam were gradually changed, and SHMI was quantified for each scenario. In the second experiment, rotational springs with different stiffness were attached to the right hinge, and the SSRU algorithm was applied to update the changes in the stiffness properties of the support. Both experiments were conducted on a vibration-isolated frame using the impact test. Figure 6-10 shows the instruments used in the experiment work: a Dell computer xps13, DEWE 43V data acquisition, DYTRAN 5800B4 impact hammer, and DYTRAN 7556A2.

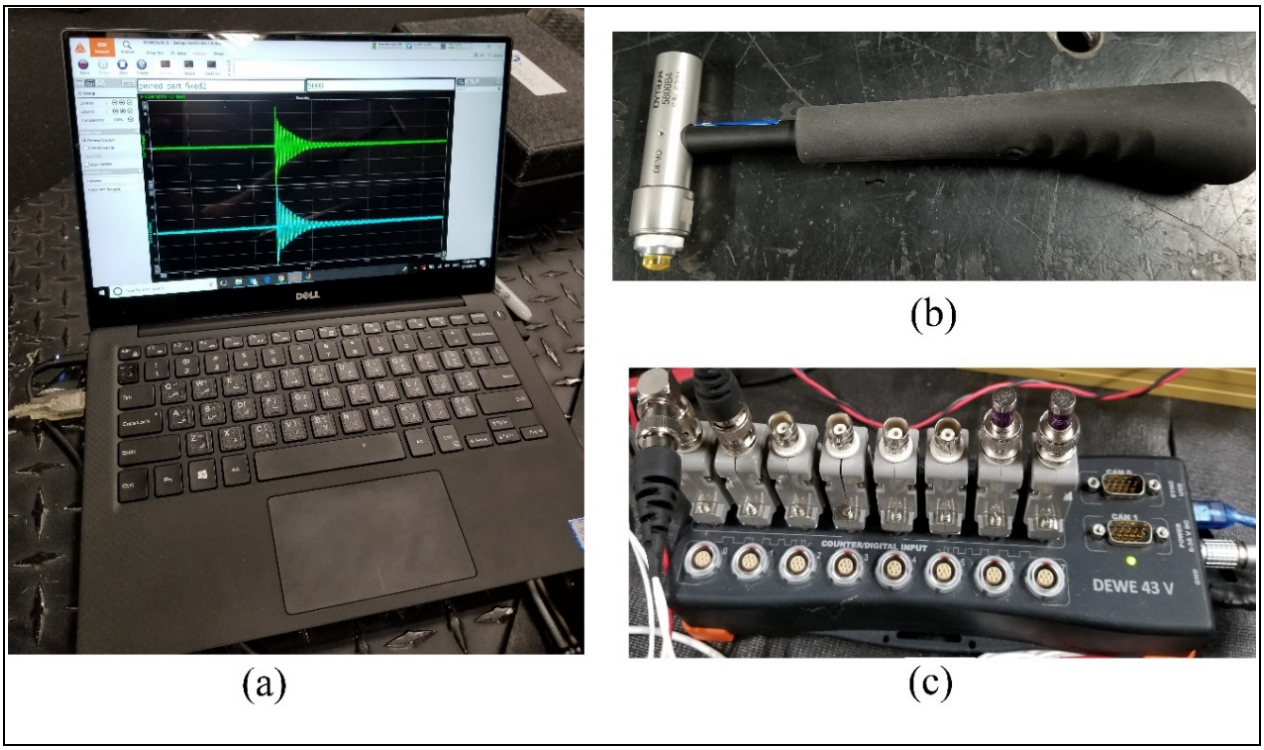

Figure 6-10 Equipment used in the experimental work: (a) computer to store the data, (b) impact hammer, and (c) data acquisition instrument.

6.4.1 Friction Support Experiment

A rectangular pinned-pinned cross-sectional steel beam with dimensions of 800*38.1*6.35 mm was used in this experiment as shown in Figure 6-11a. Adjustable frictional hinges were used to support the beam as shown in Figure 6-11b and Figure 6-11c. Two sensors were placed on the beam, one at the right support (sensor 1) and the second (sensor 2) at a distance of 200 mm from the right support, to simultaneously measure the angular velocity at both locations. An impact load using a hammer (shown in Figure 6-10b) was applied at the middle of the span as shown in Figure 6-11a.

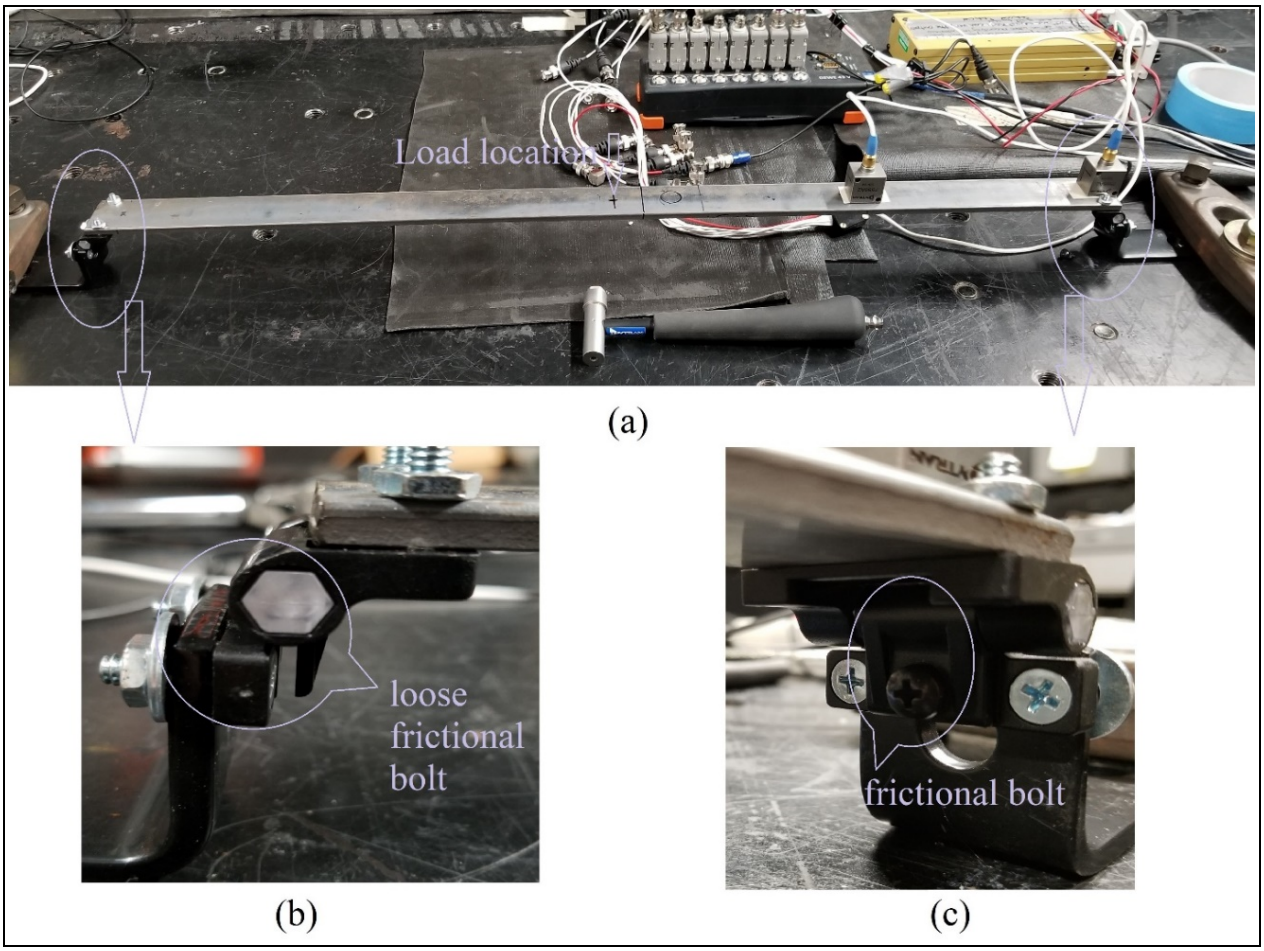

Figure 6-11 Friction support experimental setup: (a) pinned-pinned beam with hinged support and sensor locations, (b) left support, and (c) right support. The resistance of the support in (c) is controlled by tightening/loosening the X-groove bolts on the hinge of the support.

Six sets of experiments (scenarios) were conducted on the simply supported beam by keeping the state of the left support the same (hinge released from friction) and changing the friction magnitude at the right support by tightening the bolt of the friction hinge (healthy, loose, partially loose, partially tightened, tightened, and fully tightened). Ten impacts and measurements of angular velocity for each set of experiments were collected. The set with both hinges of the supports without the frictional bolts was considered as the healthy set in the SHMI calculations.

The coherence and transmissibility functions of the six scenarios were calculated for each impact load. The mean value of each of the ten coherence and transmissibility functions (from the ten impacts) was extracted and used to calculate the SHMI for each of the six scenarios Figure 6-12).

The magnitude of the transmissibility of sensors 1 and 2 was calculated for all sets of scenarios at the same frequency band of 1-80 Hz (high coherence). Figure 6-13 shows that the magnitude of SHMI increased as the rotational resistance at the right hinge support of the beam increased; i.e., the value of the SHMI increases when the friction at the hinge of the right support increases.

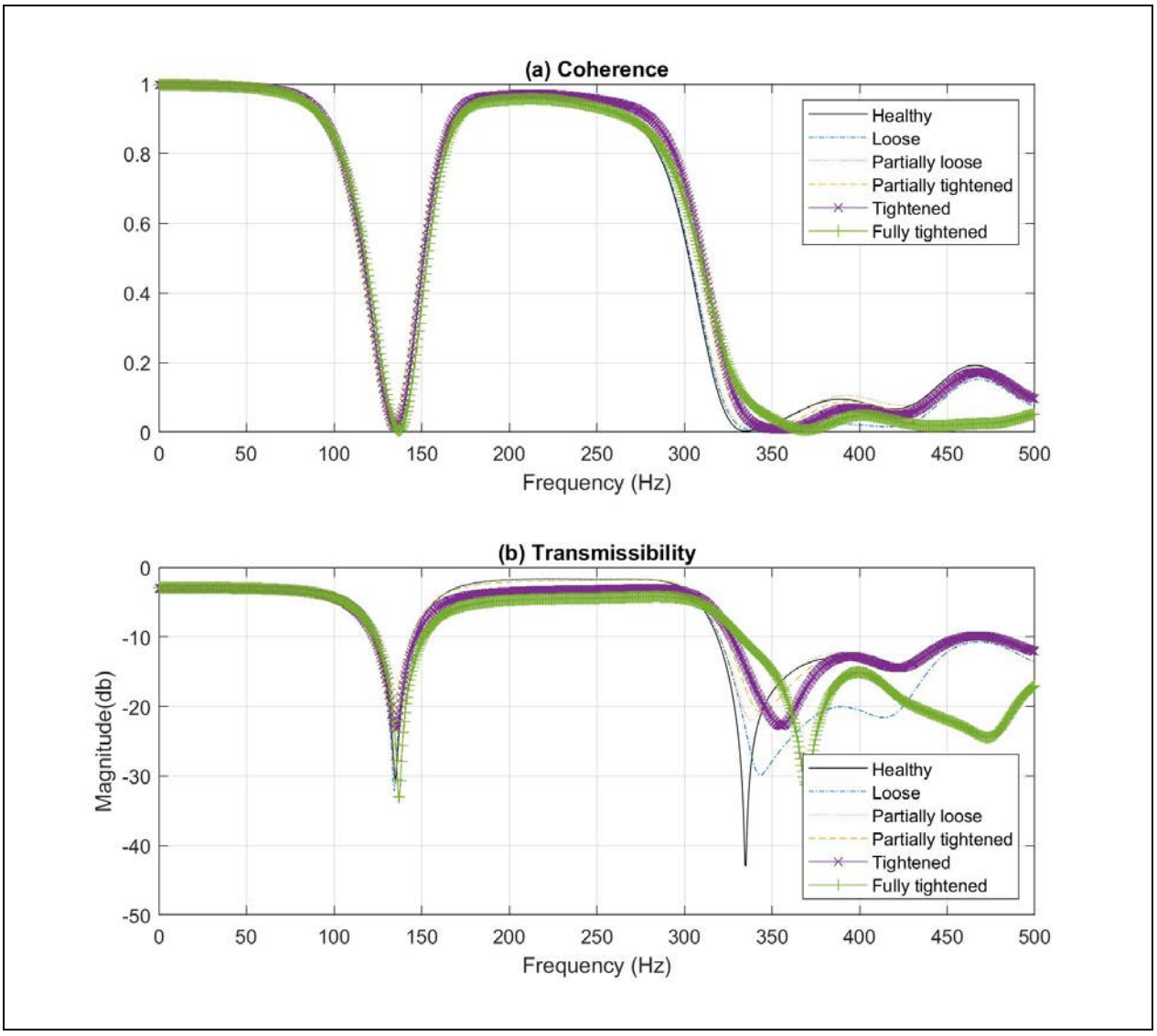

Figure 6-12 (a) The coherence of the healthy scenario, partially tightened bolt, and fully tightened bolt of the right hinge support, and (b) the transmissibility of the healthy scenario, the partially tightened bolt, and the fully tightened bolt of the right hinge support.

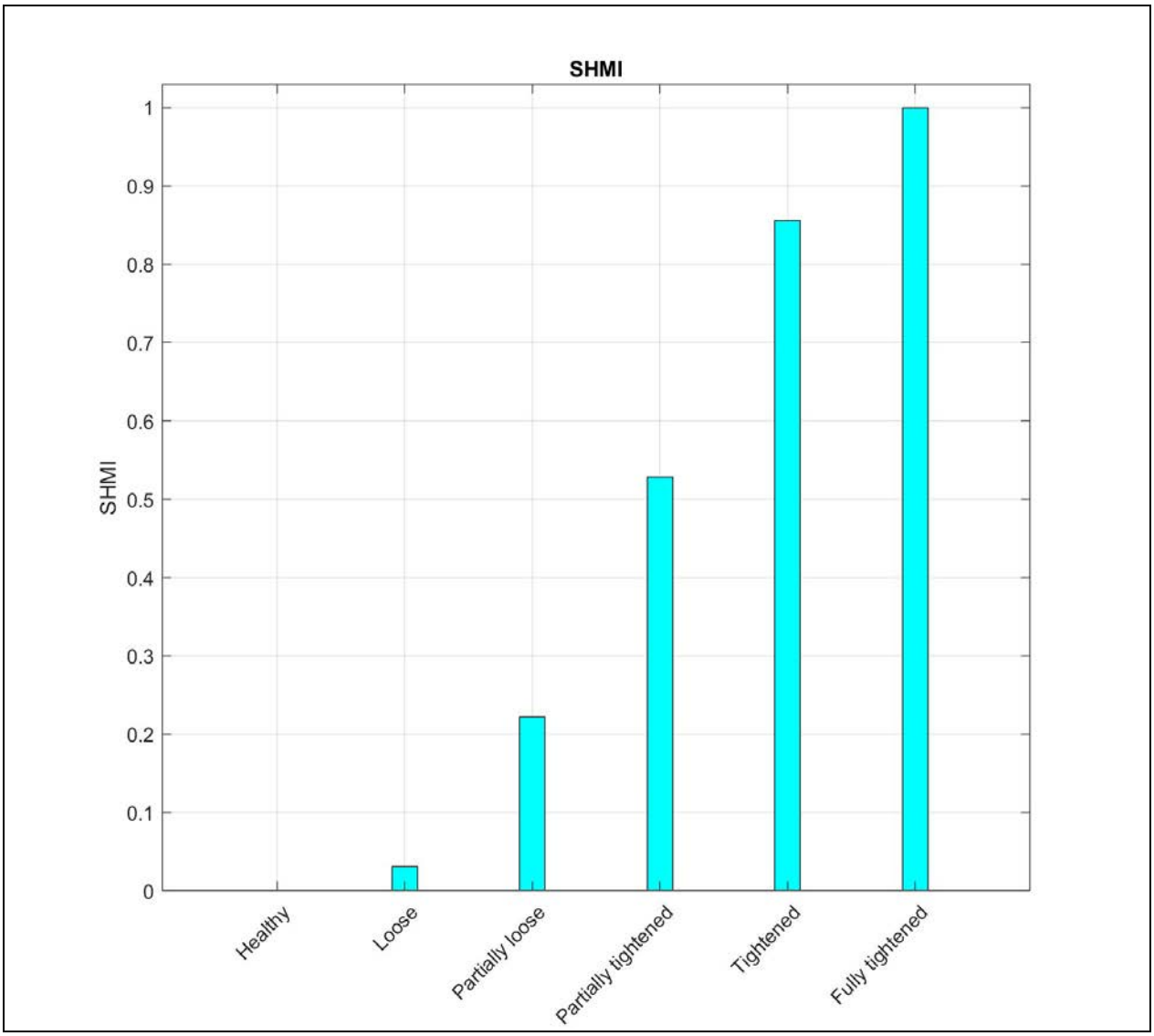

Figure 6-13 The changes in SHMI magnitudes as friction in the right hinge support is increased.

6.4.2. Spring Support Experiment

A rectangular pinned-pinned cross-section steel beam with dimensions of 800*50.8*4.76 mm is selected. Spring hinges have been used to support the beam as shown in Figure 6-14. Similar to the previous example, two sensors were placed at the right support (sensor 1) and at a distance of 200 mm from the right support (sensor 2) to measure the angular velocity at the same time. Ten impact loads using a hammer (shown in Figure 6-10b) were applied at the middle of the span as shown in Figure 6-14a.

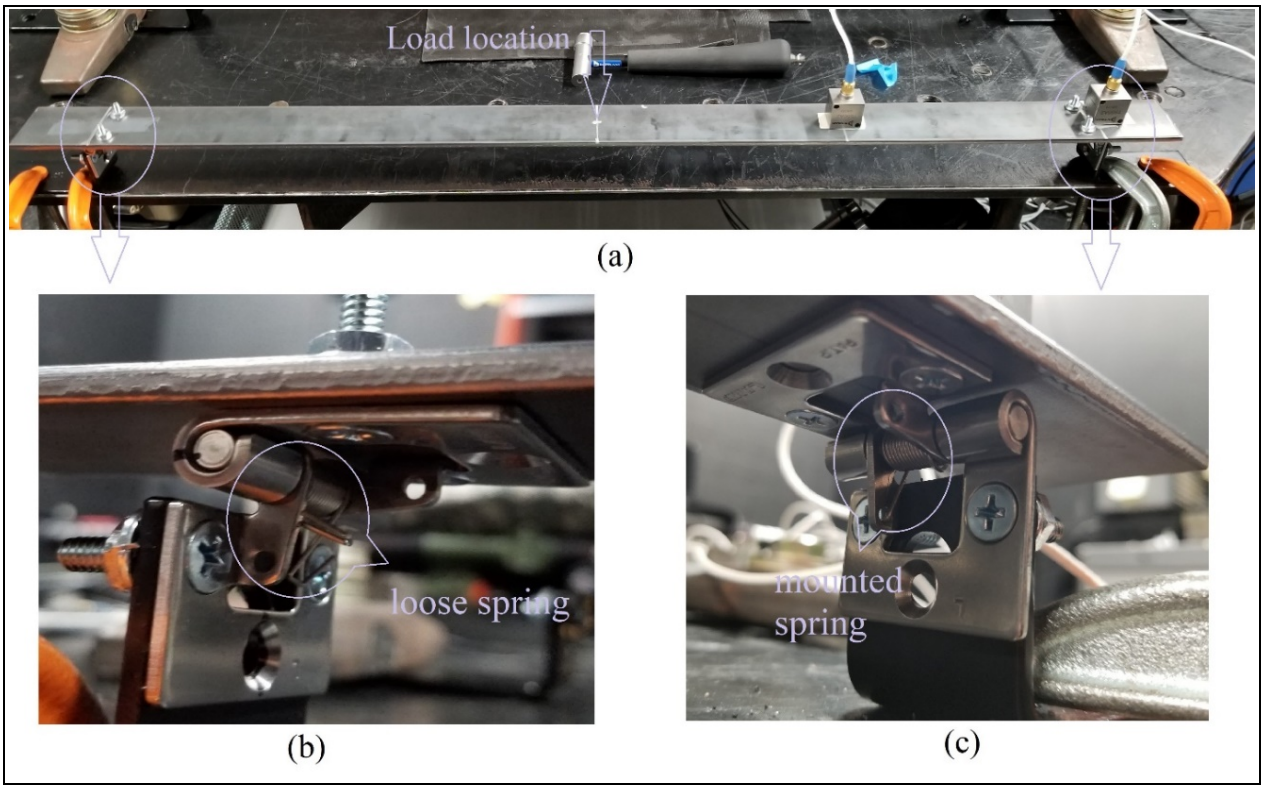

Figure 6-14 Experimental setup of changing the hinge support resistance using rotational springs: (a) setup of the pinned-pinned hinged support beam and sensor locations, (b) left hinge support with no spring attached, (c) right hinge support with a spring attached.

The scenario with the pinned-pinned hinged support without springs mounted on the hinge supports (D0 healthy scenario) was first considered to update the FEM of the beam using the algorithm in Figure 6-3 and Eq. 6-10. Two scenarios for the pinned-pinned beam were updated using Eq. 6-11; D1 and D2 represented 14 wraps of the rotational spring (with a resistance of 5.4 N.m/m/rad) and 15 wraps of rotational spring (with a resistance of 35 N.m/m/rad), respectively. Figures 6-15a, 6-15b, and 6-15c show the mean value of the transmissibility of the healthy (D0) and the updated D1 and D2 scenarios, respectively. The updated values for the rotational spring stiffness were 5.572 N.m/m/rad for D1 scenario and 36.161 N.m/m/rad for D2 scenario.

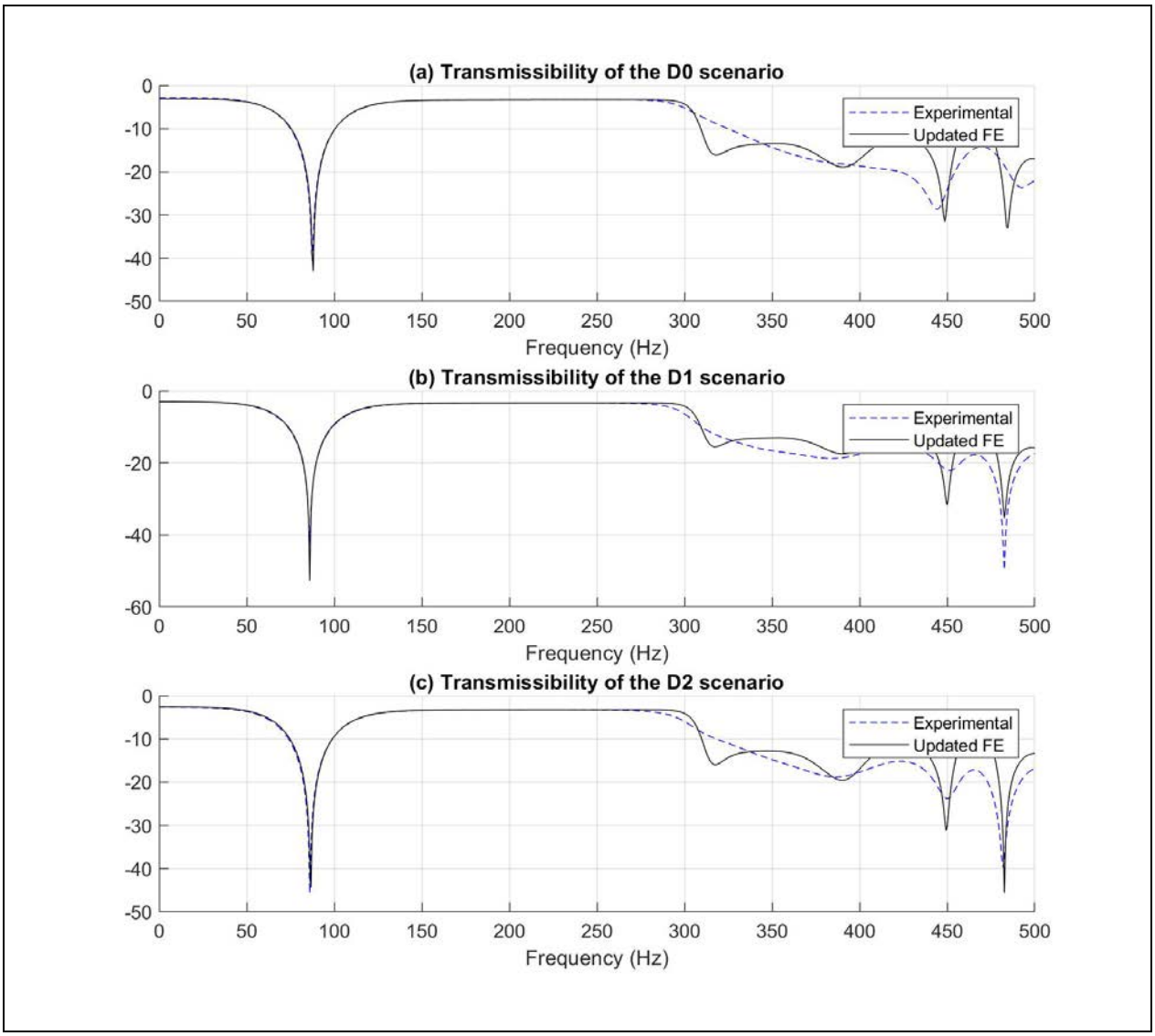

Figure 6-15 The transmissibility of (a) the healthy (D0) scenario, (b) the updated (D1) scenario, and (c) the updated (D2) scenario.

6.5. Discussion

A damage-detection and model-updating methodology was proposed in the current work to assess the support deterioration of a beam-like structure. The proposed method was based on the output responses of the angular velocity at two points on the beam, in the vicinity of the support, using the transmissibility function. The transmissibility function with selected specific frequency bands (with high coherence, close to 1) was considered to avoid the uncertainty and nonlinearity in the response signal at other frequencies. The changes in the state of the support were successfully detected and quantified using the proposed SHMI. Additionally, the rotational stiffness of the added springs at the support was successfully quantified with a small value of uncertainty (between 0.08% and 0.53%), even with the presence of white noise (5%) in the time domain data of the angular velocity.

The proposed method was also successfully tested in the laboratory environment using beams with different types of support resistance. Fabricated hinge supports with varying friction resistance and with spring loading were investigated to represent the changes in the resistance of the rotational stiffness at the support due to deterioration. One limitation of these types of supports is that they may not represent the actual bearings of real bridges; however, the changes in their functionality may reflect behavior similar to what happens in a deteriorated bridge bearing.

While the proposed method was successful in detecting and updating the health conditions of the bearing of beams in numerical and lab testing, its application to real bridges will require more investigations. One of these investigations may focus on the number and locations of sensors on the bridge, as bridges are normally supported on many bearings.

CHAPTER SEVEN: FUTURE WORK

Geometrical nonlinearity has become a vital consideration in the analysis of damage detection and health monitoring since it can take place in many applications, especially those with thin and slender structures. Geometrical, inertial, material, damping, and boundary conditions are some sources of dynamic nonlinearity. In some cases, the presence of cracks that open and close under the operating environment causes a nonlinear response in a structure that initially behaves linearly [62]. Numerical verifications with experimental studies have been presented to study the response of cantilever beams with geometrical nonlinearity [63, 64]. Incorporating both material and geometrical nonlinearity, Adeli and Zhang [65] presented nonlinear analysis of composite girder cable stayed bridges. Carrella et al. [66] presented a study of the effect of nonlinearity on the properties of a structure using collected data of the frequency response function for a single-degree-of-freedom system.

Kerschen et al. [67] presented a review of a nonlinear dynamical structure in system identification and detection. Also, a review by Worden et al. [62] illustrated some damage-sensitive data feature approaches based on nonlinear system response. In another study, using the Hilbert Huang transform and sliding window-fitting techniques, the dynamic characteristics of nonlinear systems were extracted by Pai et al. [68] for numerical and experimental systems. Manoach and Trendafilova [69] studied the sensitivity of some nonlinear vibration parameters to the damage within rectangular plates undergoing geometrical nonlinearity. The numerical results showed that the proposed damage index successfully detected and located the presence of the damage. Mojtahedi et al. [70] utilized principal component analysis for damage detection for offshore jacket-type structures with the presence of geometrical nonlinearity. Figueiredo et al. [71] used machine learning algorithms to classify and detect the damage for a three-story frame

structure in a laboratory environment. They simulated the damage through the nonlinear effect of a bumper mechanism that induces a repetitive-impact-type nonlinearity.

Studying the effect of the geometrical nonlinearity is proposed for the future work with the presence of the damage under operational loading, such as those that can take place during extreme weather conditions. The investigation would include further studies of the state of the art, as well as an analysis of the numerical models and experimental work research.

REFERENCES

1. Bartelds, G., *Aircraft Structural Health Monitoring, Prospects for Smart Solutions from a European Viewpoint.* Journal of Intelligent Material Systems and Structures, 1998. **9**(11): p. 906-910.

2. Chang, P., Flatau, A., and Liu, S., *Review Paper: Health Monitoring of Civil Infrastructure.* Structural Health Monitoring, 2003. **2**(3): p. 257-267.

3. Inventory, N.B. *Deficient Bridges by Highway System 2012*. 2012 7/14/2016 [cited 2016 9/26/2016]; Available from: https://www.fhwa.dot.gov/bridge/nbi/no10/defbr12.cfm.

4. Pandey, A.K., Biswas, M., and Samman, M.M., *Damage Detection from Changes in Curvature Mode Shapes.* Journal of Sound and Vibration, 1991. **145**(2): p. 321-332.

5. Hassiotis, S. and Jeong, G., *Identification of Stiffness Reductions Using Natural Frequencies.* Journal of Engineering Mechanics, 1995. **121**(10): p. 1106-1113.

6. Fan, W. and Qiao, P., *Vibration-Based Damage Identification Methods: A Review and Comparative Study*, in *Structural Health Monitoring*. 2011. p. 83-111.

7. Rytter, A., *Vibrational Based Inspection of Civil Engineering Structures*, u. Aalborg, Editor. 1993, Thesis (doctoral)--Aalborg University, 1993.

8. Doebling, S.W., Farrar, C.R., and Prime, M.B., *A Summary Review of Vibration-Based Damage Identification Methods.* Shock and vibration digest, 1998. **30**(2): p. 91-105.

9. Chen, J.-C. and Garba, J.A., *On-Orbit Damage Assessment for Large Space Structures.* AIAA Journal, 1988. **26**(9): p. 1119-1126.

10. Hajela, P. and Soeiro, F.J., *Structural Damage Detection Based on Static and Modal Analysis.* AIAA Journal, 1990. **28**(6): p. 1110-1115.

11. Crema, L.B., Castellani, A., and Coppotelli, G., *Damage Localization in Composite Material Structures by Using Eigenvalue Measurements*. 1995, United States: American Society of Mechanical Engineers, New York, NY (United States).

12. Cawley, P. and Adams, R.D., *A Vibration Technique for Non-Destructive Testing of Fibre Composite Structures.* Journal of Composite Materials, 1979. **13**(2): p. 161-175.

13. Vantomme, J., *Evaluation of Structural Joints in Composites with Modal Parameters.* Composite Structures, 1992. **22**(4): p. 201-205.

14. Chang, K., Shen, Z., and Lee, G., *Modal Analysis Technique for Bridge Damage Detection*, in *Nondestructive Testing Methods for Civil Infrastructure*. 1995, American Society of Civil Engineers. p. 1-16.

15. Maia, N., Silva, J., and Sampaio, R. *Localization of Damage Using Curvature of the Frequency-Response-Functions*. in *Proceedings of SPIE, the International Society for Optical Engineering*. 1997. Society of Photo-Optical Instrumentation Engineers.

16. Ratcliffe, C.P., *A Frequency and Curvature Based Experimental Method for Locating Damage in Structures.* Journal of vibration and acoustics, 2000. **122**(3): p. 324-329.

17. Sampaio, R.P.C., Maia, N.M.M., and Silva, J.M.M., *Damage Detection Using the Frequency-Response-Function Curvature Method.* Journal of Sound and Vibration, 1999. **226**(5): p. 1029-1042.

18. Charles, R.F. and David, A.J., *Comparative Study of Damage Identification Algorithms Applied to a Bridge: I. Experiment.* Smart Materials and Structures, 1998. **7**(5): p. 704.

19. Humar, J., Xu, H., and Bagchi, A., *Performance of Vibration-Based Techniques for the Identification of Structural Damage.* Structural Health Monitoring, 2006. **5**(3): p. 215-241.

20. Adams, D., *Health Monitoring of Structural Materials and Components: Methods with Applications*. 2007, John Wiley & Sons.

21. Worden, K., *Structural Fault Detection Using a Novelty Measure.* Journal of Sound and vibration, 1997. **201**(1): p. 85-101.

22. Johnson, T.J. and Adams, D.E., *Transmissibility as a Differential Indicator of Structural Damage.* Transactions-American Society Of Mechanical Engineers Journal Of Vibration And Acoustics, 2002. **124**(4): p. 634-641.

23. Schallhorn, C. and Rahmatalla, S., *Crack Detection and Health Monitoring of Highway Steel-Girder Bridges.* Structural Health Monitoring, 2015. **14**(3): p. 281-299.

24. Rucevskis, S., Janeliukstis, R., Akishin, P., and Chate, A., *Mode Shape-Based Damage Detection in Plate Structure without Baseline Data.* Structural Control and Health Monitoring, 2016. **23**(9): p. 1180-1193.

25. Maia, N.M., Almeida, R.A., Urgueira, A.P., and Sampaio, R.P., *Damage Detection and Quantification Using Transmissibility.* Mechanical Systems and Signal Processing, 2011. **25**(7): p. 2475-2483.

26. Johnson, T., Adams, D.E., and Schiefer, M. *An Analytical and Experimental Study to Assess Structural Damage and Integrity Using Dynamic Transmissibility*. in *SPIE proceedings series*. 2002. Society of Photo-Optical Instrumentation Engineers.

27. Li, J. and Hao, H. *Damage Detection of Shear Connectors Based on Power Spectral Density Transmissibility*. in *Key Engineering Materials*. 2013. Trans Tech Publ.

28. Worden, K., Manson, G., and Allman, D., *Experimental Validation of a Structural Health Monitoring Methodology: Part I. Novelty Detection on a Laboratory Structure.* Journal of Sound and Vibration, 2003. **259**(2): p. 323-343.

29. Chesné, S. and Deraemaeker, A., *Damage Localization Using Transmissibility Functions: A Critical Review.* Mechanical systems and signal processing, 2013. **38**(2): p. 569-584.

30. Miller, R., *Factors Influencing Accelerometer Measurement Capabilities-a Practical Measurement Guide*. 1973, David W Taylor naval ship research and development center.

31. Castro, S., Dean, R., Roth, G., Flowers, G.T., and Grantham, B. *Influence of Acoustic Noise on the Dynamic Performance of Mems Gyroscopes*. in *ASME 2007 International Mechanical Engineering Congress and Exposition*. 2007. American Society of Mechanical Engineers.

32. Dean, R.N., Castro, S.T., Flowers, G.T., Roth, G., Ahmed, A., Hodel, A.S., Grantham, B.E., Bittle, D.A., and Brunsch, J.P., *A Characterization of the Performance of a Mems Gyroscope in Acoustically Harsh Environments.* IEEE Transactions on Industrial Electronics, 2011. **58**(7): p. 2591-2596.

33. Wu, Z. and Li, S., *Two-Level Damage Detection Strategy Based on Modal Parameters from Distributed Dynamic Macro-Strain Measurements.* Journal of Intelligent Material Systems and Structures, 2007. **18**(7): p. 667-676.

34. Al-Jailawi, S. and Rahmatalla, S., *Transmissibility-Based Damage Detection Using Angular Velocity Versus Acceleration.* Journal of Civil Structural Health Monitoring, 2018.

35. Lu, P., *A Statistical Based Damage Detection Approach for Highway Bridge Structural Health Monitoring*. 2008: Iowa State University.

36. Sung, S.H., Lee, J.H., Park, J.W., Koo, K.Y., and Jung, H.J., *Feasibility Study on an Angular Velocity-Based Damage Detection Method Using Gyroscopes.* Measurement Science and Technology, 2014. **25**(7): p. 075009.

37. Al-Jailawi, S. and Rahmatalla, S., *Damage Detection in Structures Using Angular Velocity.* Journal of Civil Structural Health Monitoring, 2017: p. 1-15.

38. Liao, Y., Kiremidjian, A.S., Rajagopal, R., and Loh, C.-H. *Angular Velocity-Based Structural Damage Detection*. in *Sensors and Smart Structures Technologies for Civil, Mechanical, and Aerospace Systems 2016*. 2016. International Society for Optics and Photonics.

39. Sung, S., Park, J., Nagayama, T., and Jung, H., *A Multi-Scale Sensing and Diagnosis System Combining Accelerometers and Gyroscopes for Bridge Health Monitoring.* Smart Materials and Structures, 2013. **23**(1): p. 015005.

40. Podder, P., Khan, T.Z., Khan, M.H., and Rahman, M.M., *Comparative Performance Analysis of Hamming, Hanning and Blackman Window.* International Journal of Computer Applications, 2014. **96**(18).

41. Xsens, N., *Mti and Mtx User Manual and Technical Documentation.* 2010.

42. Yang, Y.-B., Wu, C.-M., and Yau, J.-D., *Dynamic Response of a Horizontally Curved Beam Subjected to Vertical and Horizontal Moving Loads.* Journal of Sound and Vibration, 2001. **242**(3): p. 519-537.

43. Krawczuk, M., and Ostachowicz, W., *Natural Vibrations of a Clamped-Clamped Arch with an Open Transverse Crack.* Journal of Vibration and Acoustics, 1997. **119**: p. 145.

44. Viola, E., Artioli, E., and Dilena, M., *Analytical and Differential Quadrature Results for Vibration Analysis of Damaged Circular Arches.* Journal of Sound and Vibration, 2005. **288**(4): p. 887-906.

45. Karaagac, C., Ozturk, H., and Sabuncu, M., *Crack Effects on the in-Plane Static and Dynamic Stabilities of a Curved Beam with an Edge Crack.* Journal of Sound and Vibration, 2011. **330**(8): p. 1718-1736.

46. Zheng, J., Chen, B., and Ye, C.Y. *Damage Detection of Steel Domes Subjected to Earthquakes by Using Wavelet Transform*. in *Advanced Materials Research*. 2011. Trans Tech Publ.

47. Barr, P.J., Halling, M.W., and Womack, K.C., *Structural Health Monitoring of a Curved Girder Bridge Subjected to Different Boundary Conditions.* The 14th World Conference on Earthquake Engineering, 2008.

48. Azizinamini, A., Power, E.H., Myers, G.F., Ozyildirim, H.C., Kline, E.S., Whitmore, D.W., and Mertz, D.R., *Design Guide for Bridges for Service Life*. 2014.

49. White, K., *Bridge Maintenance Inspection and Evaluation*. Vol. 9. 1992: CRC Press.

50. Kayser, J.R. and Nowak, A.S., *Capacity Loss Due to Corrosion in Steel-Girder Bridges.* Journal of Structural Engineering, 1989. **115**(6): p. 1525-1537.

51. Cornwell, P., Farrar, C.R., Doebling, S.W., and Sohn, H., *Environmental Variability of Modal Properties.* Experimental techniques, 1999. **23**(6): p. 45-48.

52. González, A. and Aied, H., *Characterization of Non-Linear Bearings Using the Hilbert–Huang Transform.* Advances in Mechanical Engineering, 2015. **7**(4): p. 1687814015582120.

53. Park, Y.-S., Kim, S., Kim, N., and Lee, J.-J., *Finite Element Model Updating Considering Boundary Conditions Using Neural Networks.* Engineering Structures, 2017. **150**: p. 511-519.

54. Dilena, M., Morassi, A., and Perin, M., *Dynamic Identification of a Reinforced Concrete Damaged Bridge.* Mechanical Systems and Signal Processing, 2011. **25**(8): p. 2990-3009.

55. Aktan, E., Çatbaş, N., Türer, A., and Zhang, Z., *Structural Identification: Analytical Aspects.* Journal of Structural Engineering, 1998. **124**(7): p. 817-829.

56. Brownjohn, J.M.W., Moyo, P., Omenzetter, P., and Lu, Y., *Assessment of Highway Bridge Upgrading by Dynamic Testing and Finite-Element Model Updating.* Journal of Bridge Engineering, 2003. **8**(3): p. 162-172.

57. Gordis, J.H., *Artificial Boundary Conditions for Model Updating and Damage Detection.* Mechanical systems and signal processing, 1999. **13**(3): p. 437-448.

58. Zhang, Q., Chang, T.-Y.P., and Chang, C.C., *Finite-Element Model Updating for the Kap Shui Mun Cable-Stayed Bridge.* Journal of Bridge Engineering, 2001. **6**(4): p. 285-293.

59. Meruane, V., *Model Updating Using Antiresonant Frequencies Identified from Transmissibility Functions.* Journal of Sound and Vibration, 2013. **332**(4): p. 807-820.

60. Brent, R.P., *Algorithms for Minimization without Derivatives*. 2013: Courier Corporation.

61. Forsythe, G.E., Moler, C.B., and Malcolm, M.A., *Computer Methods for Mathematical Computations.* 1977.

62. Worden, K., Farrar, C.R., Haywood, J., and Todd, M., *A Review of Nonlinear Dynamics Applications to Structural Health Monitoring.* Structural Control and Health Monitoring, 2008. **15**(4): p. 540-567.

63. Masri, S., Mariamy, Y., and Anderson, J., *Dynamic Response of a Beam with a Geometric Nonlinearity.* Journal of Applied Mechanics, 1981. **48**(2): p. 404-410.

64. Pai, P. and Palazotto, A., *Large-Deformation Analysis of Flexible Beams.* International Journal of Solids and Structures, 1996. **33**(9): p. 1335-1353.

65. Adeli, H. and Zhang, J., *Fully Nonlinear Analysis of Composite Girder Cable-Stayed Bridges.* Computers & structures, 1995. **54**(2): p. 267-277.

66. Carrella, A., Brennan, M., Waters, T., and Lopes, V., *Force and Displacement Transmissibility of a Nonlinear Isolator with High-Static-Low-Dynamic-Stiffness.* International Journal of Mechanical Sciences, 2012. **55**(1): p. 22-29.

67. Kerschen, G., Worden, K., Vakakis, A.F., and Golinval, J.-C., *Past, Present and Future of Nonlinear System Identification in Structural Dynamics.* Mechanical systems and signal processing, 2006. **20**(3): p. 505-592.

68. Pai, P.F., Huang, L., Hu, J., and Langewisch, D.R., *Time-Frequency Method for Nonlinear System Identification and Damage Detection.* Structural Health Monitoring, 2008. **7**(2): p. 103-127.

69. Manoach, E. and Trendafilova, I., *Large Amplitude Vibrations and Damage Detection of Rectangular Plates.* Journal of sound and vibration, 2008. **315**(3): p. 591-606.

70. Mojtahedi, A., Yaghin, M.L., Ettefagh, M., Hassanzadeh, Y., and Fujikubo, M., *Detection of Nonlinearity Effects in Structural Integrity Monitoring Methods for Offshore Jacket-Type Structures Based on Principal Component Analysis.* Marine Structures, 2013. **33**: p. 100-119.

71. Figueiredo, E., Park, G., Farrar, C.R., Worden, K., and Figueiras, J., *Machine Learning Algorithms for Damage Detection under Operational and Environmental Variability.* Structural Health Monitoring, 2011. **10**(6): p. 559-572.